AN ABSTRACT OF THE THESIS OF

Ali S. Al-Shahrani for the degree of Master of Science in Electrical and Computer Engineering presented on August 26, 2005.
Title: Influence of Adjustable Speed Drive on Induction Motor Fault Detection Using Stator Current Monitoring.

Abstract approved:

Annette von Jouanne Alan K. Wallace

The detection of motor faults at their incipient stage is of prime importance to any industrial plant. The introduction of adjustable speed drives has improved the control and the efficiency of induction motors, however, this has changed the nature of motor faults and how they can be detected.

Current signature analysis has caught the attention of researchers as a mature and simple technique for motor fault diagnosis. In this research three main ways of analyzing the current signature for fault detection have been investigated. These are: the power spectral density analysis, the current negative- and positive-sequence components, and the Park's vector approach.

Three major induction motor faults have been experimentally tested for the above diagnosis techniques: the bearing fault, the broken rotor bar, and the air gap dynamic eccentricity. Using an adjustable speed drive for controlling the motor while applying these fault detection techniques has been compared to the supply of the motor directly from the "mains" source and to a pure sinusoidal supply through a programmable source.

This research has proved that using the power spectral density analysis is a good tool for induction motor fault detection regardless of the source of supply. This technique can be easily implemented in standard commercial adjustable speed drives, with no additional hardware requirements.

Influence of Adjustable Speed Drive on Induction Motor Fault Detection Using Stator Current Monitoring

by
Ali S. Al-Shahrani

A THESIS

Submitted to

Oregon State University

In partial fulfillment of
the requirement for the
degree of

Master of Science

Presented August 26, 2005
Commencement June 2006

Master of Science thesis of Ali S. Al-Shahrani presented on August 26, 2005.

APPROVED:

Co-Major Professor, representing Electrical and Computer Engineering

---

Co-Major Professor, representing Electrical and Computer Engineering

---

Director of the School of Electrical Engineering and Computer Science

---

Dean of the Graduate School

I understand that my thesis will become part of the permanent collection of Oregon State University libraries. My signature below authorizes release of my thesis to any reader upon request.

Ali S. Al-Shahrani, Author

ACKNOWLEDGMENTS

First of all, I am grateful to the GOD, most mighty, most merciful, who created me and gave me the ability to think and search for the truth.

I would like to thank my co-major professors, Alan K. Wallace and Annette von Jouanne for their help, support, encouragement, and valuable direction towards accomplishing this work. Special thanks go to Manfred Dittrich, a developmental engineer from Electrical and Computer Engineering Department, for his help during the experimental stage of this research.

Appreciations go also to my research team members, Ghassan A. Bin Eid and Hamad Al-Tuaimi from Saudi Aramco Company, for their friendship and partnership in this study.

I am thankful to my employer, Saudi Aramco Company for sponsoring my study program. Special thanks go to my career development advisor, Adnan S. Jamal from Aramco Services Company and his colleagues, for granting the support for the equipment used in this research.

Finally, this work would not have been possible without the love and moral support of my father, Saeed Al-Shahrani, my grateful mother, my brothers and sisters, and the rest of my family during my study overseas. I am deeply thankful to my patient and great wife and lovely daughter for their daily support while accompanying me in the United States.

TABLE OF CONTENTS

Page

TABLE OF CONTENTS (Continued)

Page

LIST OF FIGURES

LIST OF FIGURES (Continued)

LIST OF FIGURES (Continued)

LIST OF FIGURES (Continued)

LIST OF FIGURES (Continued)

LIST OF FIGURES (Continued)

LIST OF FIGURES (Continued)

LIST OF TABLES

Influence of Adjustable Speed Drive on Induction Motor Fault Detection Using Stator Current Monitoring

1. Introduction

1.1 Overview

The history of fault diagnosis and protection is as old as machines themselves. The manufacturers and users of electrical machines initially relied on simple protections such as over-current, over-voltage, and ground-fault to ensure safe and reliable operations. However, as the tasks performed by these machines grew increasingly complex, improvements were also required in the field of fault diagnosis. It has now become very important to diagnose faults at their very inception, as unscheduled machine downtime can upset deadlines and cause heavy financial losses.

The major faults of electrical machines can generally be classified as: stator faults, resulting in the opening or shorting of one or more stator phase windings; abnormal connection of the stator windings; broken rotor bar or cracked rotor end-rings; static and/or dynamic air-gap irregularities; bent shaft (similar to dynamic eccentricity), which can result in a rubbing between the rotor and the stator causing serious damage to stator core and windings; shorted rotor field winding; and bearing and gearbox failures [1, 2].

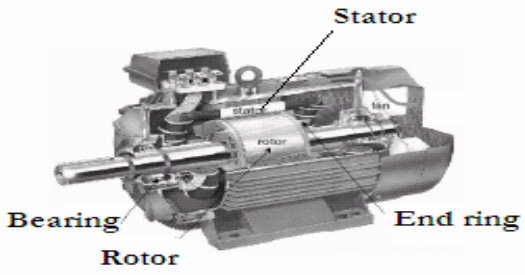

Figure 1.1: Induction motor parts [1]

These faults can produce one or more symptoms, including unbalanced air-gap voltages and line currents, increased torque pulsations, decreased average torque, increased losses and reduction in efficiency, and excessive heating.

The diagnostic methods to identify the above faults may involve several different fields of science and technology. They can be described as electromagnetic field monitoring, search coils, coils wound around motor shafts (axial flux related detection), temperature measurements, infrared recognition, radio frequency emissions monitoring, noise and vibration monitoring, chemical analysis, acoustic noise measurements, motor current signature analysis (MCSA), and artificial intelligence and neural network based techniques [2, 3].

Of the above types of faults, bearing, the stator or armature faults, the broken bar and end ring faults of squirrel cage rotors, and the eccentricity related faults are the most prevalent ones and demand special attention. For these faults detection, the motor current signature analysis has been agreed to be a simple and mature technique.

The introduction of the adjustable speed drive in the early 1970s has improved induction motor efficiency and control. On the other hand, the resulting high rapid switch-on and switch-off of semiconductor switches has caused more problems in particular to the bearing and stator winding as depicted in Figure 1.1 [2, 3, 4].

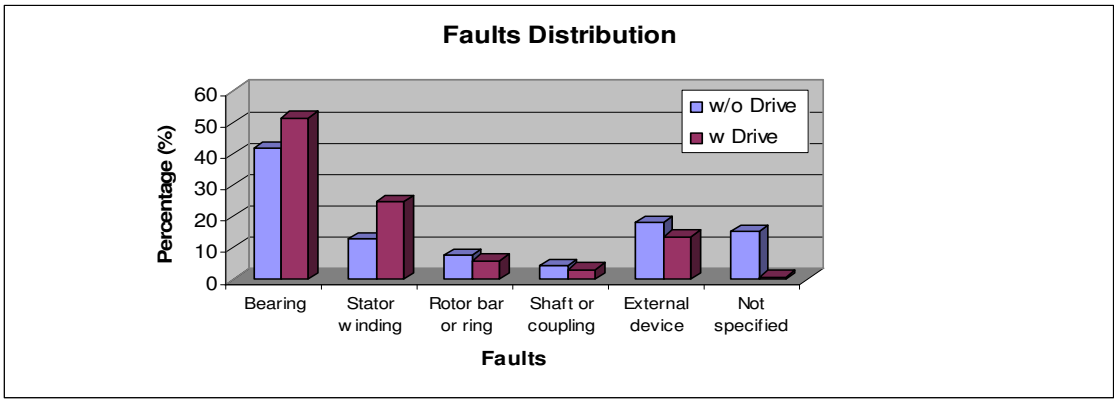

(a) Faults distribution as percentages

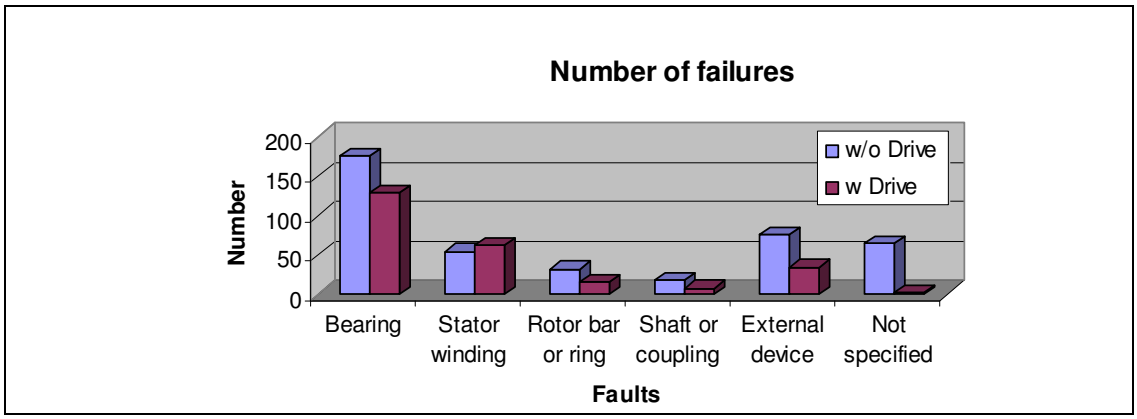

(b) Faults distribution as numbers

Figure 1.2: Distribution of faults types, with and without drive

This shows that researchers must further study the influence of the Adjustable Speed Drive on the diagnosis of the above machine faults and consider how this might change the reliability of the existing current signature analysis diagnosis indexes.

1.2 Literature review and previous works

The area of machine diagnosis has been subjected to a lot of research, however, the drive contribution to these fault diagnosis has not been subject to similar research. The following is a summary of the previous work that is related only due to the drive influence to the fault diagnosis.

1.2.1 Stator turn faults

Villada, F. et al. [5] studied the influence of changing frequency on the stator turn fault detection. Two Pulse Width Modulation (PWM) inverter-driven induction motors, at increasing amounts of winding faults, have been tested using motor current, axial flux and vibration signal analysis techniques. This shows that the time harmonics in the output voltage wave shapes of a PWM inverter causes axial leakage, electrical current and vibration signals associated with a very rich frequency spectrum. As a result, the machine will experience a rise in the heating and substantial vibration of electromagnetic origin.

Results have shown a small rise in some components of the stator current spectrum which are difficult to detect. However, vibration and axial leakage flux frequency spectrums experience measurable differences at many frequencies. Because it is nearly impossible to determine the condition of the motor from only one set of data, a predictive program has been suggested. A program which correlates different types of data to form a complete picture, determine the beginning of change and establish the cause of the problem has been suggested because it is nearly impossible to determine the condition of the motor from only one set of data.

Cash, M. A. et al. [6] develops a straightforward current-based scheme to detect stator turn faults that have occurred due to insulation failure in an adjustable speed drive (ASD)-driven, three-phase induction machine. The method employs simple statistical analysis to detect turn shorts in the stator of the machine. It is shown that the standard deviations of the calibrated, RMS line currents reveal a change in the machine's electrical symmetry caused by turn shorts. To account for inherent machine imbalance, calibration is performed with the machine in a known fault-free state; additionally, current normalization is used to account for varying loads. This method is sensitive to source balance, and is thus proposed only for inverter-fed machines.

1.2.2 Broken rotor bar faults

Miletic, A. et al. [7] compared experimental results of fault diagnosis carried out using a standard supply and those using a frequency converter supply. These results have shown that the current signature analysis of the induction motor, fed from the frequency converter, is much more complicated than in the case of standard supply. Sidebands values are smaller and can be confused with harmonics resulting from frequency changes. The estimated number of broken bars, when using the frequency converter supply, is smaller than when using the standard supply. These observations can lead to an inaccurate conclusion that the motor is in a much better state than it really is. Therefore, in the case of a frequency converter supply, great caution should be taken, and complementary analytical methods should be considered.

Bellini, A. et al. [8] suggested that as far as voltage-supplied machines are concerned, suitable components of the current space vector spectrum can be used to detect electrical faults and to evaluate their entity. Specifically for a supply of frequency, f, and rotor slip s, the negative sequence component at frequency - *f* can diagnose stator faults, while the sum of the sideband components at frequencies *(1- 2s)f* can diagnose rotor faults. However, for controlled machines these indexes are no longer effective, as their information is masked by control action. Therefore, the behavior of other variables have been investigated with the aim of finding new indexes suitable for diagnostic purposes. Simulation and experimental results have shown that the spectrum of the field control loop i_d current can be an effective diagnostic index when the field-oriented control scheme is adopted. In fact the amplitudes of the spectrum components at frequencies *2f* and *2sf* are almost constant with control loop gain variations and they seem quite linearly dependent on the degree of stator and rotor faults respectively. On the contrary, the corresponding component of torque current i_q is dependent on control gain, load conditions and overall on the frequency.

Briz, F. et al. [9] analyzed and discussed the use of high-frequency carrier-signal injection for online fault detection in induction machines. The injection of a low-magnitude high-frequency voltage, superimposed on the fundamental excitation, with the measurement of the resulting negative-sequence carrier-signal current has been shown to effectively detect faults at their incipient stages both in the stator and the rotor. In addition, a reduced sensitivity to the working condition of the machine, i.e., to the flux level, load level, fundamental excitation frequency, and temperature, was also obtained. While broken rotor bar detection has been shown to be viable with a machine having semi-open rotor slots, the rotor-fault-related component in the negative-sequence carrier-signal current spectrum was found to be too small for the case of closed rotor slot machines to allow reliable rotor fault detection. The technique can be easily implemented in standard torque controlled ac drives, with no additional hardware requirements, and requiring only very minor additional signal processing. Machine size is not expected to have a significant impact on the technique's performance, provided that the switching frequency of the inverter feeding the machine is high enough to allow for the injection of carrier-signal voltage in the range of several hundred hertz, i.e., spectral separation

between the carrier signal and the switching frequencies. Supporting this, carrier frequencies as large as one-fourth of the switching frequency have successfully been used.

1.2.3 Air gap eccentricity

Obaid, R. R. et al. [10] examined the effect of changing the input frequency of the induction motor with an adjustable speed drive on the detection of mechanical fault conditions, such as load unbalance and shaft misalignment The mechanical force resulting from these fault conditions is highly dependent on the rotational speed of the motor. When the motor is running at low speeds, the mechanical fault produces less force, resulting in smaller frequency harmonics in the stator current. Nevertheless, results show that the fault signatures are evident in the stator current spectrum even when the drive input frequency is very low. In addition, the drive frequency harmonics do not affect the fault detection, since the frequency components of interest are much lower than the drive frequencies. It is shown that the tested fault conditions are detected in an induction motor line at a rotational speed of as low as 150 rpm. Mechanical fault conditions are detected using a simple, low-cost algorithm that utilizes a single phase of the stator current. The employed algorithm could be easily incorporated into the drive at no additional cost.

1.2.4 Bearing faults

The detection of bearing faults while the drive is controlling the motor has not been subject to research. However, in some research the effects that the drive generates to the shafts and the bearing have been studied. Von Jouanne, A. et al. [11] pproved that the high switching frequency and fast rise time (i.e. high dv/dt) of modern IGBT PWM inverters causes a capacitively coupled voltage to ground across both motor bearings. The bearings are not in electrical contact with the inner or outer race because the grease used has a partially insulating effect. The charge accumulates on the rotor assembly until it exceeds the dielectric capability of the bearing grease. The resulting effect is a flash over-

current that damages the bearing surfaces. The deterioration appears as fluting (grooves) in the bearing race for motors running at relatively constant speeds, and as frosting on the race surfaces for motors operating over a wide speed range. The first signs of deterioration are noisy bearings.

1.3 Research objectives and contributions

This research studies the influence of the Adjustable Speed Drive on the diagnosis of major induction machine major faults and how this might change the reliability of the existing Motor Current Signature Analysis (MCSA) diagnosis indexes. Three different power supplies to the motor have been compared in order to examine their influence on the current signature waveforms and how these reflect in the fault diagnosis. These are: the direct supply from the mains; a pure sinusoidal supply from a laboratory programmable source; and a supply while the Adjustable Speed Drive is controlling the motor (The term ‘drive’ will be used to denote Adjustable Speed Drive throughout this research.). Three main current signature analysis methods have been investigated to find the one which most reliably reflects the right motor conditions experienced with the drive supply to the motor. These are: the power spectral analysis using a non-parametric estimation method like the Welch approach, the current negative- and positive-sequence components, and Park’s vector approach. The different analyses have been experimentally tested on three major motor faults: bearing faults; broken rotor bar; and dynamic air gap eccentricity. Vibration tests were correlated to the current signature analysis of the bearing and air gap eccentricity faults. Broken rotor bar and dynamic eccentricity have been tested at different levels of severity. This would allow seeing the measure of faults that the current signature would reflect on the condition of the motor.

2. Experimental Setup

The experimental setup of this research is depicted in Figure 2.1. Tests were conducted on four 5 Hp, 460/230V, 1200 rpm, 6.5 Amps rated current motors, all with same parameters. One motor was considered a healthy motor and tested. Its current waveforms were used as reference base lines to the other faulty motors. Two motors were tested as broken rotor bar motors. The first of the two had four broken rotor bars and the second had only one broken rotor bar. The outer race of the third motor was drilled in order to simulate a bearing fault. The healthy motor was tested for dynamic eccentricity by installing a disk, with holes drilled at radial distances, on to the shaft of the motor. More descriptive details for each motor will be given in the following chapters.

The load was applied by connecting the shaft of each motor, through a torque transducer, to a DC Motor/Generator of 15Hp, 500V, 27Amps (the output of which was connected to a rheostat bank). Changing the load from zero to the motor-rated full load can be done by applying a DC voltage to the field of the motor and increasing the load rheostat connected to the armature side.

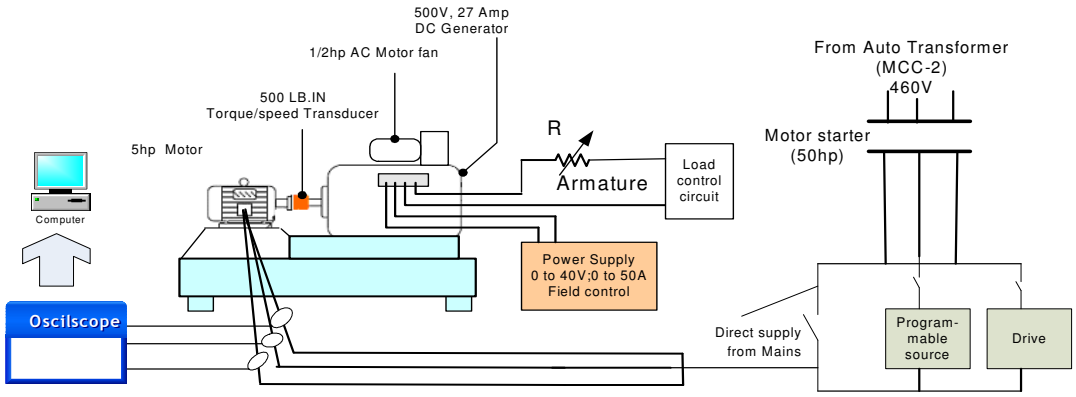

Figure 2.1: Experimental set up

In order to investigate the influence of the drive and to compare it with other power supplies, two other power sources were considered, a programmable source and a direct supply through the mains.

The programmable source was AWG 2005 Arbitrary waveform generator source that provided a very pure sinusoidal supply voltage to the motor, as depicted in Figure 2.2(b). Figure 2.2(a) depicts the case where the power supply is coming from the mains supply. This utility supply is not as clean as that of the programmable source as some voltage unbalance probably exists which introduces third harmonic of the fundamentals to the voltage waveform. In an ideal theoretical scenario, the three-phase utility voltage source contains only odd harmonics while the triplen harmonics (i.e., the third harmonic and its integer multiples) are not present. However, in practice, all of the fundamental harmonics (i.e., odd, even, and the triplen) are present due to voltage source unbalance, asymmetry inherent in manufacture design of machines or loads, or due to faults.

The drive was a commercially available, vector control, 5 Hp, 460 V that controls the motor by injecting a different frequency voltage signal by switching the inverter IGBT's at high switching frequency. The drive produces three identical phase voltages except for 120 phase displacements. These are not purely sinusoidal, as shown in Figure 2.2(c), and contain higher frequency components that are harmonics of the fundamental frequency and will be reflected on the current frequency spectrum. In practice, these harmonics are odd and not multiples of three. The flux that these harmonics produce rotates in the air gap where the direction of rotation maybe the same or opposite to the rotor's direction of rotation. If the flux is produced by a harmonic of order (h=6n-1) where n=1,2,3,… , it has an opposite direction to the rotor. On the other hand if the flux is produced by a harmonic of order (h=6n+1), it will have the same direction of rotation as the rotor. The effects these harmonics have on the fault harmonics detection varies from fault to fault. The ones that are very close to the drive harmonics might be overwhelmed and mask the detection of the fault. The interaction of these harmonics with the fundamental, and with each other produces a pulsation torque which might lead to additional fault symptoms. In practice, the effects that these harmonics produce might be reduced by increasing the switching frequency. All tests were conducted with the drive on variable torque mode.

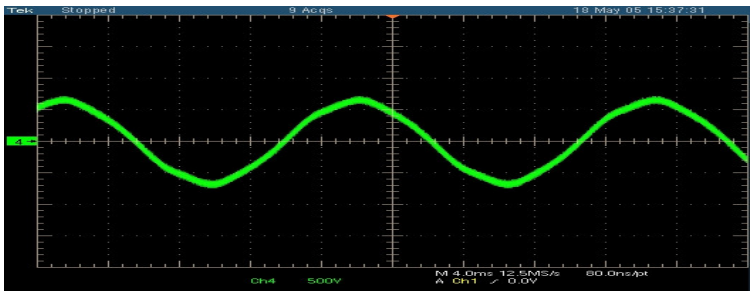

(a) Mains supply at 60 Hz

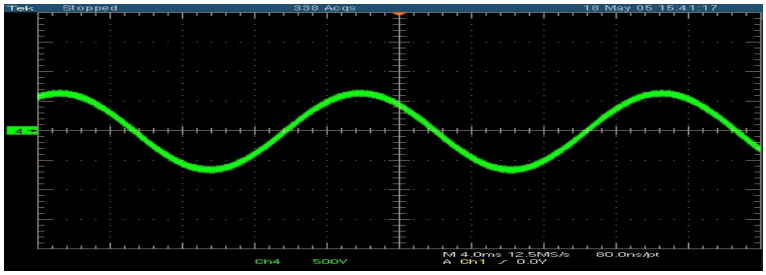

(b) Programmable source at 60 Hz

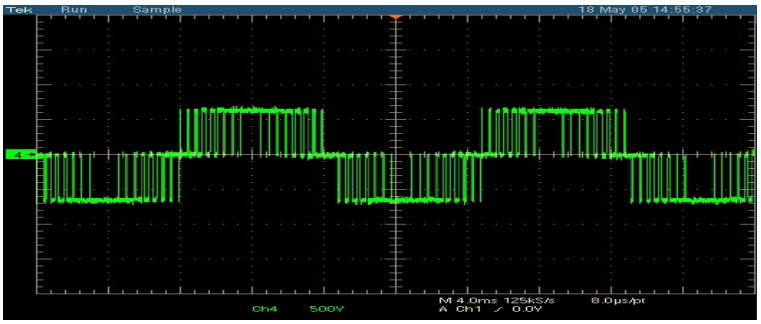

(c) Drive supply at 60 Hz

Figure 2.2: Voltage waveforms of different supply sources

The current waveform data were captured using a digital phosphor oscilloscope with signals from current transformers. Using the MATLAB® library programs these data are then saved and processed through different analysis procedures as discussed in Chapter three. Voltage, current, power and unbalance current and voltage were monitored using Power Measurement IED 7600.

3. Motor Current Signature Analysis (MCSA)

In recent years, the stator current monitoring, well known as motor current signature analysis, has become the focus for many researchers in both the academia and industry. It can provide an indication of the motor condition similar to the indication provided by other monitoring methods (e.g. vibration), without the need to access the motor. In most electrical machine applications, the stator current is usually measured for motor protection. In the case that the motor is being controlled by drive, measuring the current becomes integral to the drive components, which make it available at no cost. There are three main methods through which the captured current data can be analyzed for fault detection using current signature analysis. These are: frequency spectral analysis; negative-, positive- and zero-sequence current components; and Park's vector representation of the three phase current [12].

3.1 Spectral analysis estimation

The spectral analysis technique used in this research is a nonparametric method of estimating the frequency spectrum directly from the signal by describing the distribution of power with the frequency of a random input signal. This technique is also known as the power spectral density method, or PSD function. The PSD process estimates the power distribution by passing the signal through a band pass filter that has a sufficiently narrow bandwidth, and then measuring the power at its output. The power is then divided by the filter bandwidth.

An improved estimator of the PSD is the one proposed by Welch [13]. The method consists of dividing the time series data into (possibly overlapping) segments, computing a modified periodogram of each segment, and then averaging the PSD estimates. The result is Welch's PSD estimate. Welch's method is implemented in the Signal Processing Toolbox via the "spectrum welch" object or "pwelch" function. By default, the data is divided into four segments with 50% overlap between them. A Hamming window is used to compute the modified periodogram of each segment. The averaging of modified periodograms tends to decrease the variance of the estimate

relative to a single periodogram estimate of the entire data record. Although overlap between segments tends to introduce redundant information, this effect is diminished by the use of a nonrectangular window, which reduces the importance or weight given to the end samples of segments (the samples that overlap). However, as mentioned above, the combined use of short data records and nonrectangular windows results in reduced resolution of the estimator. In summary, there is a tradeoff between variance reduction and resolution

The process presupposes that the signal will be of adequate length to allow the filter transients to decay. In this research a period of 10 seconds has been selected as signal length. However, the motor's dynamics are noticeably unstable and probably can influence the demodulation process that requires extensive monitoring of motor operating behavior during the stator current recording process. The PSD Welch modified method was selected as the main spectral estimation method and the MATLAB® program code shown in Appendix A was used to implement it. This method of estimation has began to be implemented as part of the new commercial drive control methods which makes its integration to the drive a useful tool for the motor faults detection without the need to add any hardware [14].

3.2 Current negative and positive components

The analysis of the negative and positive components of the phase current has shown some advantages in terms of faults diagnosis [12]. These components can be obtained using the symmetrical component theory given by:

$$\begin{bmatrix} i_0 \\ i_p \\ i_n \end{bmatrix} = \frac{1}{3}\begin{bmatrix} 1 & a^2 & a \\ a & 1 & a^2 \\ a^2 & a & 1 \end{bmatrix}\begin{bmatrix} i_a \\ i_b \\ i_c \end{bmatrix} \tag{3.1}$$

where $a = e^{j\frac{2\pi}{3}}$, i_0, i_p, i_n are the zero, positive and negative components of the current respectively, and i_a, i_b, i_c are the three-phase stator currents. The MATLAB® program code shown in Appendix B was used to extract negative and positive sequence components. All components, including the main phase current, are then plotted in the same figure using the PSD Welch method. Since the zero sequence components are only applicable to detection of the stator turns fault they are, not considered in this research, and only the negative and positive sequence components where considered for the mechanical faults described earlier.

It is assumed that the current positive sequence components are more related to the non-faults symptoms, like load oscillation or speed ripples, while the current negative sequence components are affected by the fault's severity. This is investigated thoroughly in the following chapters using the faults frequency harmonics sidebands to distinguish between faults symptoms and non-related overwhelming torque ripples from the load. The main disadvantages of this method of analysis are the lengthy time it takes in order to process and manipulate all of the sampled points to extract the positive and negative components, and the requirement of measuring all of the three-phase currents.

3.3 Park's vector approach

As a function of the motor current three phases-variables (i_a, i_b, i_c), Park's Vector components (i_d, i_q) are obtained by transforming the machine's *abc*-currents into the *qd0*-currents using the transformation

$$T(\theta) = \frac{\sqrt{2}}{\sqrt{3}} \begin{bmatrix} \cos(\theta) & \cos(\theta - 120) & \cos(\theta + 120) \\ \sin(\theta) & \sin(\theta - 120) & \sin(\theta + 120) \\ \frac{1}{2} & \frac{1}{2} & \frac{1}{2} \end{bmatrix} \tag{3.2}$$

For $\theta = 0$ and assuming a balanced three-phase supply, the zero-component of the qd0-currents become zero and the Park's vector components are given by: [15]

$$i_d = \frac{\sqrt{2}}{\sqrt{3}} i_a - \frac{1}{\sqrt{6}} i_b - \frac{1}{\sqrt{6}} i_c \tag{3.3}$$

$$i_q = \frac{1}{\sqrt{2}} i_b - \frac{1}{\sqrt{2}} i_c \tag{3.4}$$

When these currents are displayed on a set of orthogonal axis, an ideal machine with no faults will produce a circle centered on the origin. Any fault condition will produce a detectable deviation in this reference pattern. The influence of voltage unbalance and load pulsation can not be predicted using this analysis as will be discussed in the following chapters. This approach has been implemented using the MATLAB® program code shown in Appendix C. The main disadvantages of this process are that it ignores of the effects of the unbalanced voltages and non-idealities and that a quantitative of the fault severity cannot be obtained with this scheme.

4. Broken Rotor Bars

4.1 Analytical background

Unlike stator design, cage rotor design and manufacturing have undergone little change over the years. As a result rotor failures now account for around 5-10% of total induction motor failures [1, 3, 4]. Cage rotors are of two types: cast and fabricated. Previously, cast rotors were used only in small machines. However, with the advent of cast ducted rotors; casting technology can be used even for the rotors of machines in the range of 3000 kW. Fabricated rotors are generally found in larger or special application machines. Cast rotors though more rugged than the fabricated type, can almost never be repaired once faults like cracked or broken rotor bars develop in them.

The reasons for rotor bar and end ring breakage are several [1, 12]. They can be caused by thermal stresses due to thermal overload and unbalance, hot spots or excessive losses, sparking (mainly fabricated rotors), magnetic stresses caused by electromagnetic forces, unbalanced magnetic pull (UMP), electromagnetic noise and vibration, residual stresses due to manufacturing problems, dynamic stresses arising from shaft torques, centrifugal forces and cyclic stresses, environmental stresses caused by contamination and abrasion of rotor material due to chemicals or moisture, mechanical stresses due to loose laminations, fatigued parts, bearing failure, etc.

While broken rotor bars are not common, they are a major concern for industries and utilities that operate large induction machines. Because of their short air gap length and large starting torques, large machines are the most susceptible to damage caused by this form of failure. In many cases, vibration monitoring for this fault condition has a limited benefit [12]

4.1.1 Rotor slot harmonics and air gap flux density

Broken rotor bars can be detected by monitoring the motor current spectral components produced by the magnetic field anomaly of the broken bars [1, 2, 12, 16, 17]. Anomalies caused by the rotor and the stator slots can be modeled by the machine's air gap flux density as given by:

$$B_g(\varphi_s, \theta_{rm}) = MMF_g(\varphi_s, \theta_{rm}) \bullet P_g(\varphi_s, \theta_{rm}) \tag{4.1}$$

where *Bg* is the air gap flux density, *MMFg* is the magnetomotive force, *Pg* is the air gap permanence, φ_s is the stator spatial angular position and θ_{rm} is the rotor mechanical position. The variations in the air gap permanence are due to non-uniform air gap eccentricity while anomalies in the air gap MMF are produced by broken rotor bars and non-sinusoidal winding EMF distributions. Both the MMF and permanence effects are reflected in to the flux density. Because the winding inductances are calculated directly from the air gap flux density, non-uniformities in the MMF produce equivalent sinusoidal variations in these terms. The inductance oscillations give rise to predictable stator current components that can be used for broken bar detection. In this chapter, the characteristic frequency components are reviewed and demonstrated through testing.

In an ideal symmetric machine, the rotor MMF (MMFr) is a traveling wave in the positive direction described by [12, 18]:

$$MMF_r = A_{mmf} \cos(\omega_e t - \varphi_s) \tag{4.2}$$

where A_{mmf} is the amplitude of the rotor MMF and $\omega_e = 2\pi f_e$. In the case of a broken rotor bar, the rotor MMF is modulated by a two-pole magnetic field anomaly that rotates at the mechanical rotor speed since it is attached to the broken bar [12, 19]. Because of the

rapid nature of the magnetic field anomaly, the MMF modulation is rich in harmonics. The n^{th} harmonic of the modulated rotor MMF can be written as:

$$MMF_{rn} = A_n \cos\left(n\theta_{rm} - n\varphi_s\right) \bullet A_{mmf} \cos\left(\omega_e t - \varphi_s\right) \tag{4.3}$$

where A_n is the modulation amplitude and the mechanical rotor position is defined as $\theta_{rm} = 2\pi f_{rm} t$. Knowing that the per unit slip of the machine is given by:

$$s = \frac{f_e - \frac{p}{2} f_{rm}}{f_e} \tag{4.4}$$

this allows equation (4.3) to be expanded to predict the frequency components in rotor MMF traveling wave. The stator current therefore, has harmonic components that are generated at frequencies for broken rotor bar given by:

$$f_{brb} = f_e \left[n\left(\frac{1-s}{p/2}\right) \pm s \right] \tag{4.5}$$

4.2 Experimental analysis

During experiments, broken rotor bar faults were simulated by drilling a hole in the bar in order to vary rotor resistance and exhibit the same symptoms as a real broken rotor bar in a large induction motor. Two stages of severity were tested in the sample motor of specification described above. First, an incipient fault was tested by making one small hole at the front end of one of the 42 bars. The drilling was made at the end of the bar where it joins the end ring as depicted in Figure 4.1(a). This is where most of the large induction motor broken rotor bar start. Then, a very severe case was simulated by drilling four adjacent broken rotor bars as depicted Figure 4.1(b). This broken rotor bar motor was tested with different power supply sources, mains, programmable source and adjustable speed drive to see the influence of changing frequency on the ability of detecting broken rotor bar faults.

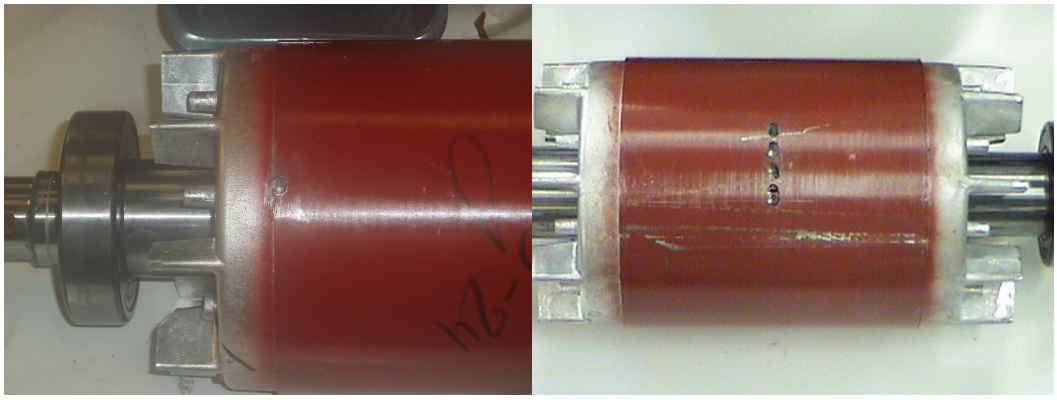

(a) One broken rotor bar (b) Four broken rotor bars

Figure 4.1: Different broken rotor bars

4.2.1 Vibration monitoring test

The vibration test is not recommended for broken rotor bar fault detection [12]. The over all machine vibration level for the broken rotor bar in this experiment (0.034 in/sec) is almost close to the one for the healthy case (0.031 in/sec). New frequencies are not present in the high frequency range where faults are expected for monitoring as shown in Figure 4.2 which indeed doesn't recommend the vibration test as a good tool for monitoring and detecting the broken rotor bar faults.

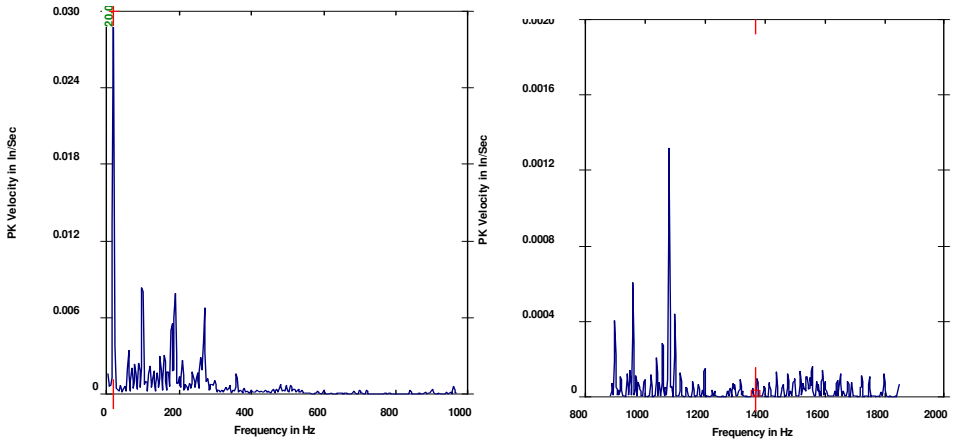

(a) Low frequency range (b) High frequency range

Figure 4.2: Vibration monitoring test

4.2.2 Power spectral density analysis

In addition to the harmonics that are described by equation (4.5), the sideband components f_{sb} around the fundamental can be used for detecting broken bar faults as given by:

$$f_{sb} = (1 \pm 2s) f_s \tag{4.6}$$

While the lower sideband is specifically due to broken rotor bar, the upper sideband is mainly affected by consequent speed oscillation. The motor-load inertia also affects the magnitude of these sidebands. In fact, the broken bars actually give rise to a sequence of such sidebands given by

$$f_{sb} = (1 \pm n2s) f_s \ , \quad n = 1, 2, 3, \ldots. \tag{4.7}$$

Using equation (4.6), Table 4.1 shows the first order sidebands for different frequencies tested when the motor is supplied from the drive and the motor is running at full load.

f_s	$n_s=120f/p$	n_r	s	$(1+2s)f$	$(1-2sf)$
30	600	532.5	0.1125	36.75	23.25
40	800	799.48	0.00065	40.052	39.948
60	1200	1170.8	0.024333	62.92	57.08
80	1600	1537.9	0.038812	86.21	73.79

Table 4.1: Broken rotor bar sidebands with drive supply at different frequencies

where n_s is the stator or synchronous speed and n_r is the rotor or mechanical speed. Table 4.2 shows the first order sidebands for different frequencies tested, when the motor is supplied from a programmable source and the motor is running at full load.

f_s	$n_s=120f/p$	n_r	s	$(1+2s)f$	$(1-2sf)$
30	600	586.5	0.0225	31.35	28.65
40	800	783.5	0.020625	41.65	38.35
60	1200	1170.6	0.0245	62.94	57.06
80	1600	1544.2	0.034875	85.58	74.42

Table 4.2: Broken rotor bar sidebands with programmable supply at different frequencies

Table 4.3 shows the first order sidebands when the motor is fed directly from the mains at 60 Hz and the motor is running at full load.

f_s	$n_s=120f/p$	n_r	s	$(1+2s)f$	$(1-2sf)$
60	1200	1170.9	0.02425	62.91	57.09

Table 4.3: Broken rotor bar sidebands with mains supply.

The following power spectral density figures are obtained using the Welch spectral estimation as described in Chapter 3. The first order sidebands at n=1 are shown first in the following figures. In comparison to the other sidebands, their high magnitude reflects a better indication of the broken rotor bar fault. Figure 4.3 depicted the first order sidebands harmonics where the motor is running at full load and fed from the mains supply at 60 Hz. This figure shows the single broken rotor bar sidebands and the four broken rotor bars respectively. The difference between the healthy and the broken rotor bar sidebands is noticeable - it is more than 20 db in magnitude. The upper sideband at *(1+2s)f* shows a higher magnitude than the lower sidebands at *(1-2s)f* because it is more influenced by the speed oscillations. The level of severity can be easily monitored from this difference in magnitude. Similarly, the four broken rotor bar sidebands are higher by 10 db than the sidebands of a single broken rotor bar.

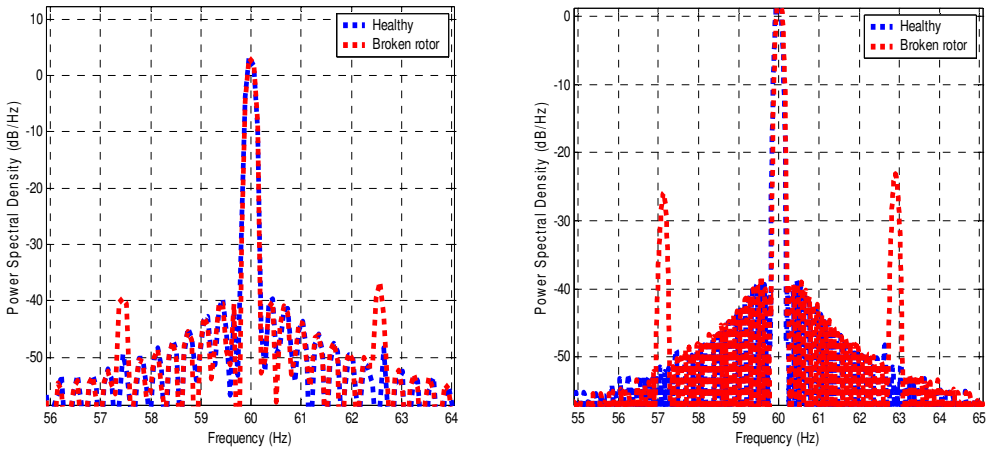

(a) One broken rotor (b) Four broken rotor bars

Figure 4.3: Spectral densities when the motor is powered by mains, at 60 Hz, and running at full load

Figure 4.4 shows the dependency of the broken rotor bar sidebands as given by equation (4.6) on the speed of the motor or the slip. The first order sidebands at different loading points, starting from no load up to full load, have been plotted on the same figure for the two different broken rotor bar severities. As the load increases, i.e. as speed decreases, sidebands positions shift away from the fundamental frequency which proves the dependency of the sideband harmonics on the speed or the slip. Another important point is that the magnitude of the upper and lower sidebands increases as load increases where the upper sideband shows always a higher magnitude than the lower sideband. For the single broken rotor bar, the sidebands start to appear from more than 50% load and above, however, for the four broken rotor bar they start to appear from more than 25% load level and above. Thus, it is concluded that it is almost impossible to detect broken rotor bars while the motor is running without a load and a better broken rotor bar diagnosis could be achieved at full load level.

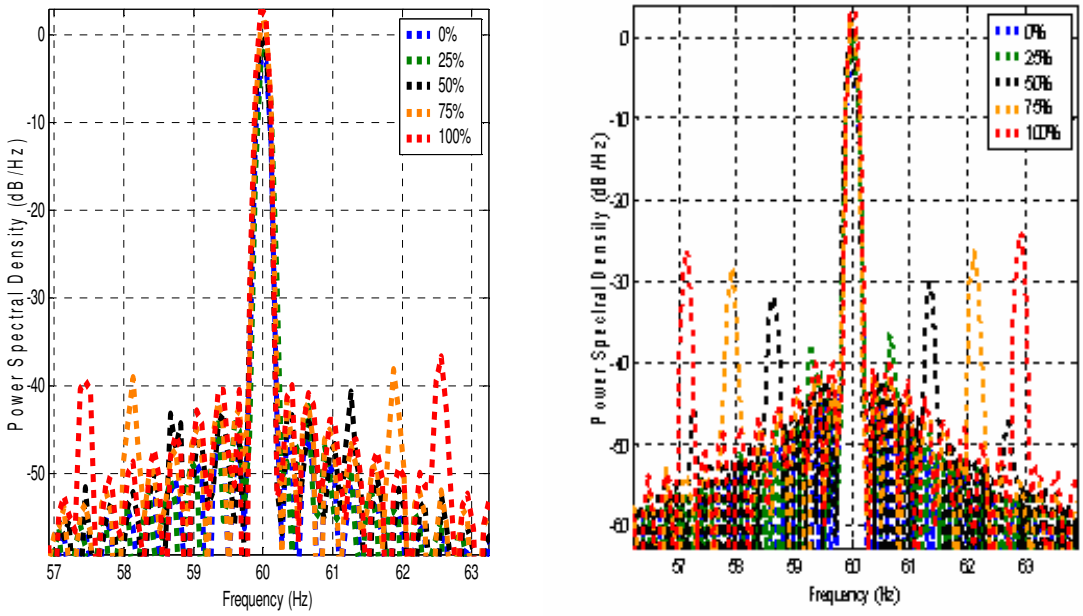

(a) One broken rotor bar (b) Four broken rotor bars

Figure 4.4: Spectral densities at different loading levels with mains as power source

Similar results were collected when the motor was fed from a programmable source and a clean sinusoidal voltage supply signal was injected into the motor as depicted in Figure 4.5. The positions of the sidebands for the full load case come as predicted by Table 4.3. The two sidebands for the single broken rotor have almost the same amplitude. This is, however, not the case for the four broken rotor bars. This indicates that the supply unbalance doesn't highly affect the detection of the broken rotor bar first order sidebands.

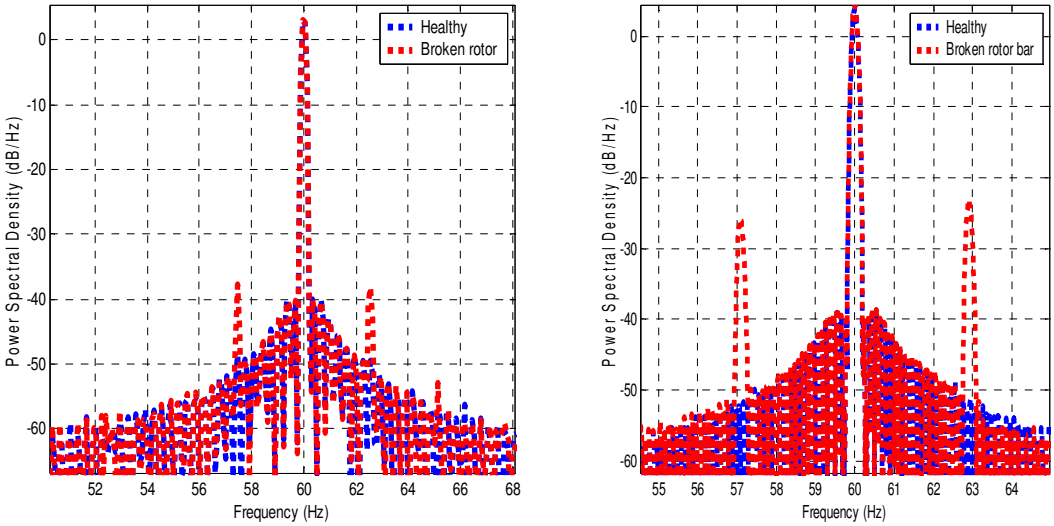

(a) One broken rotor bar (b) Four broken rotor bars

Figure 4.5: Spectral densities with programmable 60 Hz source at full load

The influence of changing frequency on the detection of the broken rotor bar sidebands is shown in the following figures. Four different frequencies have been tested, namely, 30 Hz, 40 Hz, 60Hz and 80 Hz. All sidebands for the different frequencies come as predicted by table 4.2. This proves the validity of equation 4.6 for predicting the effects of broken rotor bar. For the single broken rotor bar, the sidebands are barely evident at low frequencies, such as 30 Hz and 40 Hz (depicted in Figure 4.6): however, as frequency increases, the magnitude starts to increase and the sidebands shift away from the fundamental.

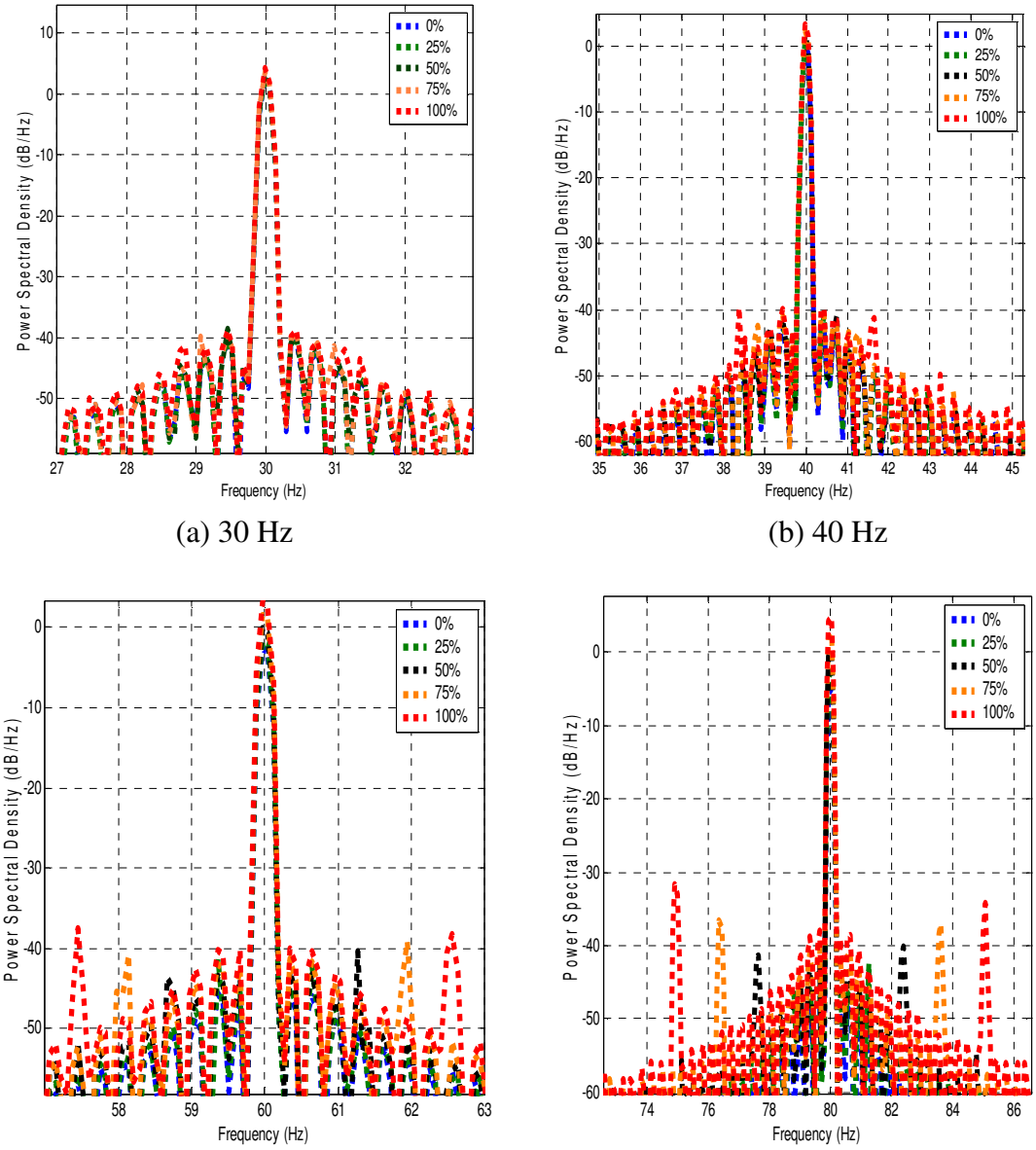

(a) 30 Hz (b) 40 Hz

(c) 60 Hz (d) 80 Hz

Figure 4.6: Single broken rotor bar with programmable source at different loading points and different frequencies

The four broken rotor bar sidebands at different frequencies are depicted in Figure 4.7. By comparing these graphs to the ones shown in the previous figure, the level of fault severity can be clearly distinguished. It can be concluded that it is harder to detect incipient broken rotor bar sidebands when supply frequency is less than the normal operating frequency , and, in particular at low loading levels.

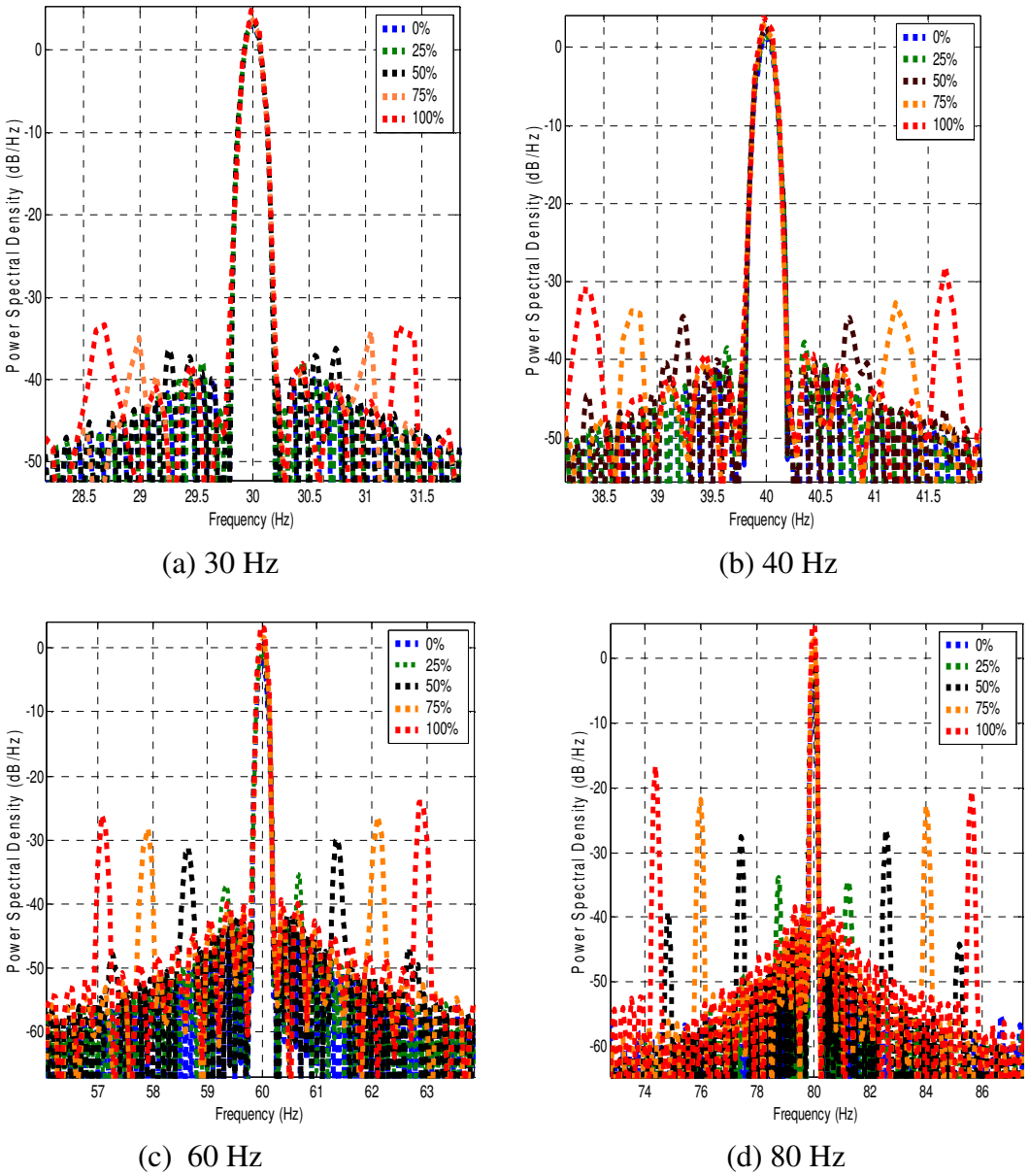

(a) 30 Hz (b) 40 Hz

(c) 60 Hz (d) 80 Hz

Figure 4.7: Four broken rotor bar with programmable source at different loading points and at different frequencies

The following figures depict the case when the motor is being controlled by an adjustable speed drive and frequency is being adjusted. Unlike the programmable source, the injected voltage is not a pure sinusoid but contains a lot of harmonics as described in chapter 2. In theory, the drive harmonics are the odd and non triplen harmonics like the 5^{th}, 7^{th}, and 11^{th}, however, in practice, more of these harmonics tend to exist due the

machine designs, load, and supply. Luckily, the broken rotor bar sidebands of concern are very close to the fundamental and, therefore, not corrupted by the high energy that the other non-faulty related harmonics have. This is shown in Figure 4.8 for the two levels of broken rotor bar severity. In this case, the drive is supplying the motor which is running at full load and 60 Hz. The sidebands have almost the same magnitude as is in the programmable supply and mains supply cases.

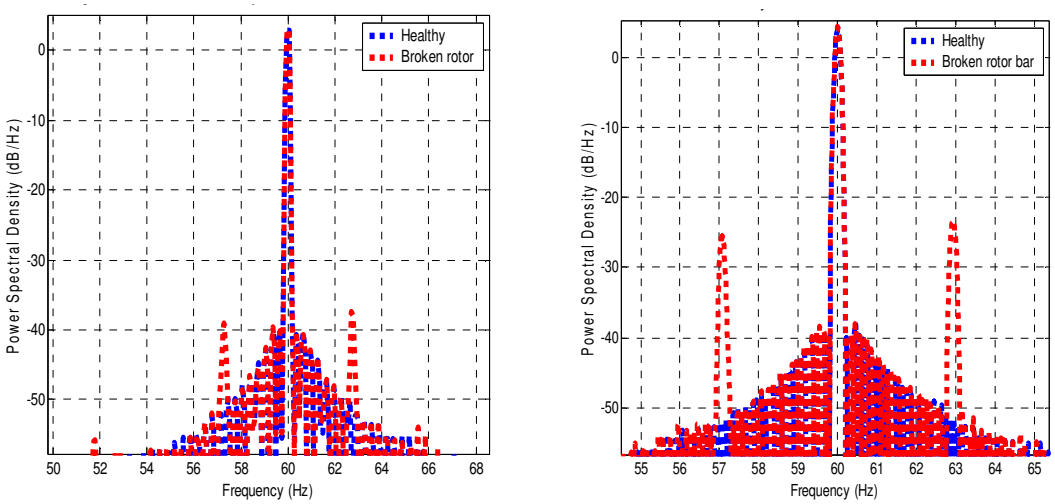

(a) One broken rotor bar (b) Four broken rotors

Figure 4.8: Spectral densities with drive as source at full load and 60 Hz

Other than running the motor at the rated operating frequency, the drive induces the broken rotor bar lower sideband more than the upper sideband – in contrast to the findings for mains and the programmable supply sources. This is shown in Figure 4.9. However, both sidebands are evident even for the single broken rotor bar. Another important observation is that the sidebands are of higher magnitude as frequency diverges from the normal operating frequency (60 Hz) in contrast to the corresponding frequencies when using the programmable source. Moreover, as frequency diverges the sidebands positions vary but in different ways than when using the programmable source. Nevertheless, they are as predicted by Table 4.2 for the drive case. These differences and similarities between the drive and the programmable source are due to the different ways of controlling the load that each one uses. The drive has more control on the load than the

programmable source. Both voltage and frequency are manipulated by the drive in order to achieve the commanded speed and torque.

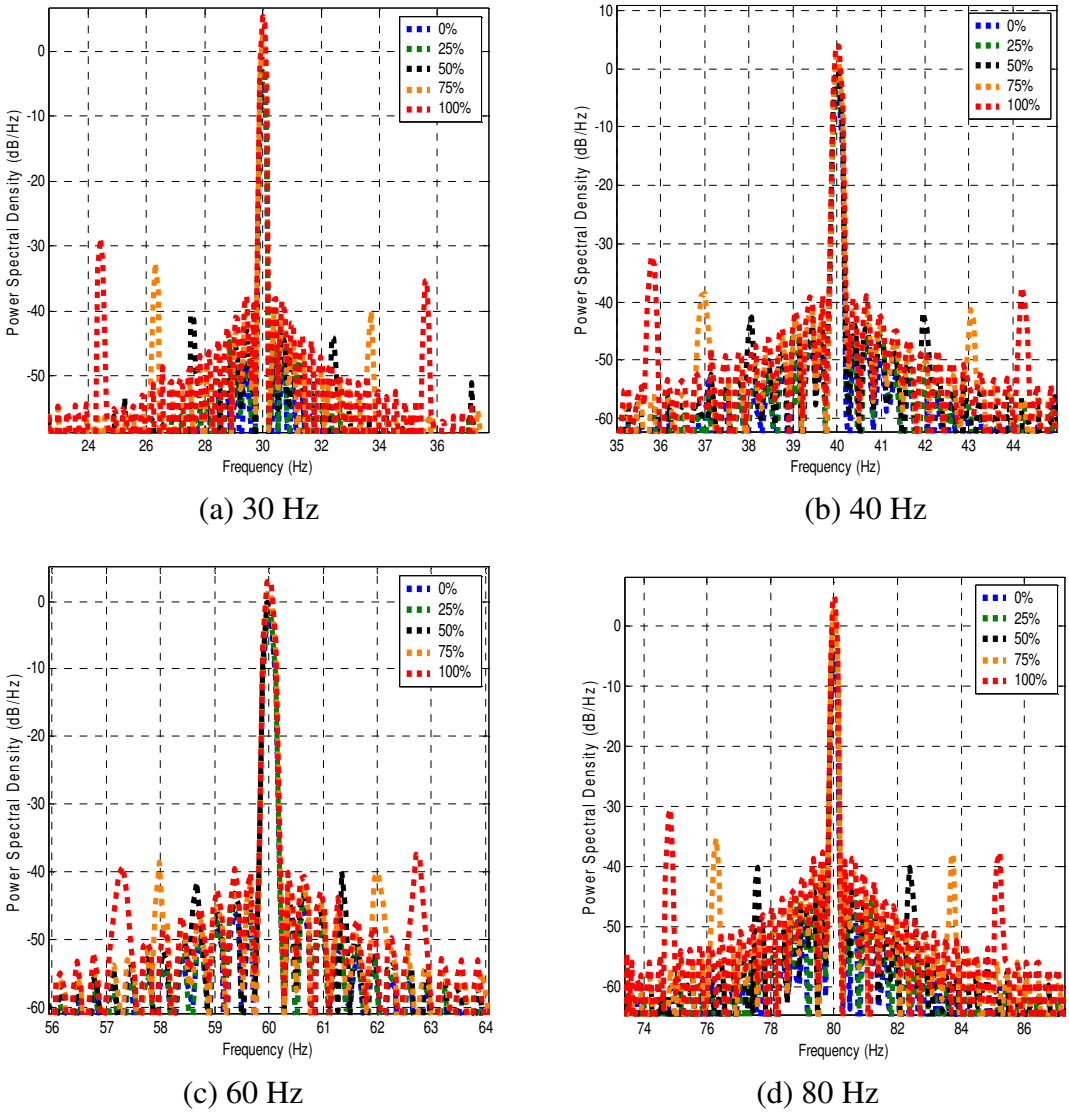

(a) 30 Hz (b) 40 Hz

(c) 60 Hz (d) 80 Hz

Figure 4.9: Single broken rotor bar with drive source at different loading points and at different frequencies

The level of severity can be distinguished from the induced magnitude of the sidebands. Figure 4.10 depicts the four broken bar sidebands at different frequencies and different loads. Similar to the single broken rotor bar the lower sidebands were induced more than the upper sidebands. This is more visible for frequencies lower that the 60 Hz. Similarly, it is obvious for frequencies higher that the 60 Hz. This concludes that,

regardless of the source of supply and the frequency that the motor is running at, the broken rotor bar can be detected, in particular at high load levels.

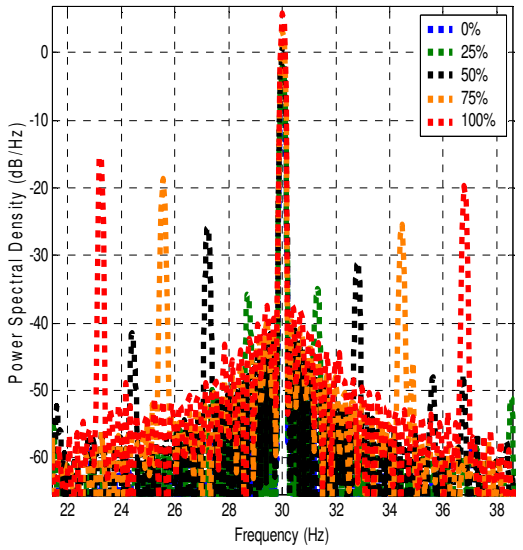

(a) 30 Hz

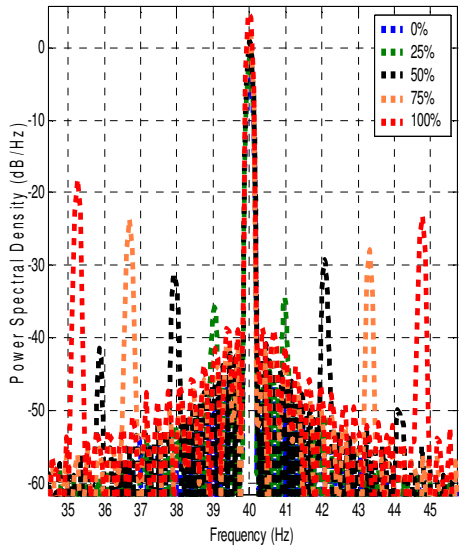

(b) 40 Hz

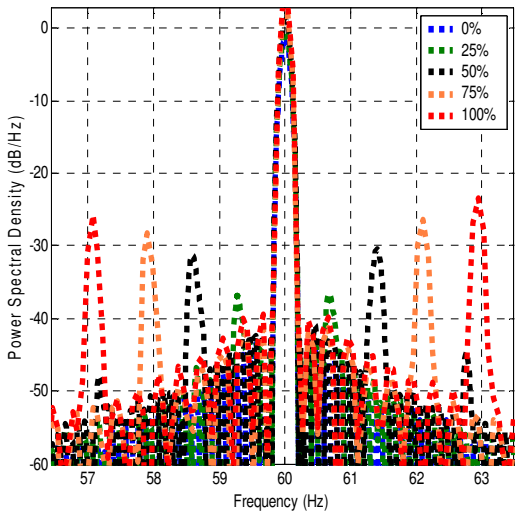

(c) 60 Hz

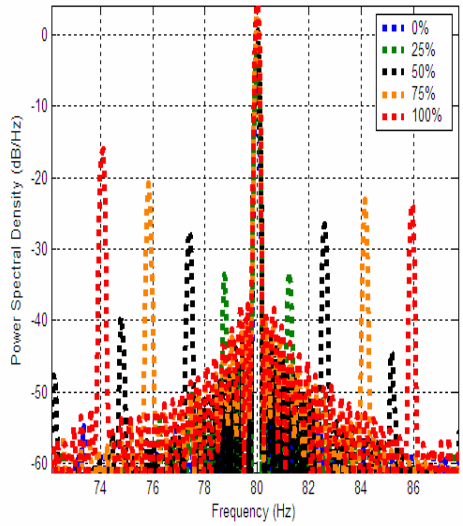

(d) 80 Hz

Figure 4.10: Four broken rotor bar with drive source at different loading points and at different frequencies

At a severe broken rotor bar case, more sidebands such as, the second and third order sidebands of the fundamentals show an indication of the broken rotor bar. This is shown in Figure 4.11 for the four broken rotor bars while the motor is powered from different sources of supply. However, for the single broken rotor bar, only the first order sidebands

of the fundamentals provide an indication of the broken rotor bar fault as shown in Figure 4.12.

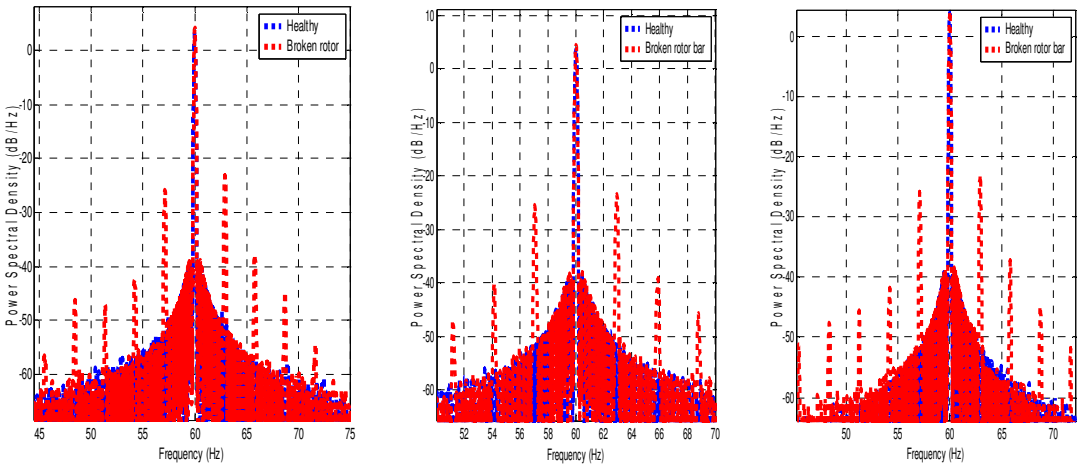

(a) Mains source (b) Drive source (c) Programmable source

Figure 4.11: Different sidebands for four broken rotor bars

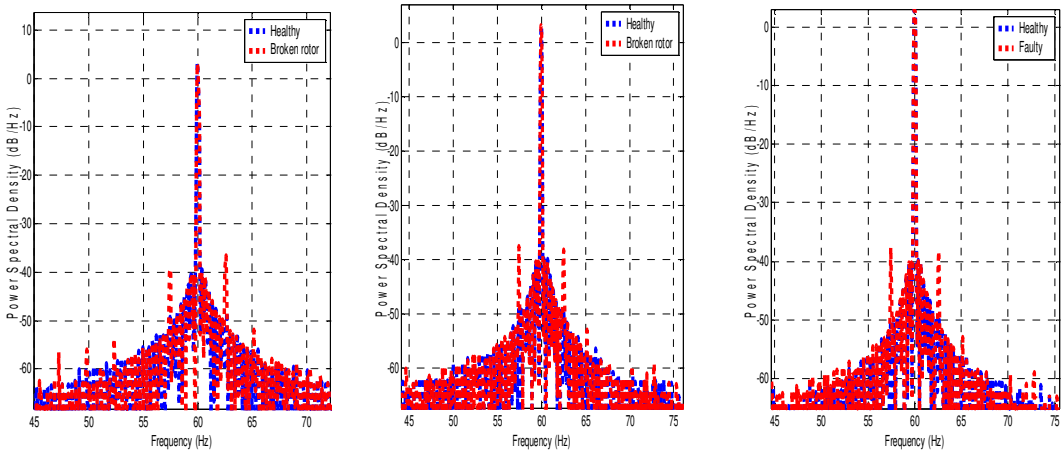

(a) Mains source (b) Drive source (c) Programmable source

Figure 4.12: First order sidebands for single broken rotor bar

In some installation cases the drive is mounted close to the motor, while the measurements or the current transformers (CT's) are installed inside substations, away from the motor. In this case, it is difficult to make test measurements from the motor side

of the drive and it is more convenient to take them from the line side of the drive, where the CT's are installed. To verify this point, a test was conducted where the CT and measurements were taken before the drive, to simulate a measurements from the substations CT's. The broken rotor bar sidebands are evident only for the four broken rotor bars as shown in Figure 4.13. However, the sidebands are not as high as in the case when the test is done from the motor lines of the drive, as shown previously. This is due to the large capacitance of the drive, which works as a filter and does not allow the harmonics of the signature to pass through to the line side of the drive. Also, in an industrial plant other loads may be connected at the line side and affect the detection of the sidebands.

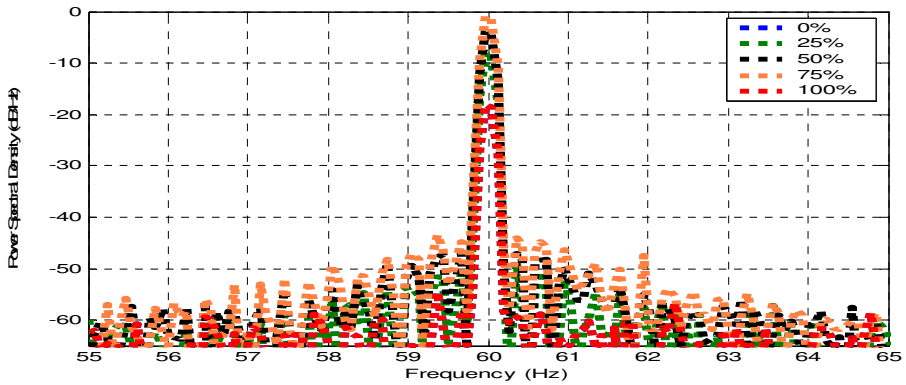

(a) Single broken rotor

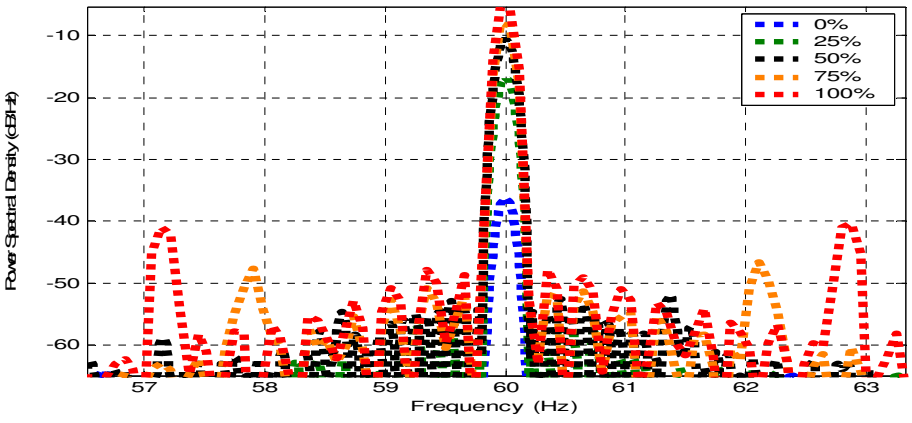

(b) Four broken rotor bars

Figure 4.13: Broken rotor sidebands with the data captured from the line side before the drive

Previous research [7] suggests that the number of broken rotor bars can be determined by:

$$n = \left[\frac{2R}{10^{N/20} + p} \right] \tag{4.8}$$

where n is the estimate of broken bar numbers, R is the number of rotor slots, N is the average dB difference between the lowest sideband components and the supply frequency component, and p is pole pairs. The table below shows the estimated number of broken rotor bars using the above equation from the three different sources (i.e., drive, programmable, and mains) at the motor full load scenario and 60 Hz:

Source of supply	*Single broken rotor*	*Four broken rotor*
Drive	0.745	2.556
Programmable	0.745	2.583
Mains	0.689	2.610

Table 4.4: Estimated number of broken rotor bar at different supplies and full load

However, the accuracy of this equation is not reliable for large number of broken rotor bars.

4.2.3 Negative and positive sequence analysis

For stator turn faults, the use of negative and positive sequence components of the phase current have shown some advantages in terms of fault diagnosis. These components are investigated for the broken rotor bar faults detection using the symmetrical component theory as described in Chapter 3. Because it has already been shown that the full rated load was optimum for achieving better results for broken rotor bar detection, the negative and positive approach has been applied only to the motor rated full load and at rated operating frequency at 60 Hz.

Analysis of the current show that neither the current negative-sequence content nor the positive-sequence content can provide notable lower or upper sidebands, as the main phase current sidebands fault indicates. Moreover, an exact match between the negative content sidebands of healthy and faulty motors, and similarly, an exact match between the positive content sidebands of healthy and faulty cases, makes it difficult to reveal the motor condition using only these contents. Also, this does not provide any helpful information about the interaction of the non-faulty conditions, such as load oscillations or supply voltage unbalance. The previous observations are shown for the case that the supply is directly from the mains. In this case a voltage unbalance tends to exist as depicted in Figure 4.14 for both the single and four broken rotor bars respectively.

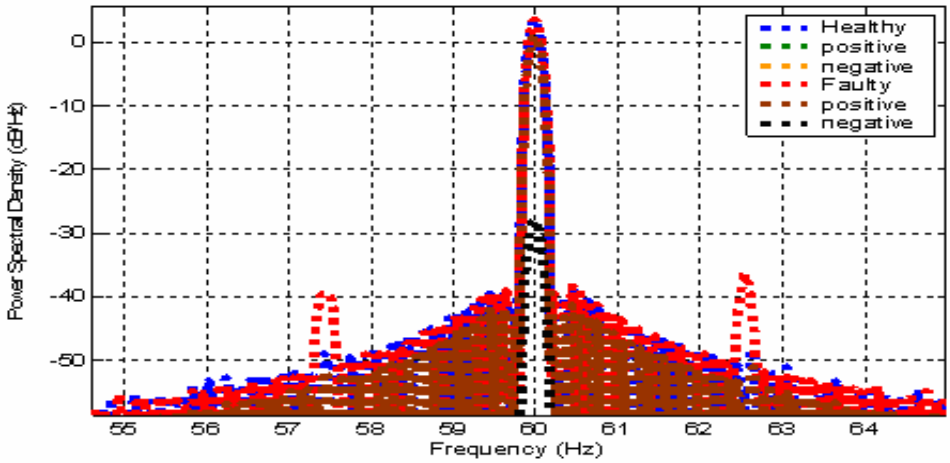

(a) One broken rotor bar

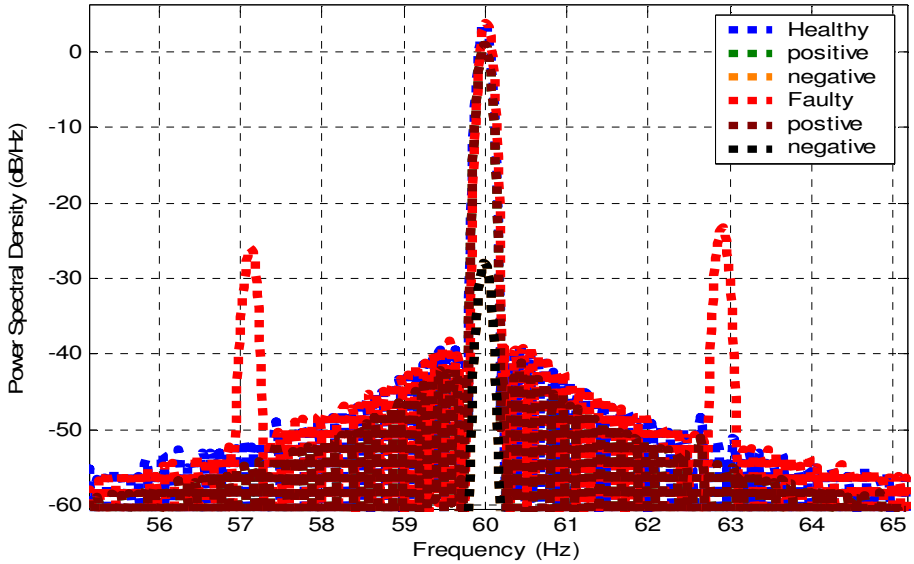

(b) Four broken rotor bars

Figure 4.14: Power spectral densities for the negative- and positive-sequence components for broken rotor bar sidebands with motor fed from mains supply

Better results were not obtained while the motor was fed from a pure sinusoidal source, as depicted in Figure 4.15. The elimination of supply voltage unbalance can not be observed in the sidebands of the positive or the negative contents.

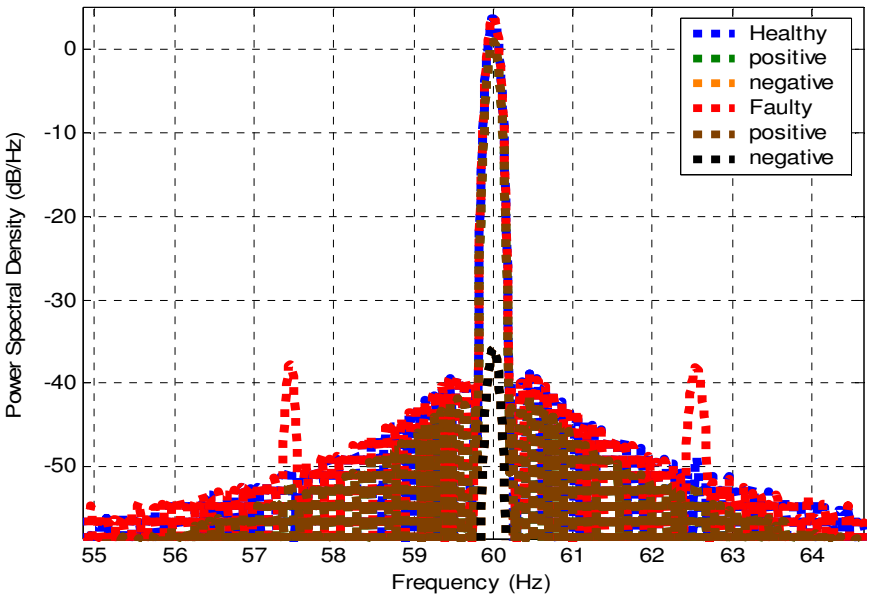

(a) One broken rotor bar

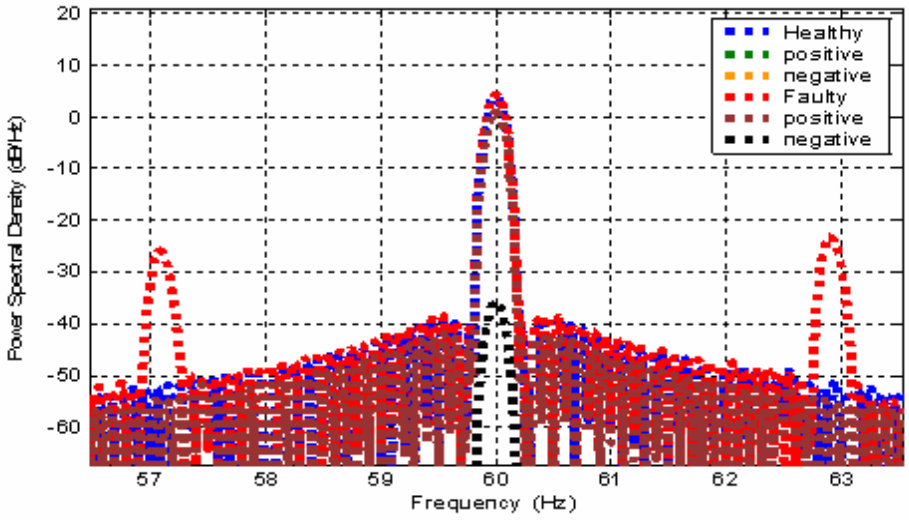

(b) Four broken rotor bars

Figure 4.15: Power spectral densities for negative and positive component for broken rotor bar sidebands with motor fed from a programmable supply

The drive harmonics and special voltage supply has not made a change to the negative and positive components as shown in Figure 4.16. Thus, it is concluded that negative and positive sequences analyses are not a useful tool, thus preventing their use during this research for measuring the magnitude of fault signals and the separation from any overwhelming torque ripples from the load.

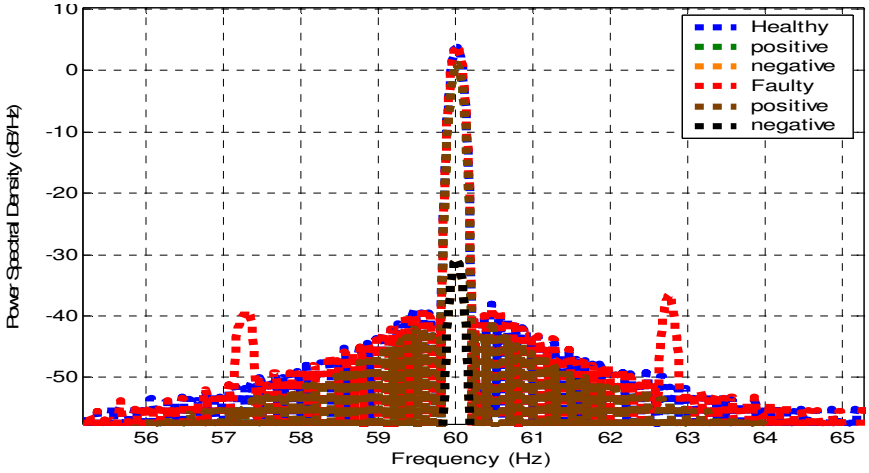

(a) One broken rotor bar

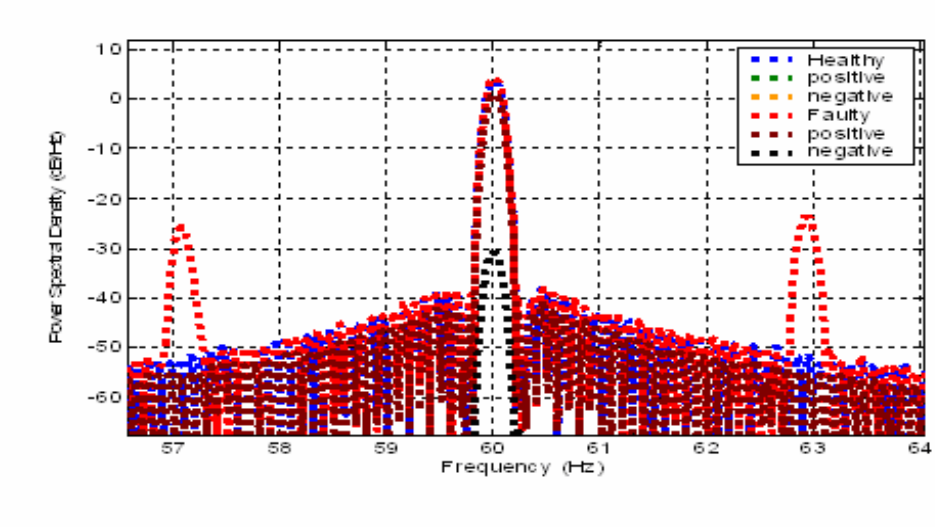

(b) Four broken rotor bars

Figure 4.16: Power spectral densities for negative and positive components for broken rotor bar sidebands with motor fed from drive supply

4.2.4 Park's vector approach analysis

As outlined in Chapter 3, the third approach of analyzing the current signature analysis for fault detection is using Park's vector theory. When using a programmable source, supplying a pure sinusoidal voltage signal to a healthy motor, the trajectory of Park's vector is a circle centered at the origin of the coordinates (shown in Figure 4.17). For a motor with a broken rotor bar as depicted on Figure 4.18 a deviation from the circle pattern is slightly evident. This deviation is even clearer for more severe cases, such as the four broken rotor bar, as shown in Figure 4.19.

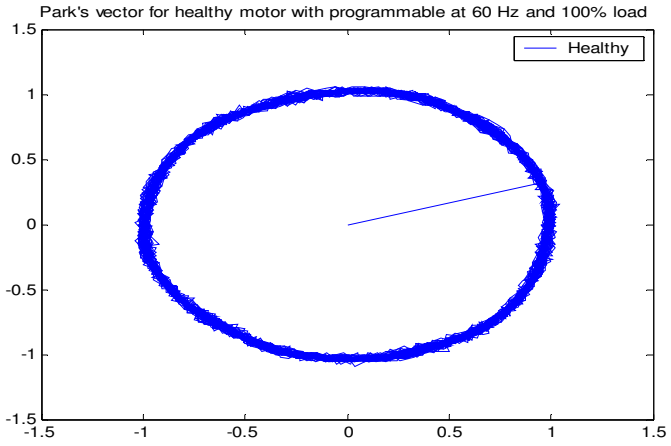

Figure 4.17: Park's vector for healthy motor fed from programmable source

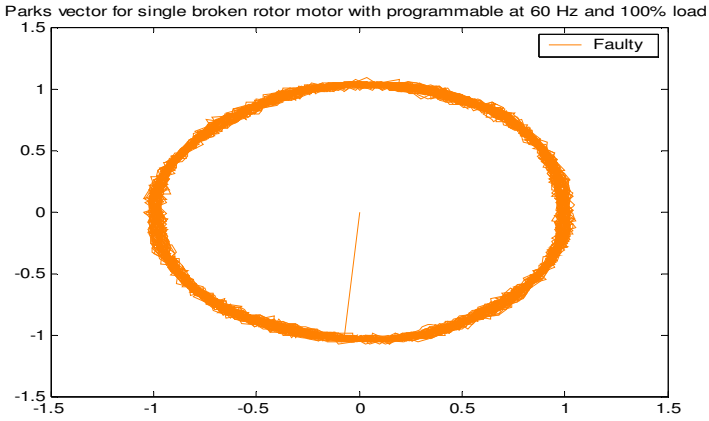

Figure 4.18: Park's vector for single broken rotor motor fed from programmable

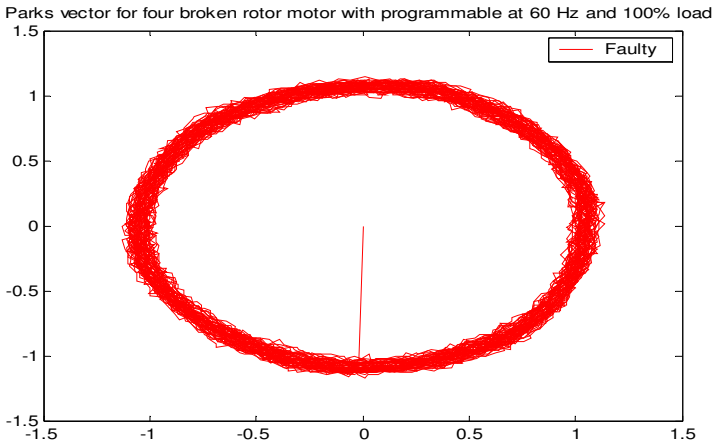

Figure 4.19: Park's vector for four broken rotor motor fed from programmable source

If a healthy motor is being supplied directly through the mains, the trajectory is not circular as depicted in Figure 4.20. This is mainly due to the voltage unbalances that can accompany such supplies, and which induce third harmonics and cause core saturation.

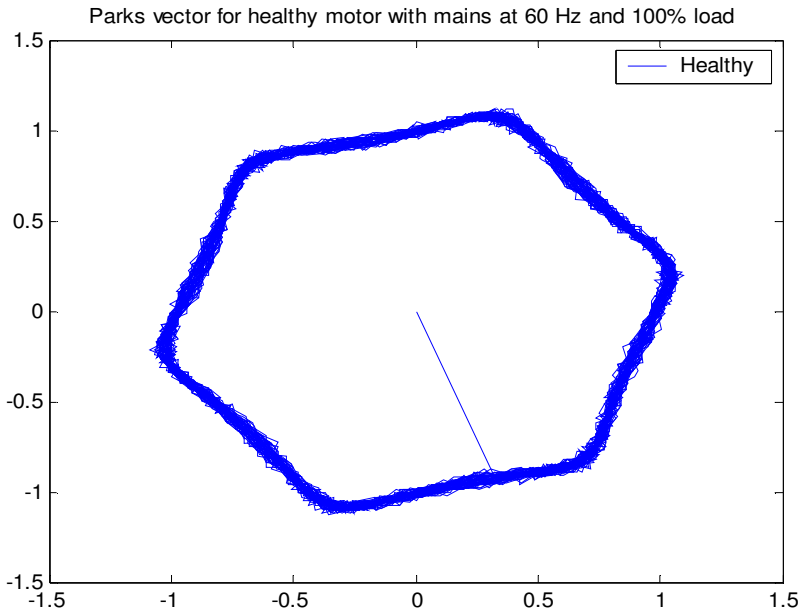

Figure 4.20: Park's vector for a healthy motor fed from mains

However, the change of pattern cluster could provide some indication of faults. Moreover, the change of rotation is not an indication of fault because it is mainly due to swapping of phases during the experimental setup. This is shown in Figure 4.21 for the single broken rotor bar and clearly evident in Figure 4.22 for the four broken rotor.

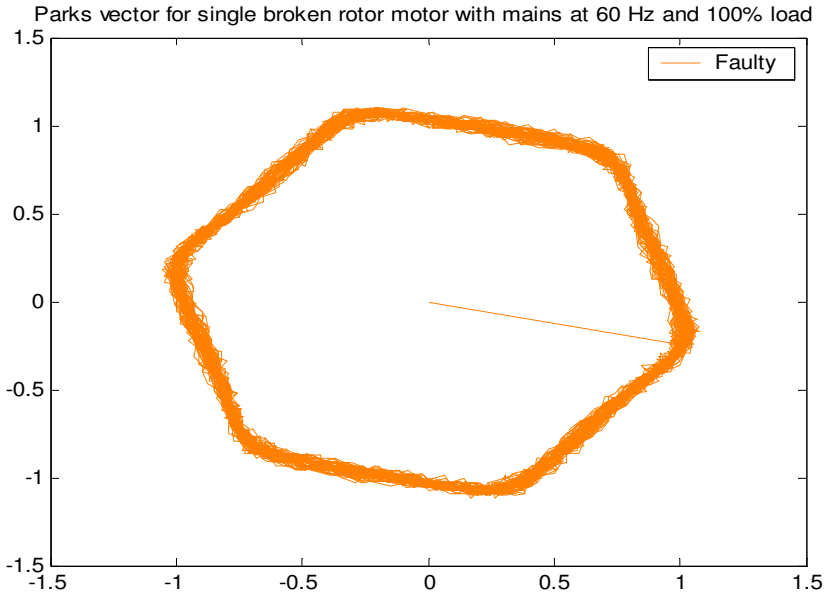

Figure 4.21: Park's vector for single broken rotor motor fed from mains

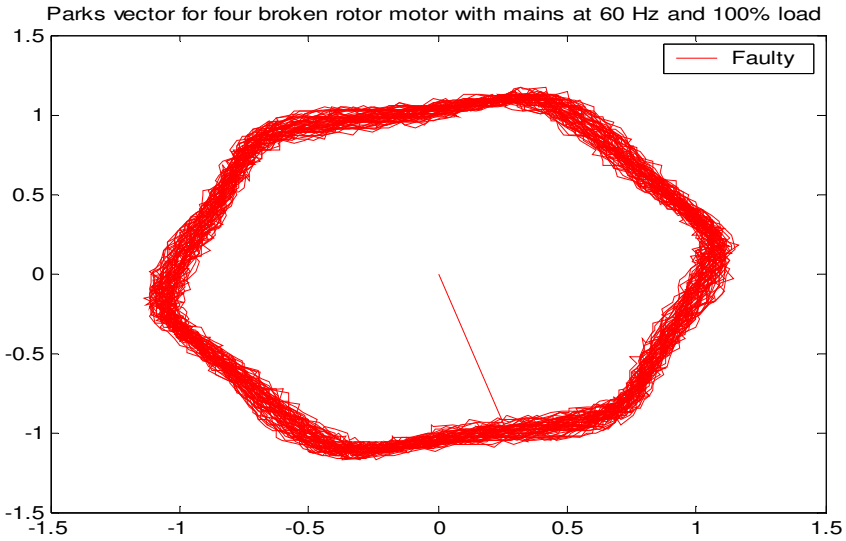

Figure 4.22: Park's vector for four broken rotor motor fed from mains

The drive uses a vector control theory which introduces the line to line voltages as a hexagonal shape (depicted in Figure 4.23). The non-uniform shape of this pattern is mainly due to the number of harmonics that the drive injects with the supply. Similar to the motors with programmable and mains supplies, the faulty motor with one broken

rotor bar is causing the trajectory to increase (as shown in Figure 4.24) and with the four broken rotor bars to increase even further (as shown in Figure 4.25).

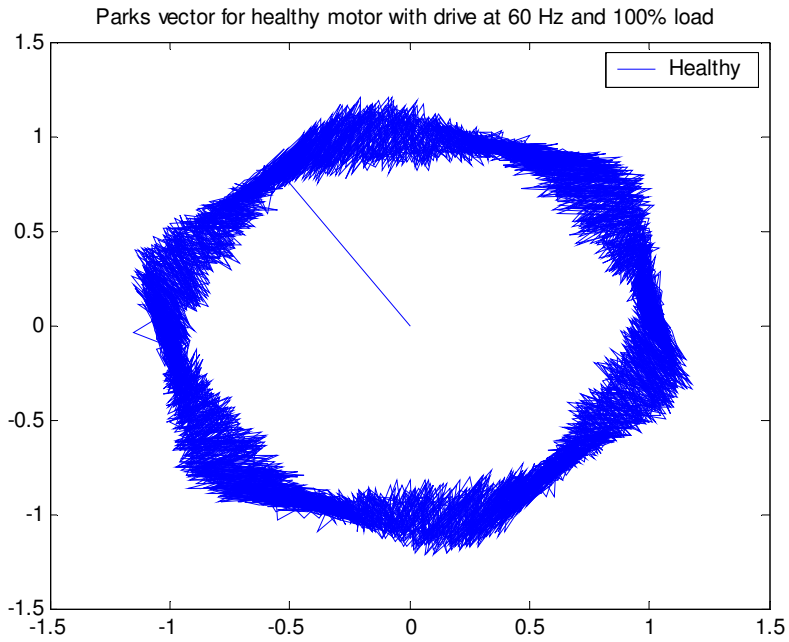

Figure 4.23: Park's vector for a healthy rotor motor fed from drive

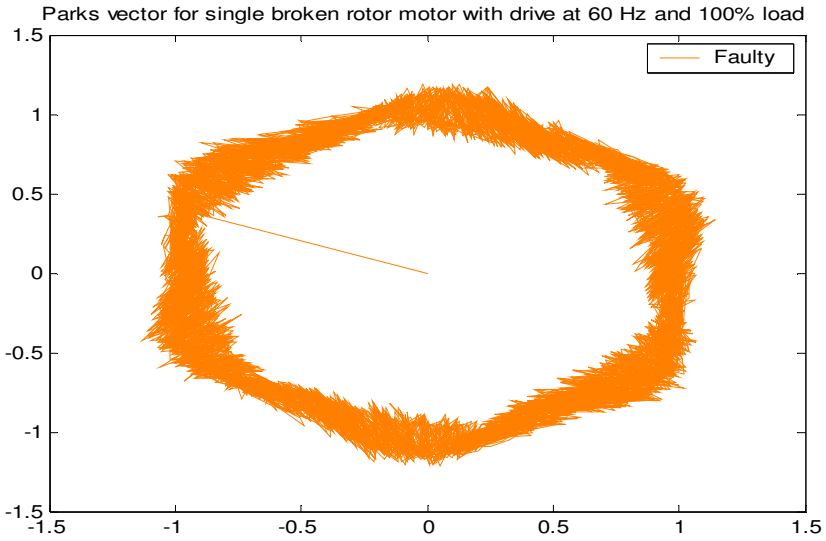

Figure 4.24: Park's vector for single broken rotor motor fed from drive

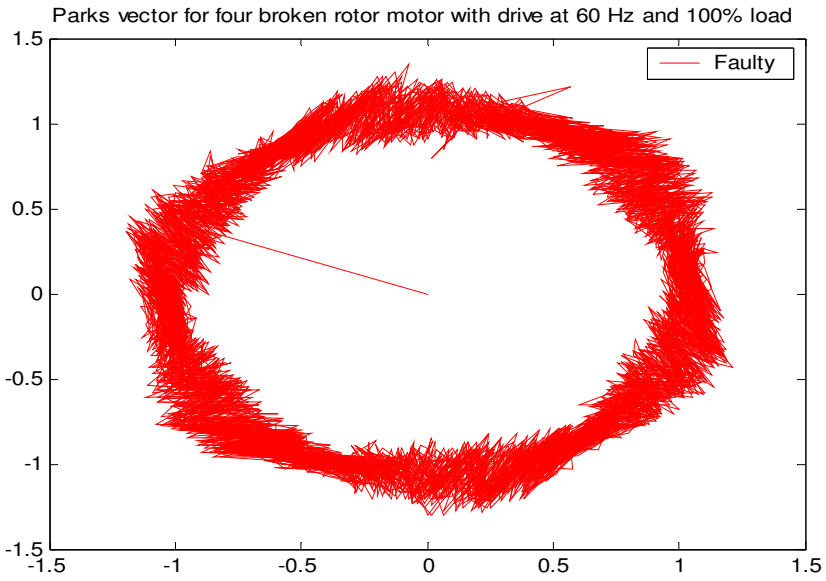

Figure 4.25: Park's vector for four broken rotor motor fed from drive

5. Air gap Dynamic Eccentricity

5.1 Analytical background

Machine eccentricity is the condition of unequal air-gap that exists between the stator and rotor [2, 10]. When eccentricity becomes large, the resulting unbalanced magnetic pull forces (UMP) can cause stator to rotor rub, and this can result in the damage of the stator and rotor. There are two types of air-gap eccentricity: the static air-gap eccentricity and the dynamic air-gap eccentricity. In the case of the static air-gap eccentricity, the position of the minimal radial air-gap length is fixed in space as shown in Figure 5.1(a). Static eccentricity may be caused by the ovality of the stator core or by the incorrect positioning of the rotor or the stator during manufacturing stage. If the rotor-shaft assembly is sufficiently stiff, the level of static eccentricity does not change. In case of dynamic eccentricity, the center of the rotor is not at the center of the rotation and the position of minimum air-gap rotates with the rotor as shown in Figure 5.1(b).

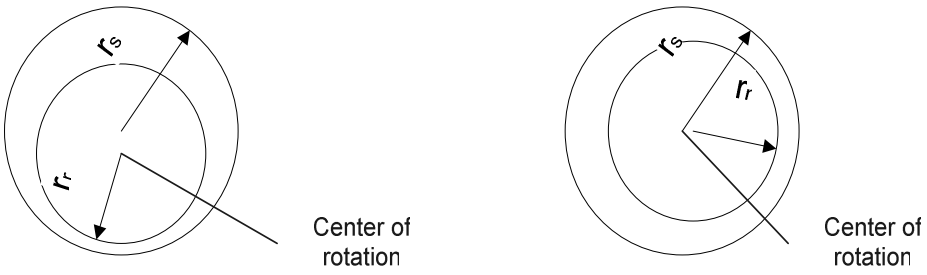

(a) Static eccentricity (b) Dynamic eccentricity

Figure 5.1: Different types of air gap eccentricity

This misalignment may be caused by several factors, such as a bent rotor shaft, bearing wear or misalignment, or mechanical resonance at critical speed. An air-gap eccentricity of up to 10% is permissible [16]. However, manufacturers normally keep the total eccentricity level even lower to minimize UMP and to reduce vibration and noise. In reality, static and dynamic eccentricities tend to co-exist. An inherent level of static eccentricity exists even in newly manufactured machines due to manufacturing and assembly methods .This causes a steady UMP in one direction. With usage, this may bend the rotor shaft, lead to bearing wear and tear, etc. The result might be some degree of dynamic eccentricity. Unless detected early, these effects may develop into stator to rotor rub, causing a major breakdown of the machine [20].

5.1.1 Eccentricity harmonics

As described by equation (4.1), the flux density in the air gap due to the current flowing in one of the phases winding is defined to be the product of the *MMF* and the air gap permeance *Pg*. Under ideal conditions, the permenace is constant because of the uniform air gap, however, in reality, the air gap length changes which causes a variation in the permenace. Theses variations can be expressed as either stationary [1, 12, 18, 19, 20]:

$$P_g(\varphi_s) = P_o + \sum_n P_n \cos\left[n\varphi_s + \alpha_n\right] \tag{5.1}$$

or rotating,

$$P_g(\varphi_s, \theta_m) = P_o + \sum_n P_n \cos\left[n(\varphi_s - \theta_m) + \alpha_n\right] \tag{5.2}$$

where P_o is the average air gap permeance and P_n is the magnitude of the n^{th} permeance variation. A stationary eccentricity, like that produced by a misalignment maintains a constant position through time and can be described as

$$P_g(\varphi_s) = P_o + P_1 \cos \varphi_s \tag{5.3}$$

where the air gap permeance of the machine is unaffected by changes in the rotor position. A rotating eccentricity, such that produced by a mechanical unbalance of the rotor, causes the air gap permeance to change over time since the rotor position moves from its initial position of $\theta_r = 0$ to a new position of $\theta_r(t) = wt$ at some later time t. This variations does not need to occur at only rotational velocity $w = w_{rm}$, but may be at any frequency. This variation can be described as:

$$P_g(\varphi_s, \theta_{rm}) = P_o + P_1 \cos(\varphi_s - \theta_{rm}) \tag{5.4}$$

The presence of static and dynamic eccentricity can be detected using MCSA [1, 2, 10, 12, 17, 18, 19, 20]. Two methods have been proposed for the detection of air gap eccentricity. The first monitors the behavior of the fundamental sidebands of the supply frequency. The frequencies of interest are predicted by equation:

$$f_{ec} = f_s \left[1 \pm m \left(\frac{1-s}{p/2} \right) \right] \tag{5.5}$$

where f_s is the electrical supply frequency, m=1,2,3,…, s is the per unit slip, and p is number of poles. The advantage of this method is that it does not require any knowledge of the construction of the motor in order to determine the characteristic frequencies.

The second method of detecting the air gap eccentricity monitors the current behavior of the sidebands of the slot frequencies. The sideband frequencies associated with an eccentricity are:

$$f_{slot+ec} = f_s \left[KR \pm n_d \left(\frac{1-s}{p/2} \right) \pm n_w \right] \tag{5.6}$$

where k= 1,2,3,…, R is the number of rotor slots, n_d is the order of the rotating eccentricity, and n_w is the order of the stator MMF harmonic. This scheme has the advantage of separating the spectral components produced by an air gap eccentricity from those caused by other sources; however, it has the disadvantage of requiring more knowledge of the motor construction, such as the number of rotor slots.

5.2 Experimental analysis

Air gap dynamic eccentricity faults can be implemented in the laboratory in three ways: rotor load unbalance, angular shaft misalignment and radial shaft misalignment. Only rotor load unbalances have been tested in this research. Steel bolts and nuts, weighting 220 grams, are placed in holes, which are drilled at different radial distances from the rotor shaft on a balanced metal disk (Figure 5.2). Tests at different loading levels and at different operating frequencies from different sources were conducted.

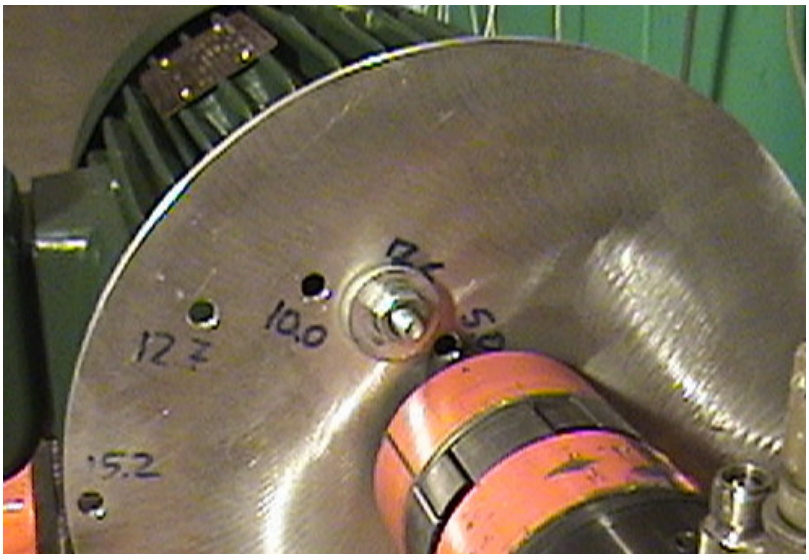

Figure 5.2: Experimental setup for dynamic eccentricity faults

5.2.1 Vibration monitoring test

An effective way to measure the level of unbalance on a machine is by measuring the level of vibration of the machine casing. This vibration test measures the absolute movements of the machine while the current signature measures the relative motion between the stator and the rotor, equivalent to the changes in the air gap [10, 18].

Four different levels of vibration tests were performed at 30 Hz, 40 Hz, 60 Hz and 80 Hz, and at three different loading levels: 50%, 75% and 100%. The vibration signal was measured using a standard CSI-2115 vibration signal analyzer mounted in horizontal position to the motor casing. Three different sources of supply were compared. The first load unbalance was made by placing the bolt and nuts 7.5 cm away from the shaft on the balanced disk. A programmable source was feeding the motor at different frequencies. The second case of load unbalance was similar to the first, but this time, the motor was fed through a 5 Hp Adjustable Speed Drive. In the third case, the supply from the mains was monitored at the normal 60 Hz supply frequency.

For the 30 Hz test, as depicted in Figure 5.3, the overall vibration eccentricity of the motor fed from a programmable source shows a slight increase in comparison to the drive case at all monitored loading levels. During the 40 Hz test, the differences between the programmable source and the drive for the same dynamic eccentricity level are small; however, the vibration magnitude in general is higher than in the 30 Hz case. At 60 Hz, the programmable source and the supply from mains show an increase of the vibration level as load increases; however, the results for the drive, which usually are lower than both the programmable source and the mains, has almost the same magnitude. For the 80 Hz test, an opposite result to all of the above tests is observed. The drive shows a higher magnitude of vibration than the programmable source. In this case the level of vibration remains almost constants as load increases, whereas the programmable source level of vibration decreases as load increases or speed decreases.

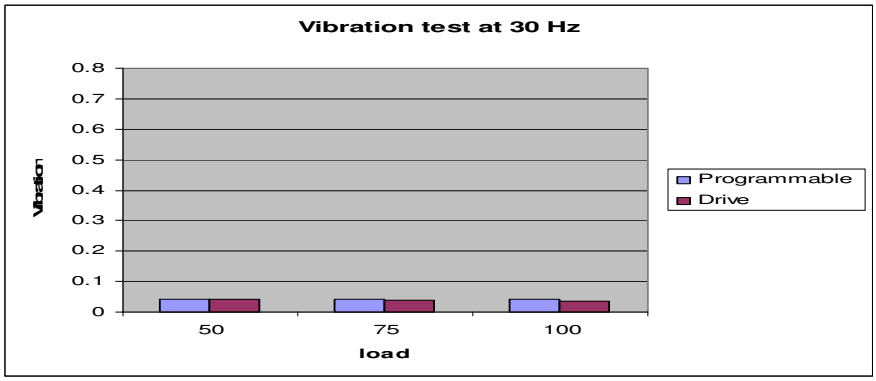

(a) 30 Hz

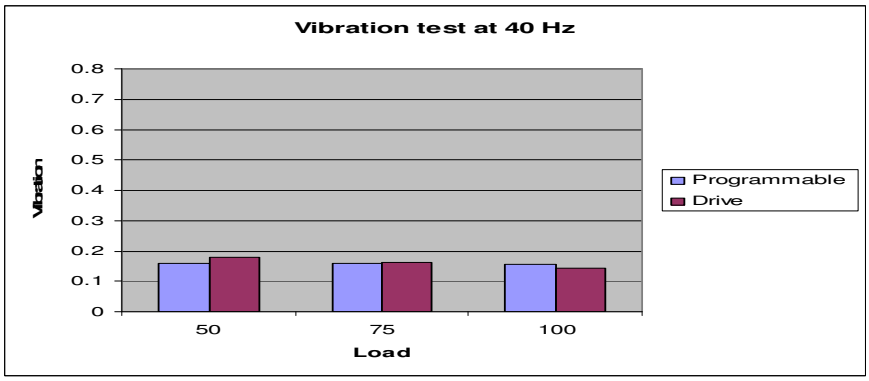

(b) 40 Hz

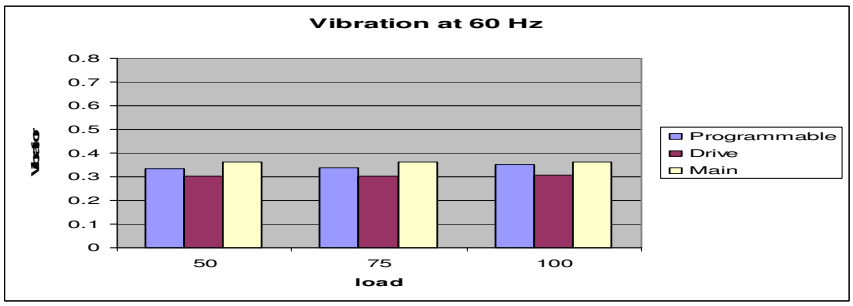

(c) 60 Hz

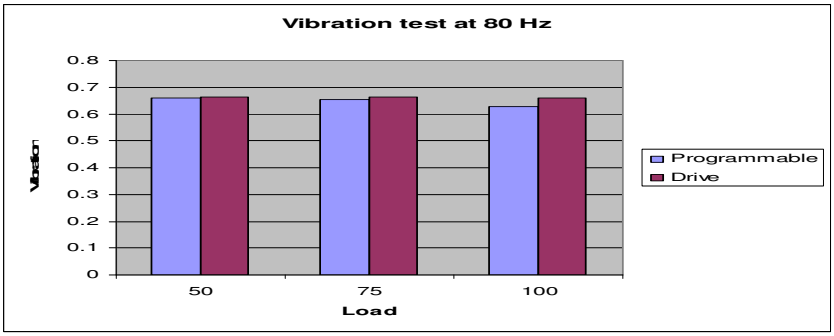

(c) 80 Hz

Figure 5.3: Different vibration tests levels

The vibration test doesn't provide a good indication for small air gap dynamic eccentricities, like the load unbalance at low level of frequencies; - it is hard to distinguish between faulty and healthy cases. However, it is reliable at frequency where, as shown in 60Hz and 80 Hz tests, both the programmable source and the drive have a very high level of vibration.

5.2.2 Current signature analysis

Similar tests to the vibration test were performed but this time the analysis was done using Motor Current Signature Analysis (MCSA). The following are the three main methods of analysis of the stator current used for the detection of air gap dynamic eccentricities. The algorithms used in these analyses are described in Chapter 3.

5.2.2.1 Power spectral density analysis

For the current signature analyses using the power spectral density Welch estimation method, four different frequencies were monitored, 30Hz, 40Hz, 60Hz and 80Hz, at nine different loading points. These were 0%, 10%, 25%, 35%, 50%, 65%, 75%, 90% and 100%. In order to have the similar test conditions, the level of dynamic eccentricity (load unbalance) was kept the same at all of the four frequency tests. For each test, the frequency was changed using two different sources: programmable source and an adjustable speed drive. For each source a healthy motor case was compared to a dynamic eccentricity case, under very similar conditions. Mains supply also was compared with the drive and the programmable source at 60 Hz.

The attempt here is to evaluate and validate the ability to detect the dynamic eccentricity faults using the current signature analysis by evaluating the well known eccentricity sideband harmonics that can be revealed from equation (5.5). The sidebands using this equation can be approximated using:

$$f_{ec} = f_s \pm m f_r \qquad \text{m= 1, 2, 3, etc} \tag{5.7}$$

where f_r is the rotor mechanical frequency. Table 5.1 summarizes the eccentricity sideband harmonics for all tested frequencies for different values of m.

f_s	*fr*	*fs+1fr*	*fs-2fr*	*fs+2fr*	*fs-2fr*	*fs+3fr*	*fs-3fr*
30	10	40	20	50	10	60	0
40	13.3	53.3	26.7	66.6	13.4	79.9	0.1
60	20	80	40	100	20	120	0
80	26.67	106.67	53.3	133.34	26.66	160.01	-0.01

Table 5.1: Dynamic eccentricity sideband harmonics at different frequencies

It is observed from this table that the eccentricity sidebands are the same for different values of m for the same frequency. For m = 3, the upper sideband is the second harmonic which in most cases is present also because of non-eccentricity problem. Only the first three sidebands, at m = 1, 2, and 3, show a significant magnitude that can be monitored for eccentricity fault detection, thus other non significant values are not considered in this research. Following is a summary of the four main tests.

Figure 5.4 shows the 30 Hz eccentricity sidebands at full load for the programmable source supply. The $f_s \pm f_r$ and the f_s+3f_r (the second harmonics) sidebands for the eccentricity case show a higher magnitude than the healthy case. For the same frequency but with supply from the drive (as depicted in Figure 5.5), only the *fs+3fr* or the second harmonic is present for both the healthy and the eccentricity cases. Moreover, the magnitude for the eccentricity fault is higher than in the healthy case. The other eccentricity sidebands even the first order at m=1, are not evident and it is clear that the drive has superimposed these harmonics. This makes it difficult to detect dynamic eccentricity faults at low frequency while the drive is being used to control the motor.

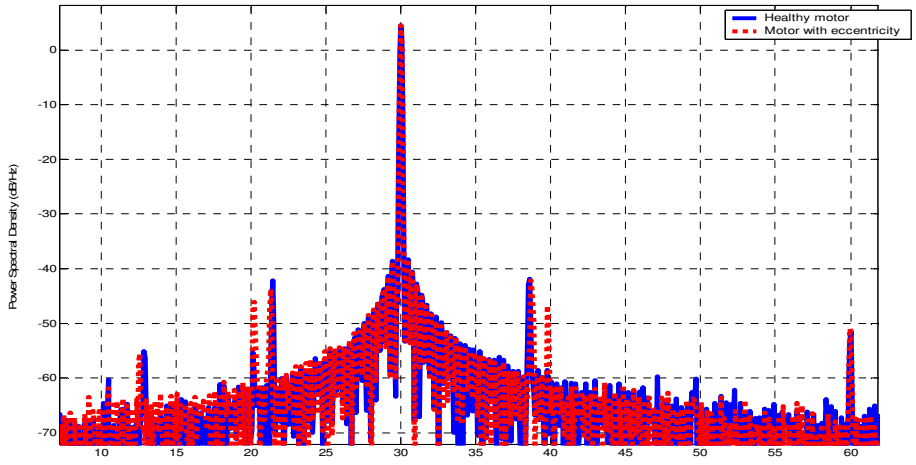

Figure 5.4: Power spectral density with programmable source at 30 Hz and full load

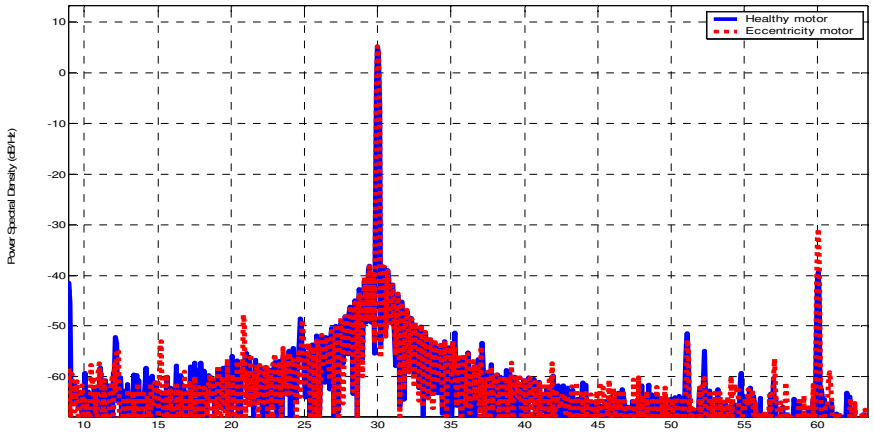

Figure 5.5: Power spectral density with drive source at 30 Hz and full load

For the same test at different load levels, Figures 5.6 and 5.7 depict the ratio of the lower sidebands (LSB) magnitude to the fundamental and the upper sidebands (USB) magnitude to the fundamental respectively. In each figure the healthy and eccentricity cases are compared for the programmable source and the drive cases. These charts show that the effective monitoring load levels for the eccentricity fault detection start from 75% for both of the LSB and USB. In general, the level of eccentricity decreases as speed decreases or as torque increases. The programmable source always has higher levels of

eccentricity than the drive, at all of the loading points. For the drive case it is hard to detect and differentiate between the healthy and eccentricity cases while it is easier and clear to do so for the programmable source.

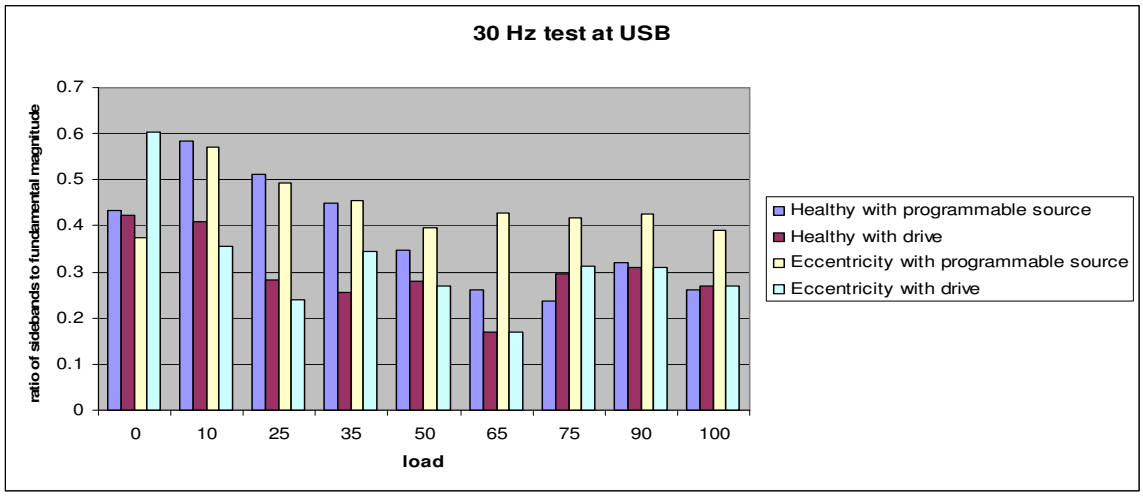

Figure 5.6: Dynamic eccentricity LSB at 30 Hz test at different load levels.

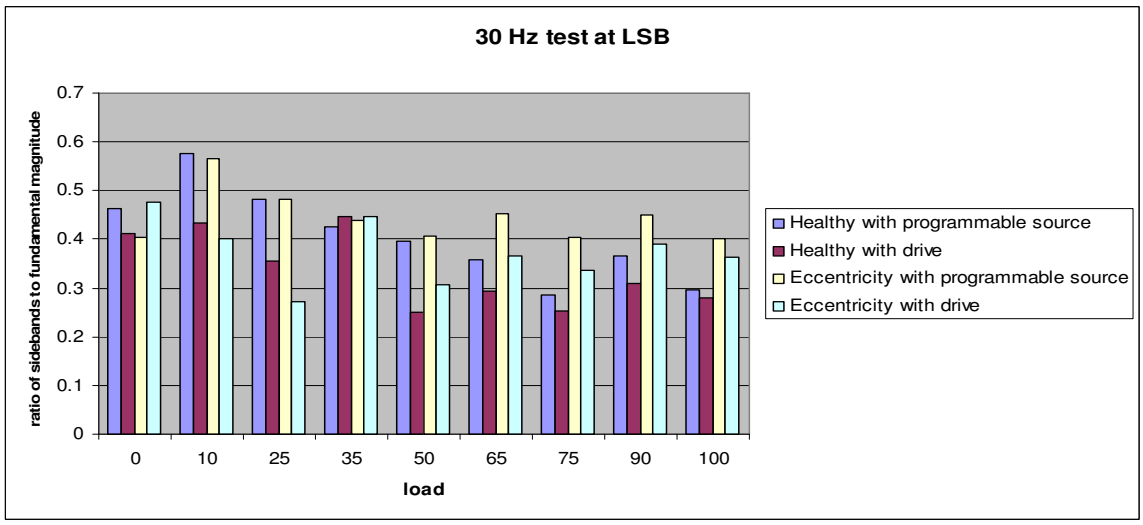

Figure 5.7: Dynamic eccentricity USB at 30 Hz test at different load levels

Figure 5.8 shows the eccentricity sidebands with the motor running at 40 Hz, supplied by the programmable source, at the rated full load. The first order sidebands for the eccentricity fault show a notable difference in comparison to the healthy case. Moreover, this magnitude is higher than in the 30 Hz case. When the motor is connected

to the drive more eccentricity sidebands start to appear at 40 Hz test than for the 30 Hz test, as shown in Figure 5.9. Only the lower sideband, *fs-fr* shows a distinguishable magnitude between the eccentricity and the healthy cases.

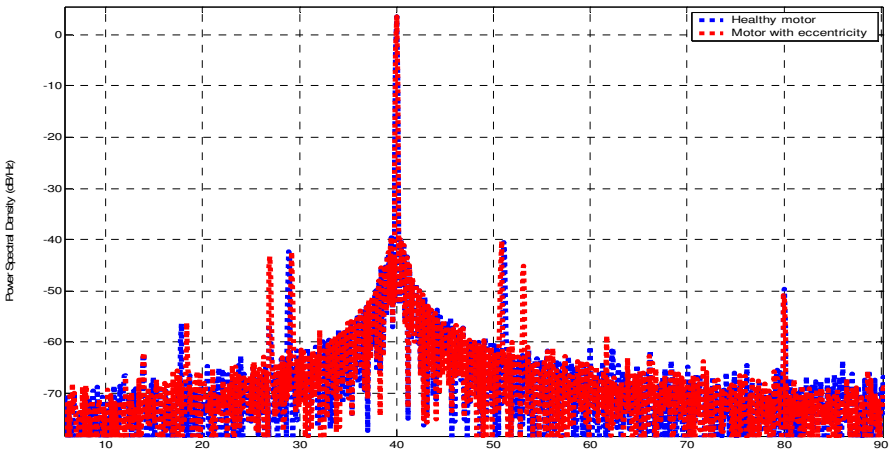

Figure 5.8: Power spectral density with programmable source at 40 Hz and full load

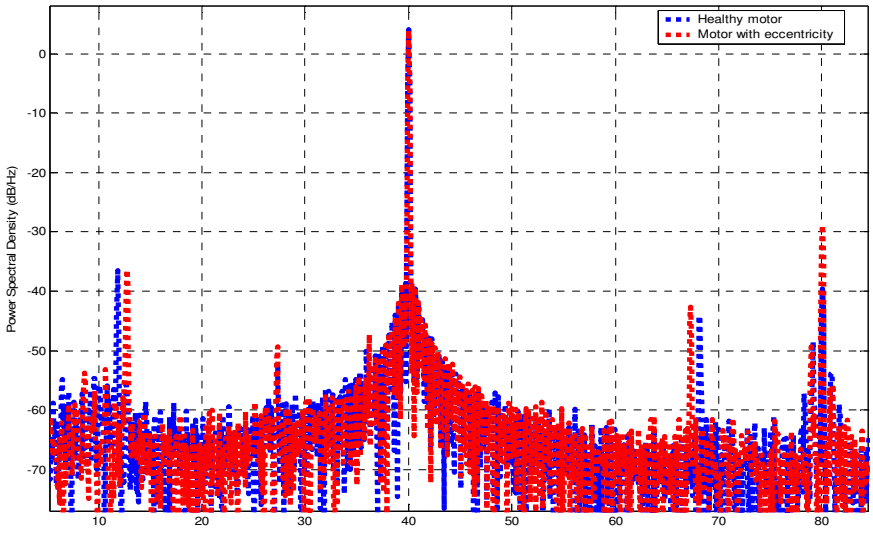

Figure 5.9: Power spectral density with drive source at 40 Hz and full load

For the same 40 Hz test but at different load levels, Figures 5.10 and 5.11 depict the ratio of the *fs*±*fr* lower and upper sidebands magnitude to the fundamental magnitude respectively (for the programmable and the drive cases). These charts show that the effective monitoring load level for the eccentricity faults start at 75% loading. This is for both sidebands. The programmable source always has higher levels of eccentricity than the drive at all of the loading points. At loading points less than 50%, the healthy case shows higher level of eccentricity than the applied dynamic eccentricity fault, both for the drive and the programmable source. However, at more than 50 % the eccentricity case starts to have higher and consistent magnitudes, and increases as load increase. This is more evident in the programmable source case more than in the drive case.

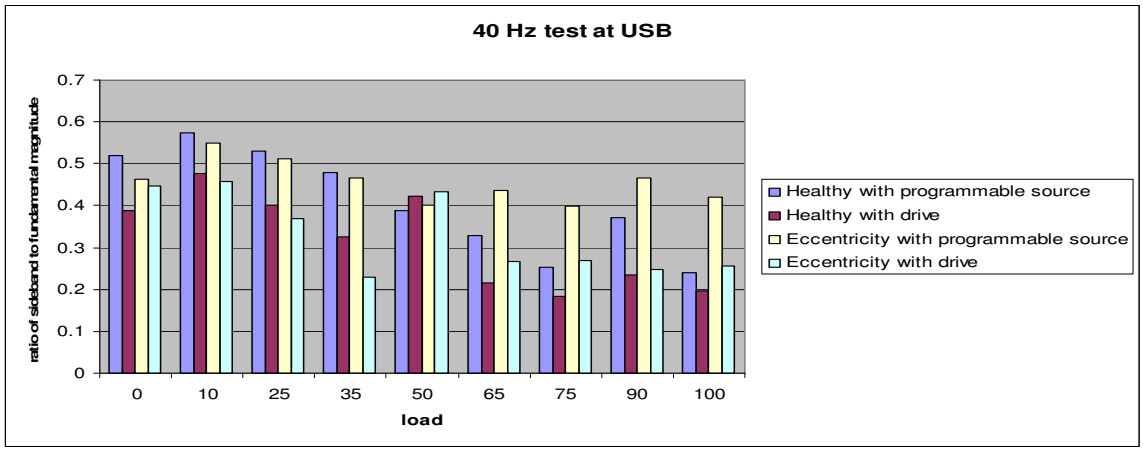

Figure 5.10: Dynamic eccentricity LSB at 40 Hz test at different load levels

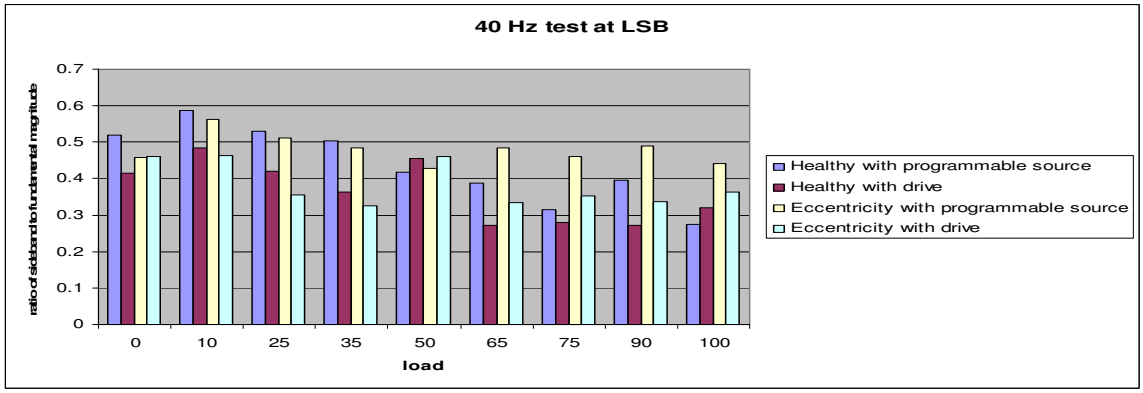

Figure 5.11: Dynamic eccentricity USB at 40 Hz test at different load levels

During the 60 Hz test, a supply from the mains was compared with the programmable and drive sources. The first order sidebands, for all of the three supplies, show the same magnitude of eccentricity, as shown in Figures 5.12, 5.13, and 5.14. The upper sidebands for the *fs*±*2fr* and *fs*±*3fr* are present for the supply from the mains and drive, therefore, provide good indication of the eccentricity fault.

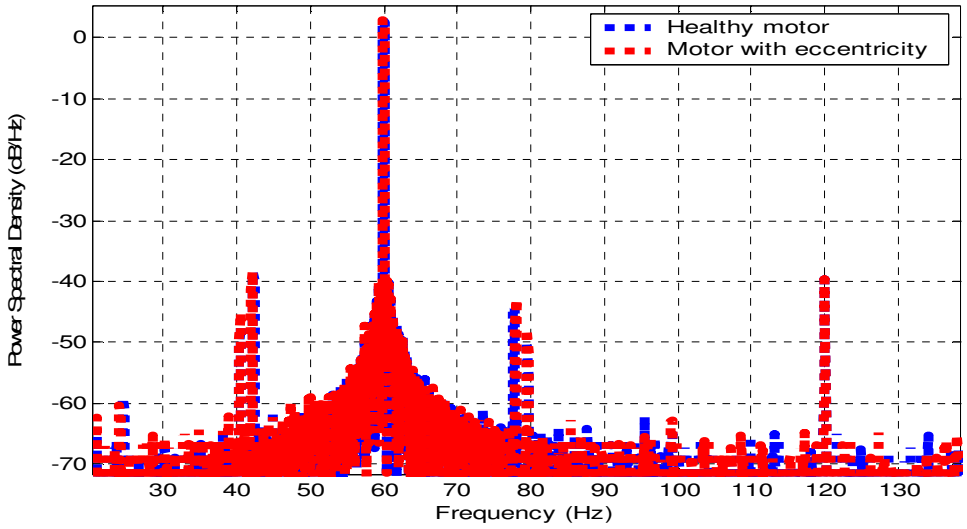

Figure 5.12: Power spectral density with programmable source at 60 Hz and full load

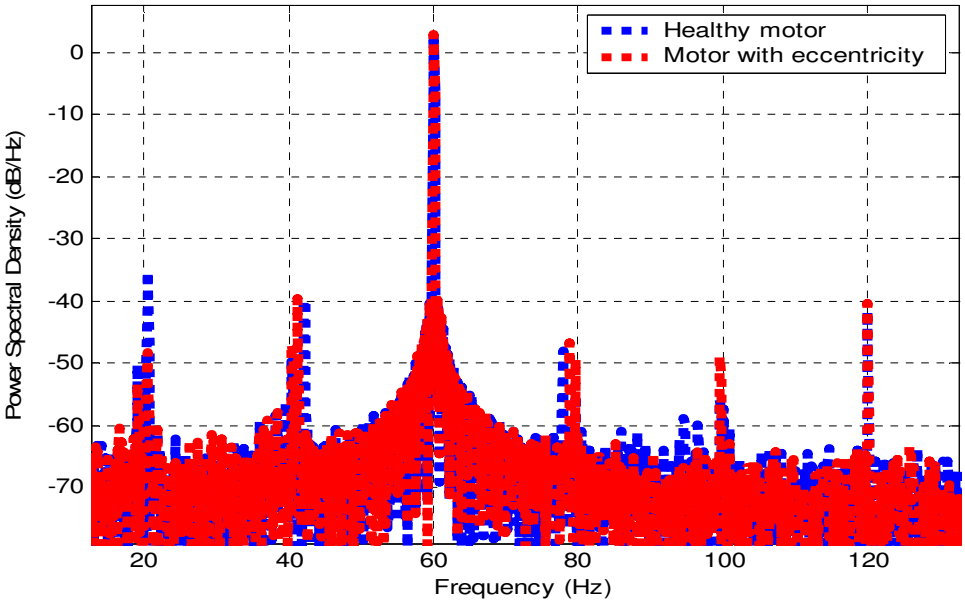

Figure 5.13: Power spectral density with drive source at 60 Hz and full load

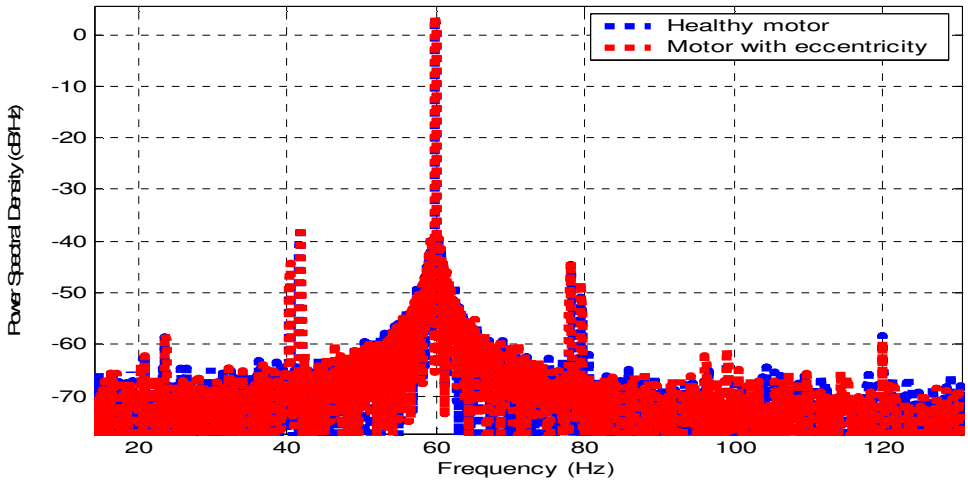

Figure 5.14: Power spectral density with mains source at 60 Hz and full load

For the same 60 Hz test and at different load levels, Figures 5.15 and 5.16 depict the ratio of the first order lower sidebands magnitude to the fundamental and the upper sidebands magnitude to the fundamental respectively. Healthy and eccentricity sidebands magnitudes are shown for the programmable, drive and mains supply sources. Unlike the 30 Hz and 40 Hz tests, this test shows only small differences between the eccentricity and the healthy cases. It is evident from these charts that the effective monitoring load level for the eccentricity faults detection start at 75% for both of the $fs \pm fr$ sidebands.

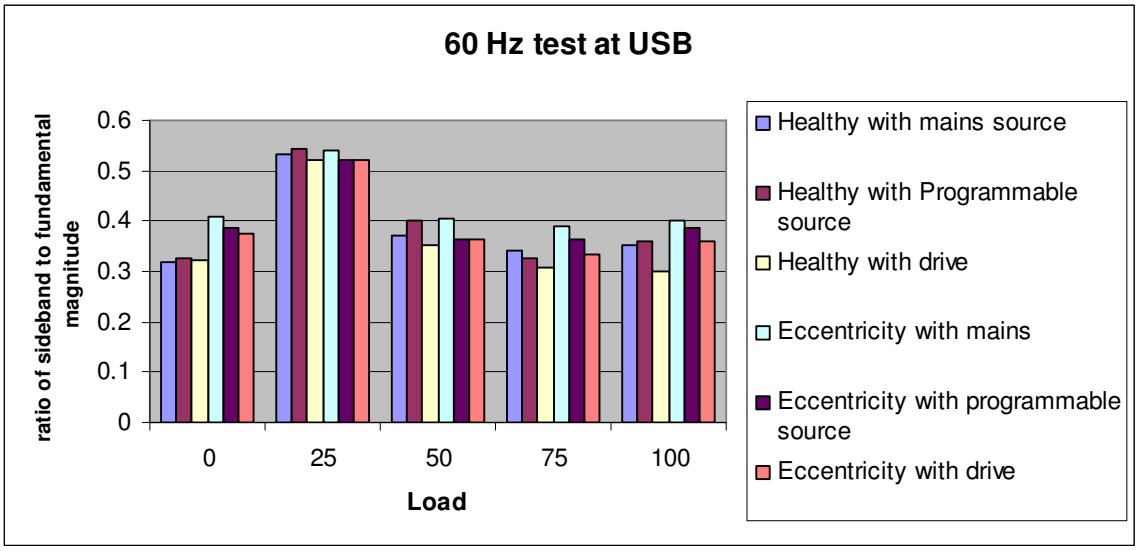

Figure 5.15: Dynamic eccentricity LSB at 60 Hz test at different load levels

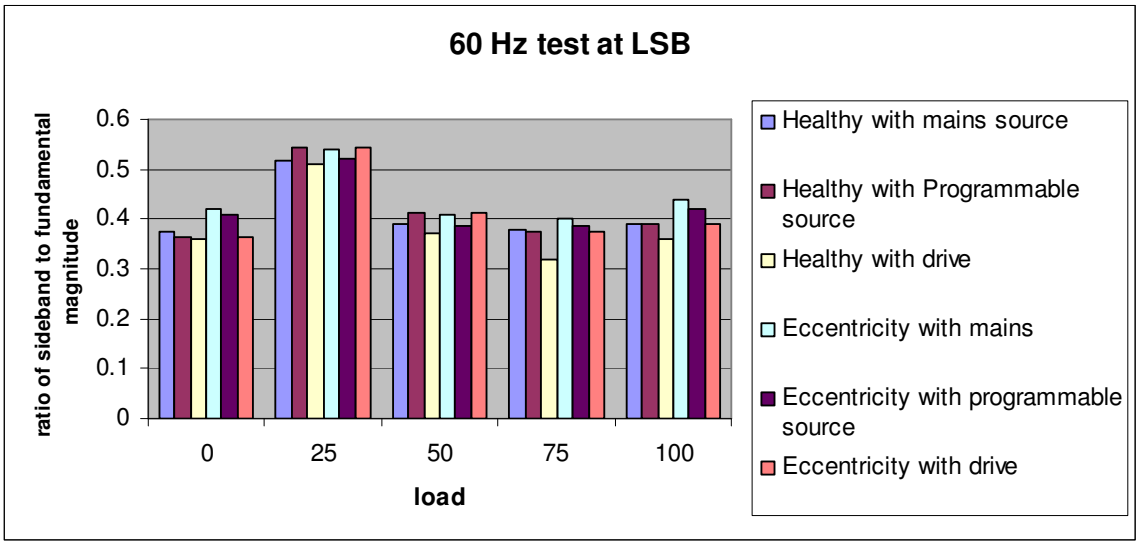

Figure 5.16: Dynamic eccentricity USB at 60 Hz test at different load levels

Operation at higher than the normal 60 Hz frequency, for example 80 Hz, is shown in Figures 5.17 and 5.18 for the programmable source and drive respectively. The drive starts to inject more harmonics of which only the first order sidebands at $fs \pm fr$ and the upper sideband of $fs+3fr$ reflect the magnitude of the dynamic eccentricity fault. On the other hand, the programmable source has fewer harmonics and overall shows a higher magnitude for the eccentricity case than the healthy one.

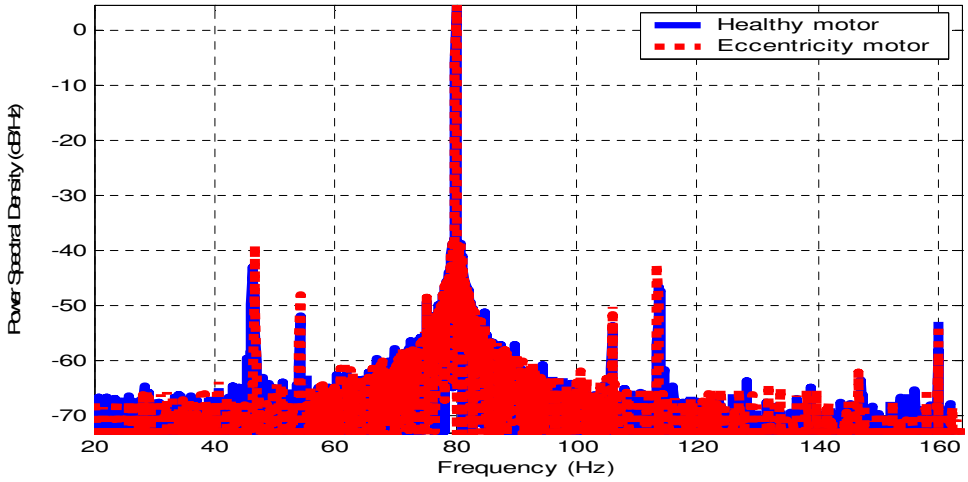

Figure 5.17: Power spectral density with programmable source at 80 Hz and full load

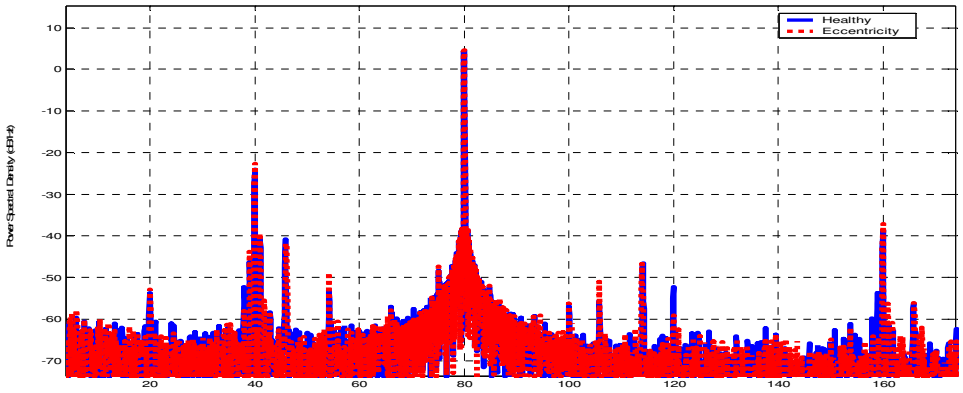

Figure 5.18: Power spectral density with drive source at 80 Hz and full load

For the same 80 Hz test, Figure 5.19 shows the ratio of the upper sideband magnitude to the magnitude of the fundamental for the first order eccentricity at different loading levels. At all of the loading points, the dynamic eccentricity case with drive is showing a higher magnitude than the healthy case. However, this is only true and consistent for the programmable source at loading points of more than 65%. Figure 5.16 shows the ratio of the lower sideband magnitude to the magnitude of the fundamental for the first order eccentricity at different loading levels. With eccentricity, the drive started to show higher and consistent magnitude more than the healthy case at loading points of more than 25%. For the programmable source this is only true for loads of more than 65%. Moreover, both the drive and the programmable source have a very similar level of eccentricity at most of the loading levels - not the case for all of the other tests.

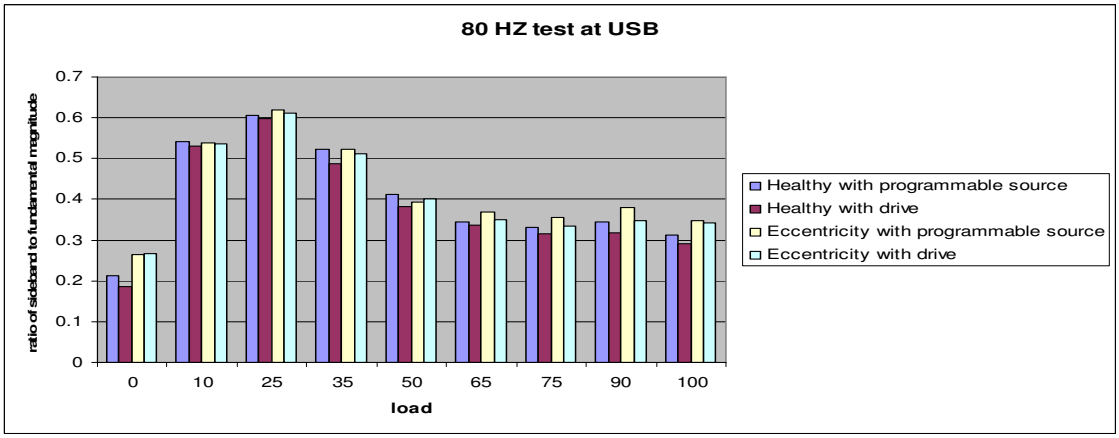

Figure 5.19: Dynamic eccentricity LSB at 80 Hz test at different load levels

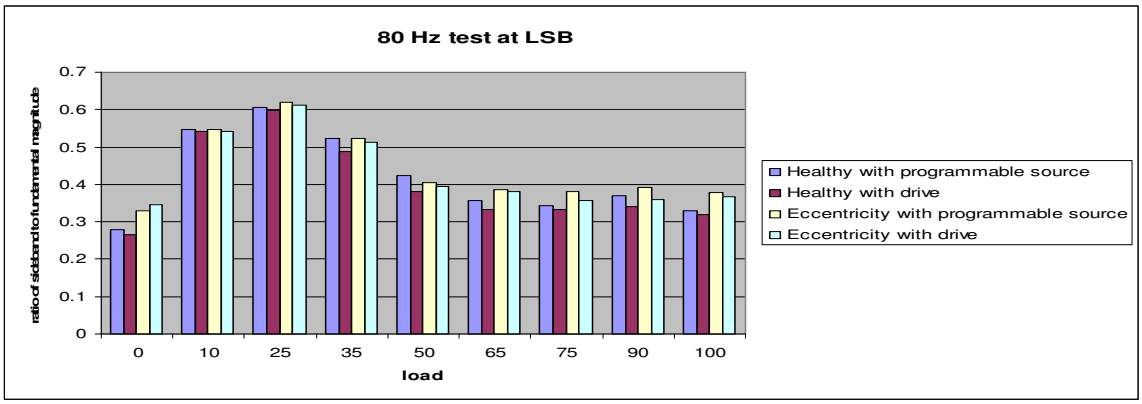

Figure 5.20: Dynamic eccentricity LSB at 80 Hz test at different load levels

In summary, dynamic eccentricity faults detection, while the motor is being controlled by the drive is not effective at low level of frequencies and especially at low load levels. However, for normal, 60 Hz operating frequency, and higher, the drive has shown a clearer reflection of the dynamic eccentricity condition, even more so than the programmable source supply. Nevertheless, the dynamic eccentricity faults can still be detected, regardless of the supply source, by using the Current Signature Analysis (MCSA) power spectral density sideband harmonics. But this is only true at high loads, typically, more than 65%.

5.2.2.2 Dynamic eccentricity severity test

Different severity levels of unbalances were created by moving the bolts and nuts in the holes on the balanced disk. Three levels of severity were tested starting at 10 cm radial distance from the shaft and ending at 15.2 cm, towards the edge of the disk. The force acting on the shaft increase as the radial distance increases between the bolt and the shaft. This force as calculated using equation (5.8) and is a function of rotor speed squared.

$$F = m \cdot r.\omega^2 \tag{5.8}$$

where F is in newtons, m in kilograms, r is in meters and ω is in radian/sec. Table 5.2 shows the calculated force for each of the three levels of dynamic severity, at different speeds, using the same bolt and nuts described above.

Speed(Hz)	*F at 10 cm Level 1*	*F at 12.7 cm Level 2*	*F at 15.2cm Level 3*
40	154.4	1960.88	29805.38
60	347.4	4411.98	67062.1

Table 5.2: Forces at three different levels of eccentricity

These tests were conducted at two different frequencies, namely at 60 Hz and 40 Hz. This showed the effects of changing frequency using the drive on the detection of the dynamic eccentricity sidebands. Figure 5.21 shows the three levels of dynamic eccentricity for the 40 Hz test upper sideband (USB). The level of eccentricity can not be detected clearly before the 50% loading is achieved. However, as load increases to more than 50% a clear difference between the three levels is visible in the right order of eccentricity severity.

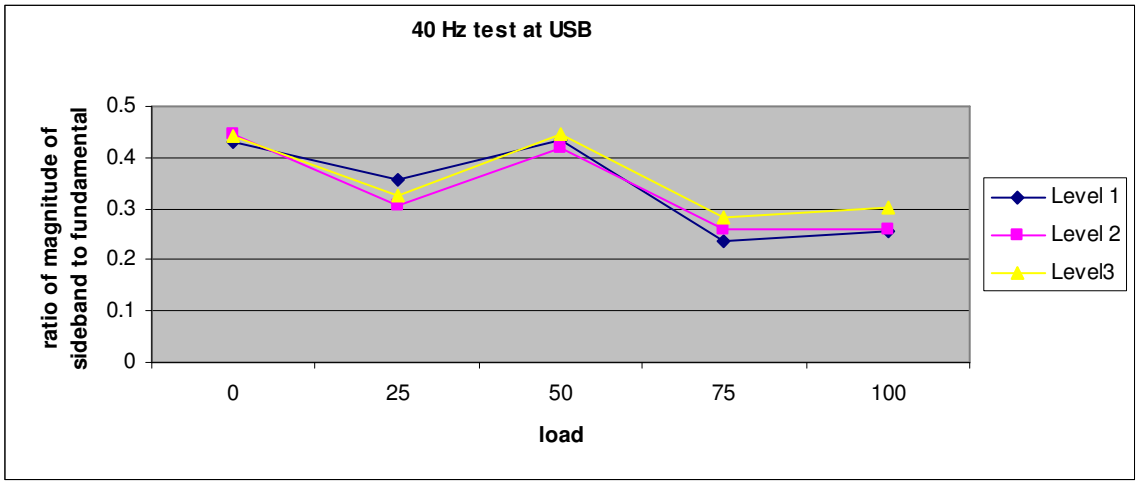

Figure 5.21: Different level of eccentricity at 40 Hz USB

Figure 5.22 shows the three levels of dynamic eccentricity for the 40 Hz test lower sideband (LSB). Only after the 75% loading, where the levels of eccentricity start to have the right order of eccentricity severity (level three and level two have higher magnitude than level one).

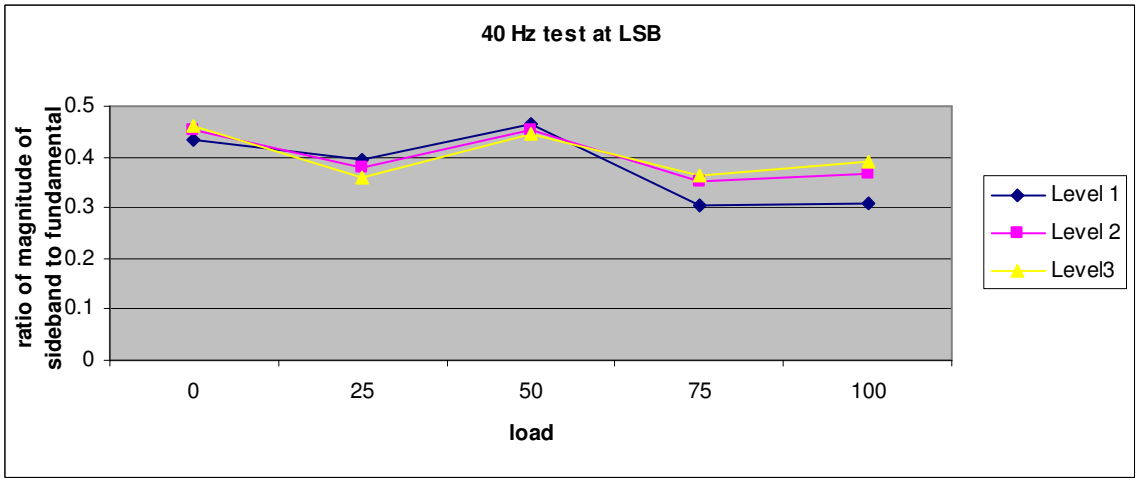

Figure 5.22: Different level of eccentricity at 40 Hz LSB

Figure 5.23 shows the three levels of dynamic eccentricity for the 60 Hz test upper sideband (USB). It is hard to distinguish between the three levels of eccentricity, except at 100% loading, where level one and level two have almost the same magnitude.

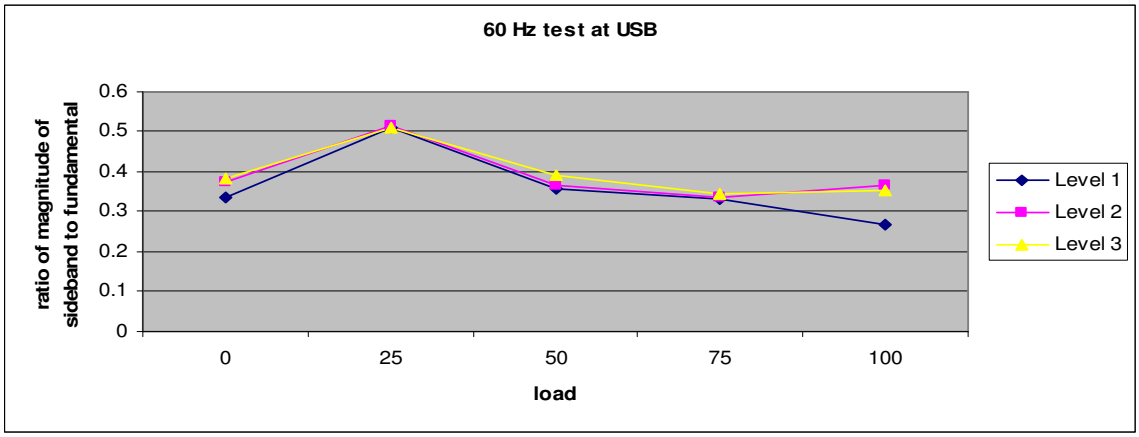

Figure 5.23: Different level of eccentricity at 60 Hz USB

Figure 5.24 shows the three levels of dynamic eccentricity for the 60 Hz test lower sideband (LSB). At most of the loading points, all of the three levels of eccentricity have the same magnitude. This makes it difficult to identify the severity of dynamic eccentricity by looking only to this sideband.

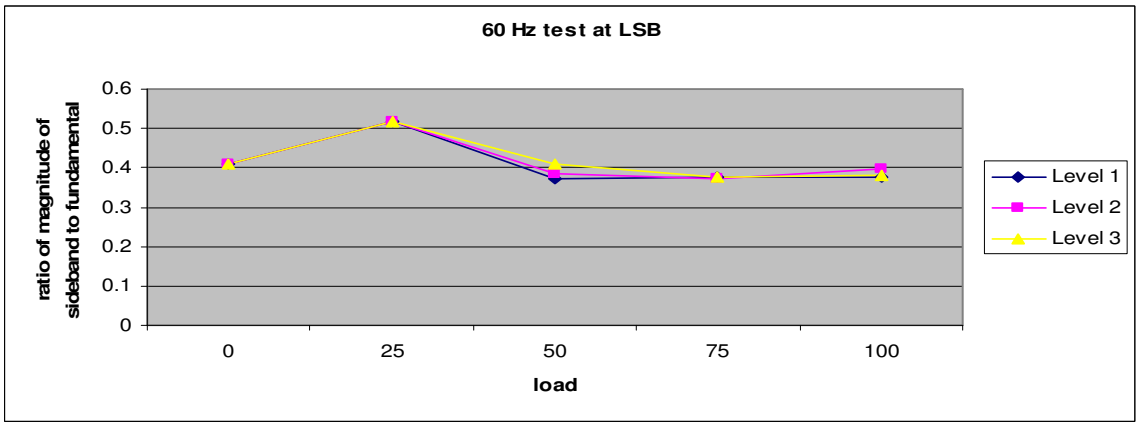

Figure 5.24: Different level of eccentricity at 60 Hz LSB

Both the 40 Hz test and 60 Hz test show that only the upper sidebands give a good and consistent indication of the severity of the dynamic eccentricity fault .This is only true as load increases or as speed decreases.

5.2.2.3 Negative and positive sequence analysis

From the previous sections it can be concluded that the first order sidebands at $fs \pm fr$ and the upper side of the third order sidebands $fs \pm 3fr$ are the most informative harmonics that can reveal eccentricity faults. In this section these have been investigated further to analyze non-fault conditions like torque pulsation and voltage unbalance which might provide misleading results about the health of the motor. These sidebands have been analyzed, only at the rated full load and at 60 Hz, using the negative and positive components approach as outlined in Chapter 3. Similar to the above analyses, the three sources of supply, drive, programmable source and mains were compared.

Figure 5.25 shows the negative and positive components for the three sidebands when the motor is fed from the mains. The negative and positive components of the eccentricity case show an increase in magnitude, in comparison to the healthy case, for both of the sidebands of $fs \pm fr$. However, the healthy case for the upper sideband at $fs+3fr$ shows higher magnitude than the eccentricity case. This leads to the conclusion that, when motor is fed from the mains supply, only the sidebands of $fs \pm fr$ are less affected by the non-fault conditions and can provide consistent information in monitoring for eccentricity faults detection.

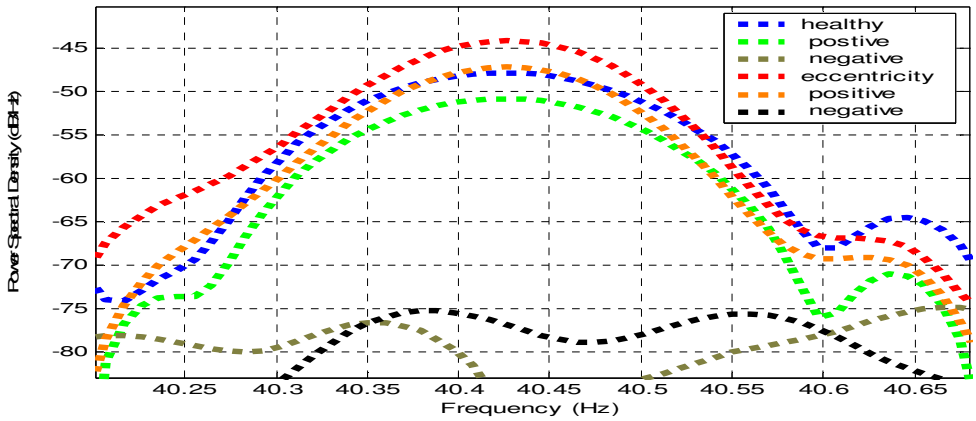

(a) Lower sidebands of *fs±fr*

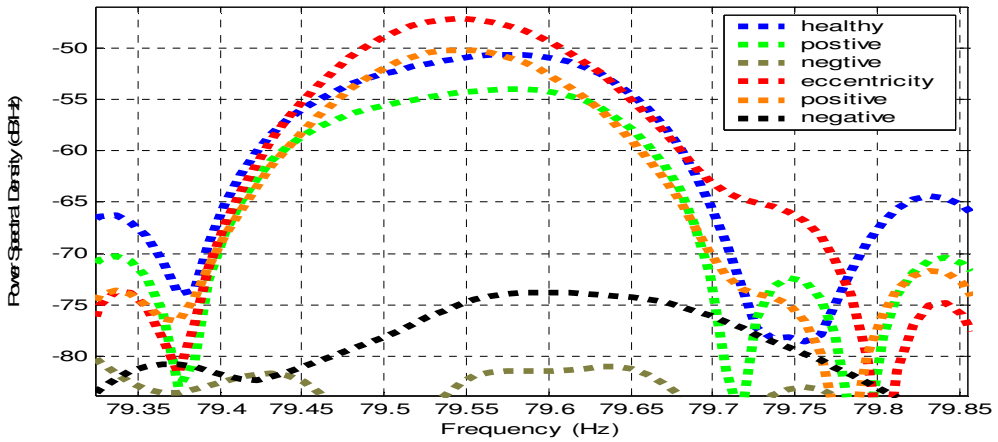

(b) Upper sidebands of *fs±fr*

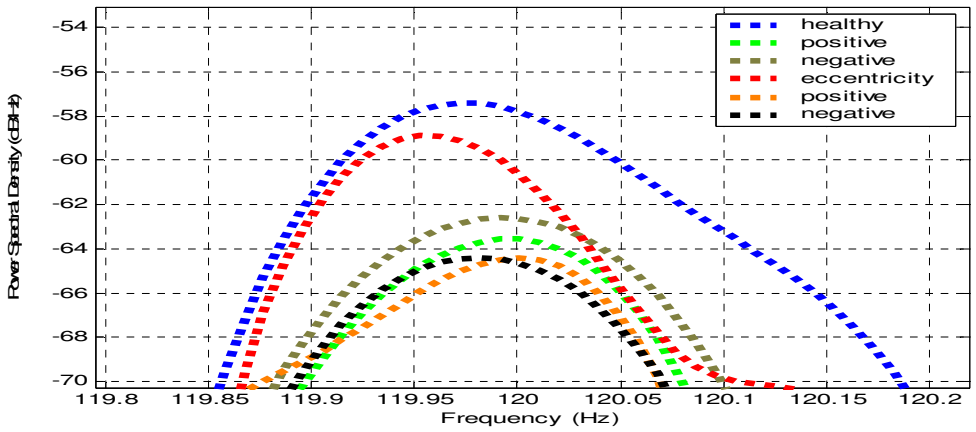

(c) Upper sidebands of *fs±3fr*

Figure 5.25: Negative and positive components for healthy vs. eccentricity with mains supply at 60 Hz and full load motor

Figure 5.26 shows the same sidebands positive and negative components for the case when motor is supplied from a pure sinusoidal supply like the programmable source. The negative sequence component of the upper sideband at *fs+3fr* has the same magnitude for both the eccentricity and healthy cases. However, this doesn't provide any good indication about the condition of the motor eccentricity problem but proves that the first order sidebands are less affected by disturbances in the supply source. These disturbances, for example a voltage unbalance, are controlled to a minimum when using a programmable source.

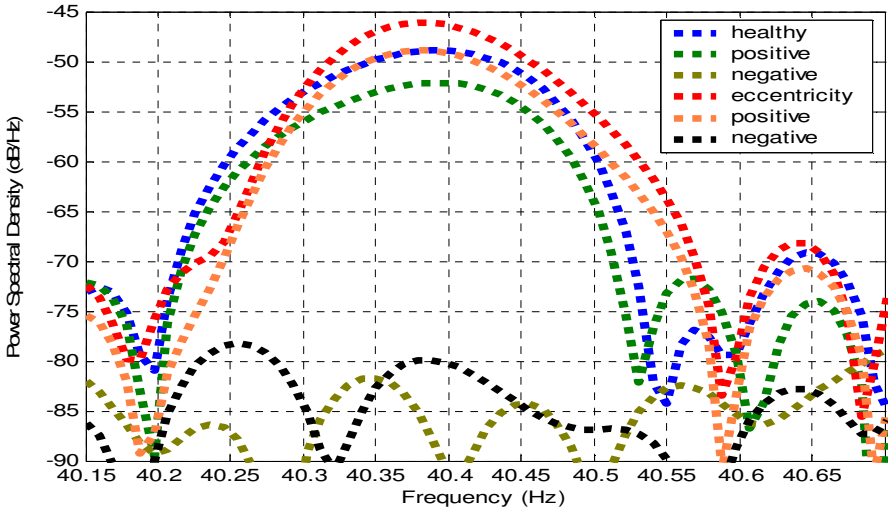

(a) Lower sidebands of *fs±fr*

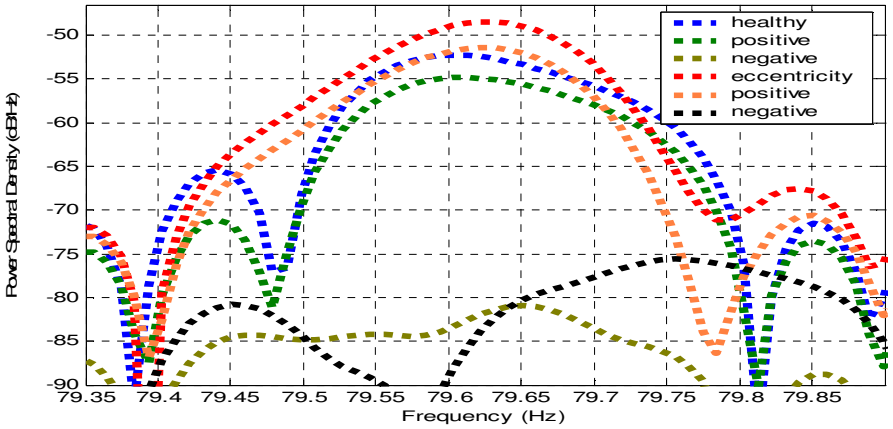

(b) Upper sidebands of *fs±fr*

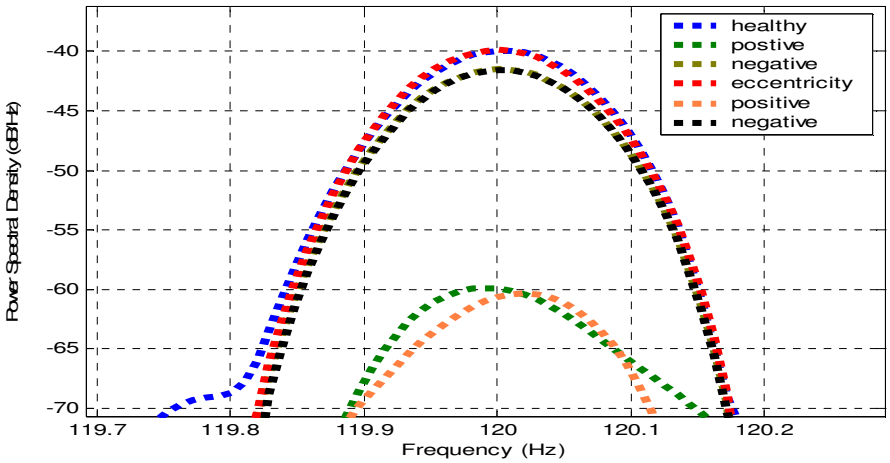

(c) Upper sidebands of *fs±3fr*

Figure 5.26: Negative and positive components for healthy vs. eccentricity with programmable supply at 60 Hz and full load motor

In comparison to above cases, the dynamic eccentricity negative sequence component shows a slight increase from the base, healthy negative sequence component, as shown in Figure 5.27, for the third upper sidebands *fs+3fr*, when drive is controlling the motor. Nevertheless, none of the positive or the negative sequence components show consistent information or better indication of a fault than what that the main phase current can provide. This is true for all of the three supply sources.

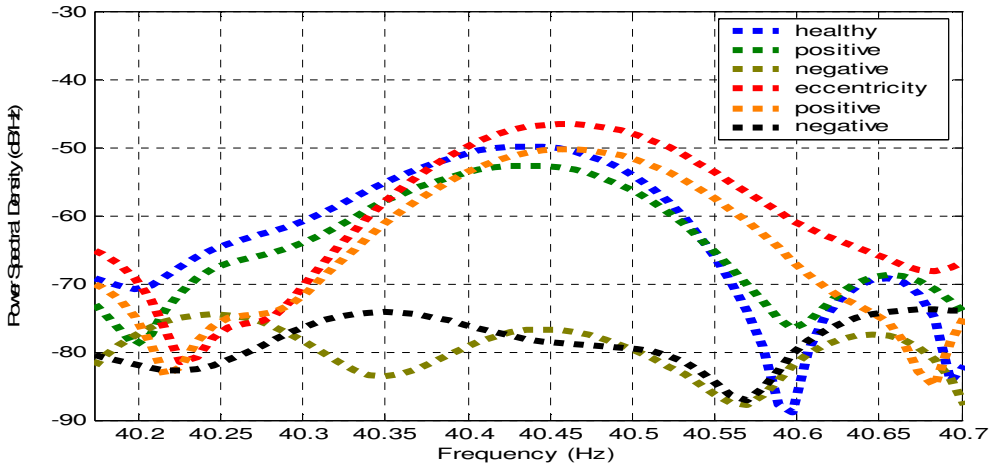

(a) Lower sidebands of *fs±fr*

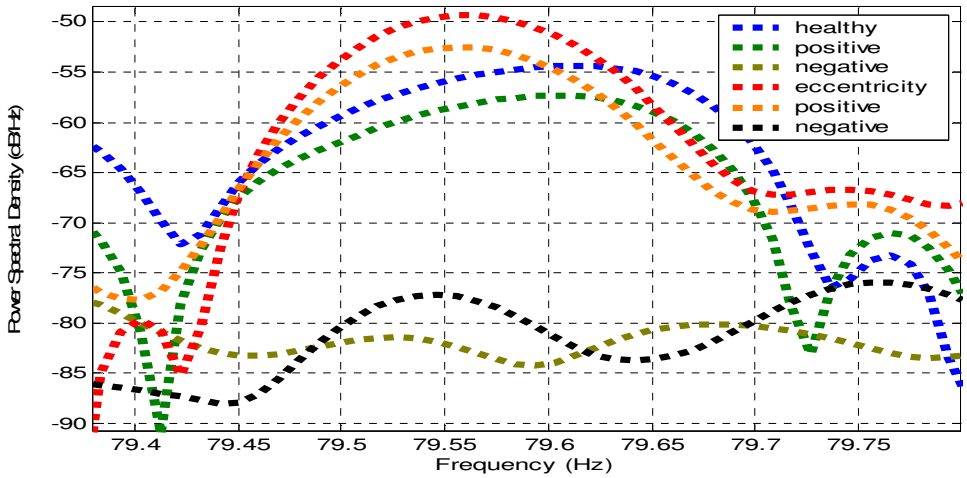

(b) Upper sidebands of *fs*±*fr*

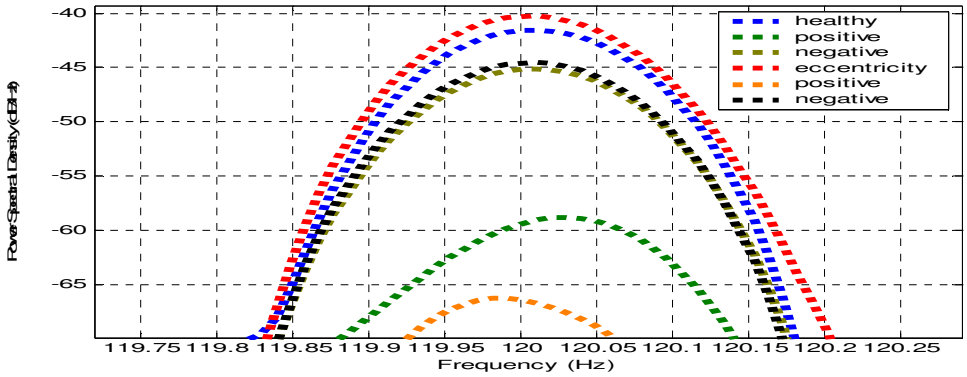

(c) Upper sidebands of *fs*±3*fr*

Figure 5.27: Negative and positive components for healthy vs. eccentricity with drive supply at 60 Hz and full load motor

5.2.2.4 Park's vectors approach

The third way of analyzing the current signature for eccentricity faults is depicted in Figure 5.28 as described in Chapter 3. It is obvious from this figure that none of the different supplies, drive, programmable or mains, provide a better indication of the level of eccentricity fault, since the healthy and the eccentricity figures are almost identical. The only difference that this approach can provide is the reflection of the voltage source supply. For example, the programmable source shows a good circle shape for the pure sinusoidal voltage supply it provides. On the other hand, the drive and the mains supply cases show a hexagonal patterns because of the degree of unbalance that comes with these supplies in addition to the harmonics that the drive injects because of the high switching speed of the IGBT's .

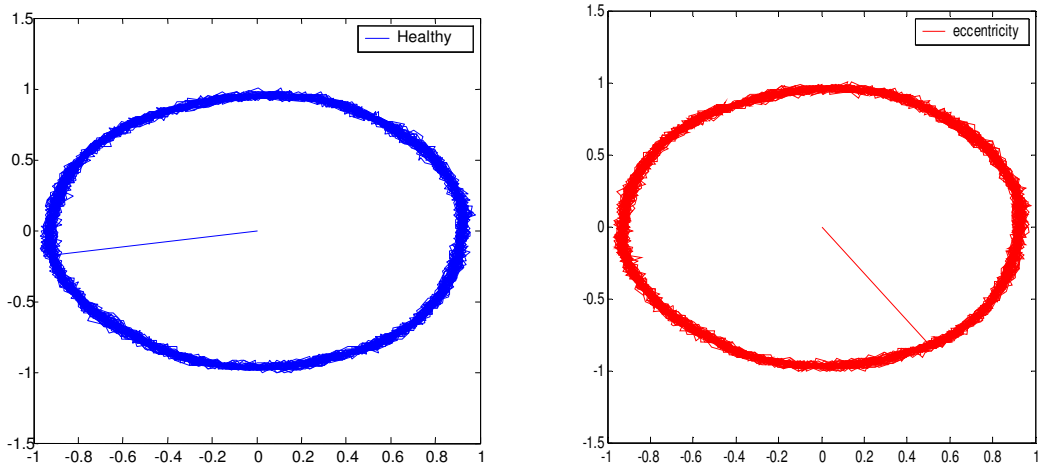

(a) Programmable supply

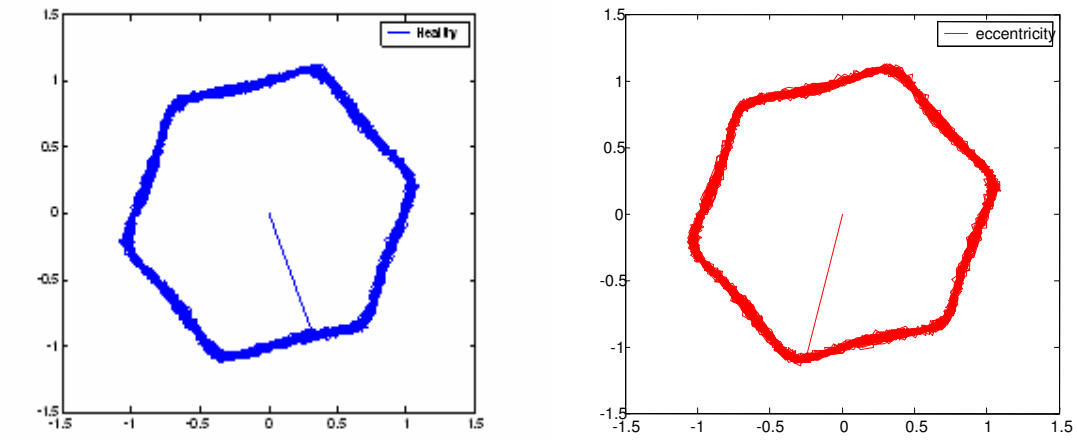

(b) Mains supply

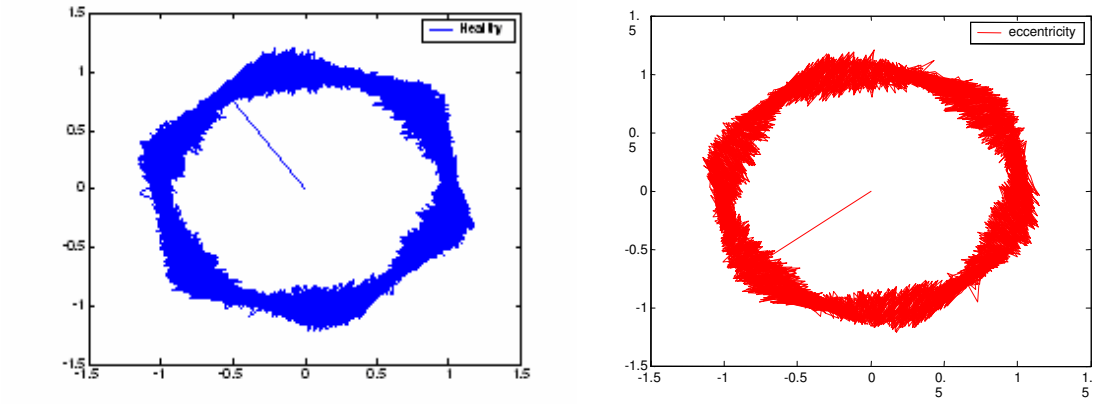

(c) Drive supply

Figure 5.28: Park's vector approach for eccentricity fault at 60 Hz and full load.

6. Bearing Faults

6.1 Analytical background

The majority of the electrical machines use ball or rolling element bearings. Each of these bearings consists of two rings, one inner and the other outer. A set of balls or rolling elements placed in raceways rotate inside these rings. Even under normal operating conditions, with balanced load and good alignment, fatigue failures may take place. These faults may lead to increased vibration and noise levels. Flaking of bearings might occur [21] when fatigue causes small pieces to break and loose from the bearing. Other than the normal internal operating stresses, caused by vibration, inherent eccentricity, and bearing currents [11, 21] due to solid state drives, bearings can be spoiled by many other external causes such as contamination and corrosion caused by sanding action of hard and abrasive minute particles; the corrosive action of water, acid, or other liquids; improper lubrication, which includes both over and under lubrication causing heating and abrasion; and improper installation of the bearing. By improperly forcing the bearing onto the shaft or in the housing (due to misalignment) indentations are formed in the raceways (brinelling) [1, 4, 22].

Although almost 40-50% of all motor failures are bearing-related [1, 2, 4, 17, 21, 22, 23] very little has been reported in literature regarding bearing-related fault detection especially when the motor is fed from other than the mains supply, such as the adjustable speed drive. Bearing faults might manifest themselves as rotor asymmetry faults [2, 17], which are usually covered under the category of eccentricity-related faults. Otherwise, the ball bearing-related defects can be categorized as [2, 17] outer bearing race defect, inner bearing race defect, ball defect and train defect. The vibration characteristic frequencies to detect these faults are given by,

$$f_v = \frac{N}{2} f_r \left[1 - \frac{b_d \cos\beta}{p_d} \right] \tag{6.1}$$

for an outer bearing race defect

$$f_v = \frac{N}{2} f_r \left[1 + \frac{b_d \cos \beta}{p_d} \right] \tag{6.2}$$

for an inner bearing race defect

$$f_v = \frac{p_d}{2b_d} f_r \left[1 - \left(\frac{b_d \cos \beta}{p_d} \right)^2 \right] \tag{6.3}$$

for a ball defect, and

$$f_v = \frac{1}{2} f_r \left[1 - \frac{b_d \cos \beta}{p_d} \right] \tag{6.4}$$

for a train defect

where f_v is the rotational frequency in rpm, N is the number of balls, b_d and p_d are the ball diameter and ball pitch diameter respectively, and β is the contact angle of the ball with the races, as shown in Figure 6.1.

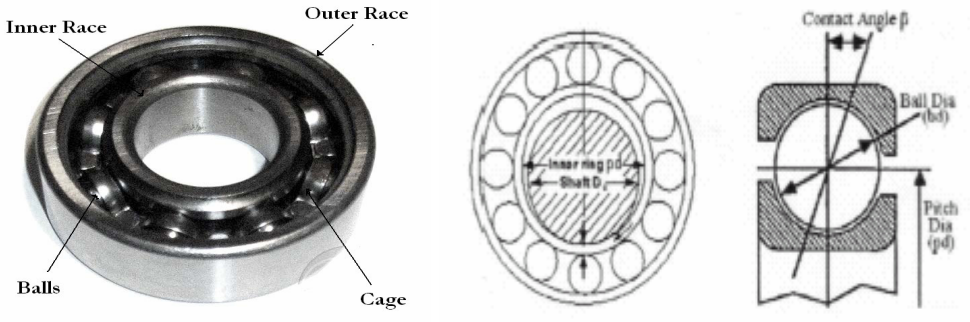

Figure 6.1: Ball bearing internal parts and dimensions [24]

These characteristic frequencies for the inner race and outer race can be approximated [8] for most bearings with between six and twelve rolling-elements by:

$$f_o = 0.4 f_r \bullet n ; \qquad f_i = 0.6 f_r \bullet n ; \tag{6.5}$$

Where f_o is the vibration frequency associated with the outer race and f_i is the vibration frequency associated with inner race fault and f_r is the rotor speed in rps.

The relationship of the bearing vibration to the stator current signature can be determined by recalling that any air gap eccentricity produces anomalies in the air gap flux density. Since ball bearings support the rotor, any bearing defect will produce a radial motion between the rotor and stator of the machine. The mechanical displacement resulting from damaged bearings causes the machine air gap to vary in a manner that can be described by a combination of rotating eccentricities moving in both directions. As with the air gap eccentricity, these variations generate stator currents at frequencies given by [12]:

$$f_{bng} = f_e \pm m f_v \tag{6.6}$$

where m = 1, 2, 3 and f_v is one of the characteristic vibration frequencies.

6.2 Experimental analysis

In this research only the bearing outer race fault is tested. A hole of 4 mm in diameter was drilled in the outer race of the bearing, as depicted in Figure 6.1. The drilling was carefully made in order not to damage the other bearing parts such as the balls and the inner race, so as to avoid multiple bearing fault signals that might provide confusion during the current and vibration analysis.

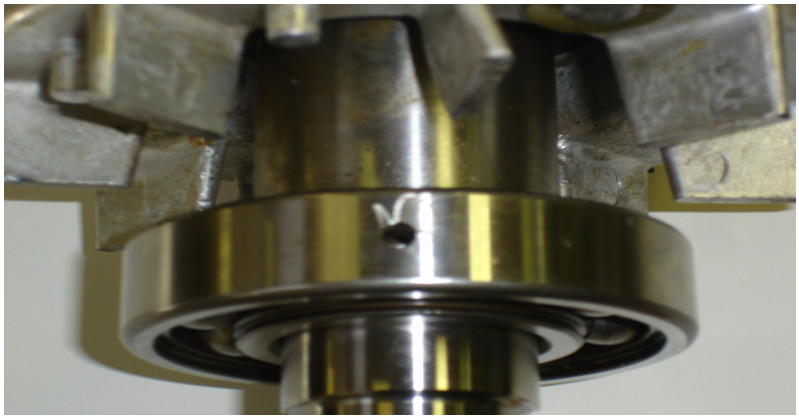

Figure 6.2: Outer race bearing fault

Using equations 6.5 and 6.6, the associated outer race characteristics vibration and current spectrum frequencies are shown in the following tables for the first two values for m (i.e., m=1, 2). Table 6.1 shows the outer race bearing fault frequencies for the situation of the motor being controlled by the drive at different frequencies and running at the motor's full rated load.

fe	*S rpm*	*R rpm*	*fr*	*fo*	*fe+1fo*	*fe-1fo*	*fe+2fo*	*fe-2fo*
30	600	532.50	8.88	28.40	58.40	1.60	86.80	-26.80
40	800	752.90	12.55	40.15	80.15	-0.15	120.31	-40.31
60	1200	1170.8	19.51	62.44	122.44	-2.44	184.89	-64.89
80	1600	1537.9	25.63	82.02	162.02	-2.02	244.04	-84.04

Table 6.1: Outer race bearing fault frequencies with drive supply at different frequency

where *S rpm* is the stator or synchronous speed and *R rpm* is the rotor or mechanical speed. Table 6.2 shows the outer race bearing fault frequencies for the situation of the motor is being supplied from programmable source at different frequencies and running at full load.

fe	*S rpm*	*R rpm*	*fr*	*fo*	*fe+1fo*	*fe-1fo*	*fe+2fo*	*fe-2fo*
30	600	586.50	9.78	31.28	61.28	-1.28	92.56	-32.56
40	800	783.50	13.06	41.79	81.79	-1.79	123.57	-43.57
60	1200	1170.6	19.51	62.43	122.43	-2.43	184.86	-64.86
80	1600	1554.2	25.90	82.89	162.89	-2.89	245.78	-85.78

Table 6.2: Outer race bearing fault frequencies with programmable supply at different frequency

Table 6.3 shows the outer race bearing fault frequencies for the situation of the motor is being fed directly from the mains at 60 Hz and running at full load.

fe	*S rpm*	*R rpm*	*fr*	*fo*	*fe+1fo*	*fe-1fo*	*fe+2fo*	*fe-2fo*
60	1200	1170.8	19.50	62.40	122.40	-2.40	184.80	-64.80

Table 6.3: Outer race bearing fault frequencies with mains supply

6.2.1 Vibration monitoring test

Vibrational test analysis is an effective tool to determine the level of bearing faults on a machine by measuring the level of vibration of the machine casing. To determine the outer race faults, an accelerometer vibration analyzer is used to measure the vibration characteristic frequencies at a horizontal position to the motor housing. The first vibration characteristic frequency shown from the vibration test is at f_o = 61.56 Hz which is very close to the one predicted by Table 6.2 at f_o = 62.44 for the situation of the motor is being supplied through a programmable source. Moreover, because of the incipient bearing fault that this motor has, the newest and most dominant characteristic vibration frequencies are in the high frequency range, as shown in Figure 6.3(b). They

came as the 21st, 22nd, 23rd, 24th, 25th and 26th multiples of the f_o vibration frequency. The highest frequency among them is the 24th multiple of f_o at 1444.7 Hz. However, these frequencies are not present for the healthy case, as shown in figure 6.3 (a).

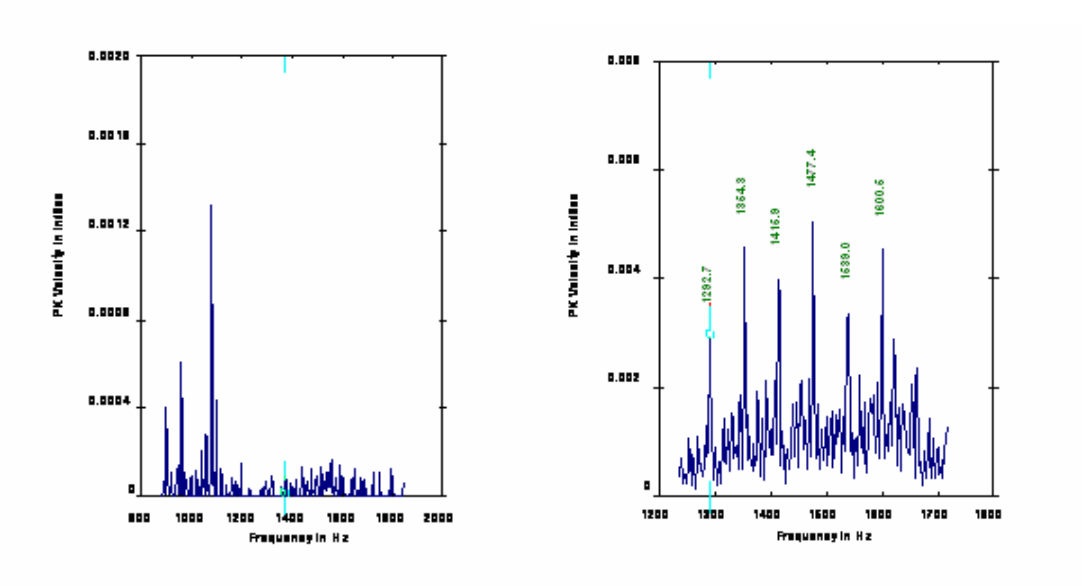

(a) Healthy motor (b) Bearing fault

Figure 6.3: Vibration test for bearing faults vs. healthy with programmable supply at 60 Hz and full load

The overall vibration frequency at 60 Hz from a mains supply to the motor at no load is 0.037 in/sec. This level of vibration decreases as load increases – down to a level of 0.032 in/sec at the rated full load- as shown in figure 6.4.

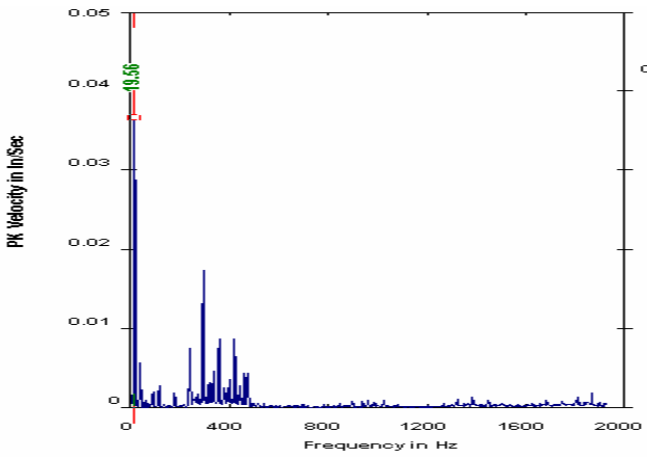

Figure 6.4: Vibration test at full load and 60 Hz from mains supply

For the programmable source, different frequencies have been tested at different load levels. Figure 6.5 shows the full load level vibration test at different frequencies. Although the overall vibration level increases from 0.009 in/sec at 30 Hz up to 0.044 in/sec at 80 Hz, it becomes difficult to relate the new frequencies to the ones expected by Table 6.2. This confirms that the vibration signal analyzer is limited in its of detection of bearing faults at low frequencies despite the clean source that the motor is using as its power supply.

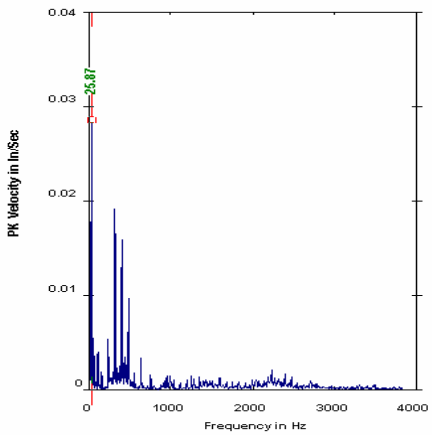

(a) 80 Hz

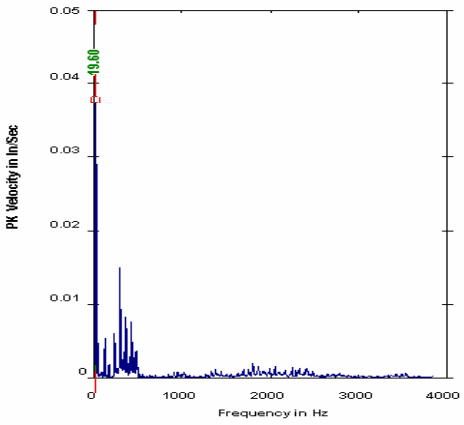

(b) 60 Hz

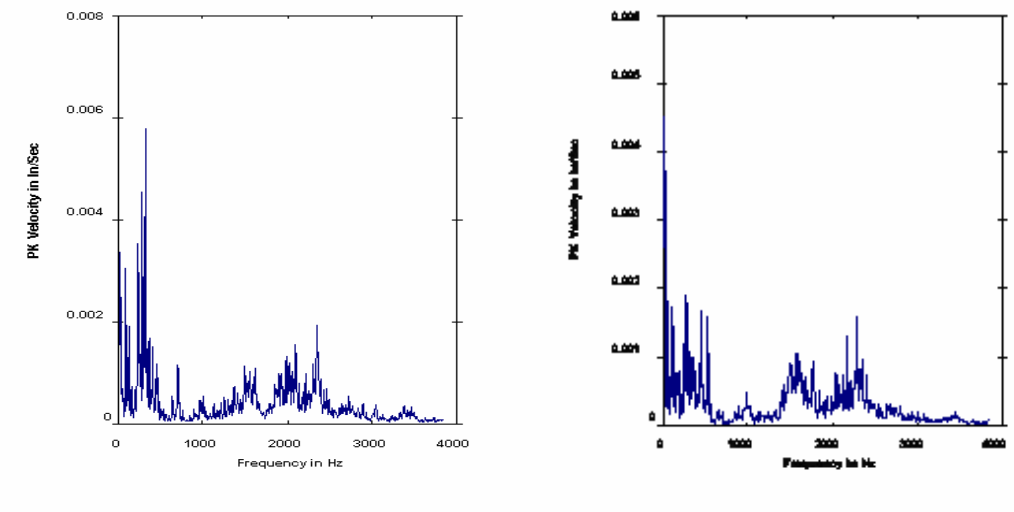

(c) 40 Hz (d) 30 Hz

Figure 6.5: Vibration test at full load and a programmable source supply at different frequencies

More vibration characteristic frequencies start to show as the frequency changes from the motor rated- frequency using the drive source, as shown in Figure 6.6. Although the 30 Hz and 40 Hz tests show some high frequency peaks, however, their overall value is minimal and not related to the characteristic frequency for bearing faults. On the other hand, the 60 Hz and 80 Hz tests show a measurable overall vibration frequency in the range of 0.035 in/sec and 0.049 in/sec for the 60Hz and 80 Hz test, respectively. Moreover, their characteristic frequency in the high range comes as a multiple of the expected values by Table 6.3.

This leads to the conclusion that using vibration signal for bearing faults detection is not only costly but is unreliable in the low frequency range. Motors controlled by drives for energy saving purposes usually operate in this low frequency range.

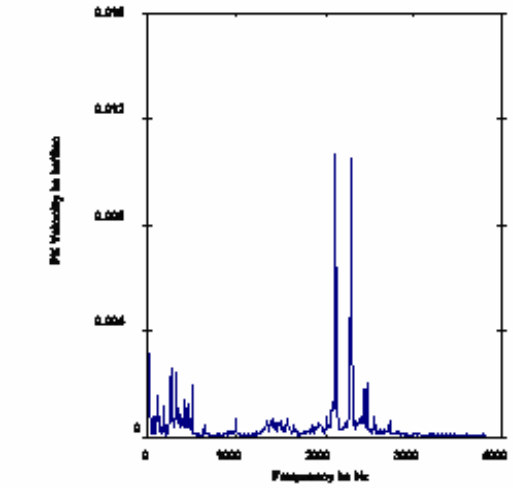

(a) 30 Hz

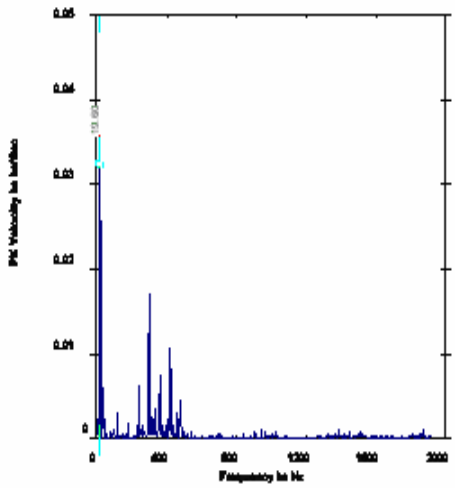

(b) 40 Hz

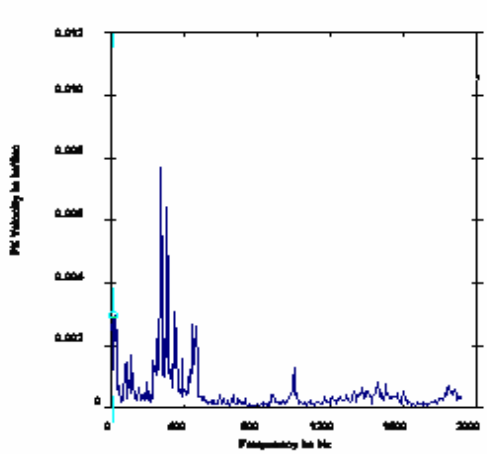

(c) 60 Hz

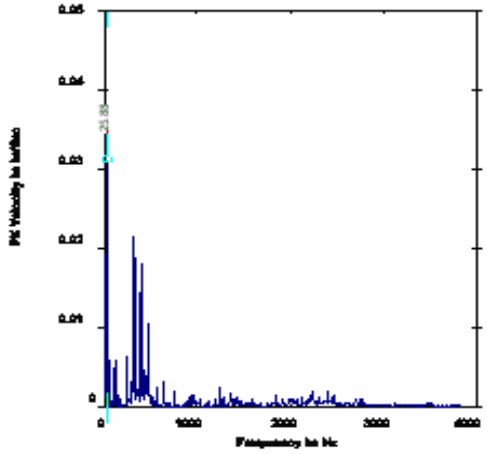

(d) 80 Hz

Figure 6.6: Vibration test at full load and a drive source supply at different frequencies

6.2.2 Current signature analysis

For bearing faults detection, the current signature measures the air gap displacement movement or the relative motion between the stator and rotor that is reflected to the stator current, as opposed to vibration monitoring, which measures absolute motions. The three different ways of analyzing the current signature for fault detection, as described in Chapter 3, are analyzed for the bearing faults detection in the following sections:

6.2.2.1 Power spectral density analysis

The analysis of the power spectral density has shown a detectable fault frequency that starts to appear only at the higher frequency range, due to the small bearing fault created in this test. Moreover, the bearing current frequency faults shown in above tables are either not practical for the frequency spectrum like the *fe-1fo* and *fe-2fo* because their values are negative or because they are very close to non-faulty harmonics like *fe+1fo* (close to the fundamental second harmonics) or like *fe+2fo* (close to the fundamental third harmonic), which makes it difficult to determine the fault condition from them. This is because of the high energy that those close harmonics possess which dampens the bearing faults' frequency energy. Therefore, the following analysis concentrates on any new frequency that appears only within the bearing fault spectrum rather than in the healthy spectrum, or on a notable increase to an existing frequency that is believed to be due to the bearing fault.

Figure 6.7 depicts the bearing fault spectrum versus the healthy case where the motor is fed from the mains supply. The only new frequencies that appeared at the bearing fault are at 522 Hz, 882Hz, and 900Hz. Moreover, a notable high increase in the magnitude of the 162 Hz and 180 Hz (*fe+2fo)* harmonics was observed. The significantly high magnitude of a frequency at 4243 Hz is due to the outer race bearing faults. A similar frequency also appears close to 4243 Hz in the healthy case due to the level of voltage unbalance, as will be shown in Figure 6.9.

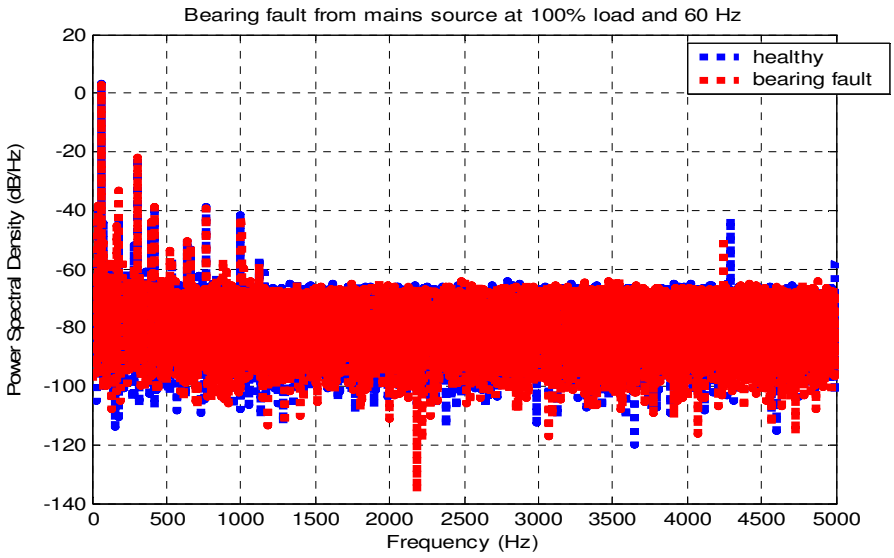

(a) Overall spectrum

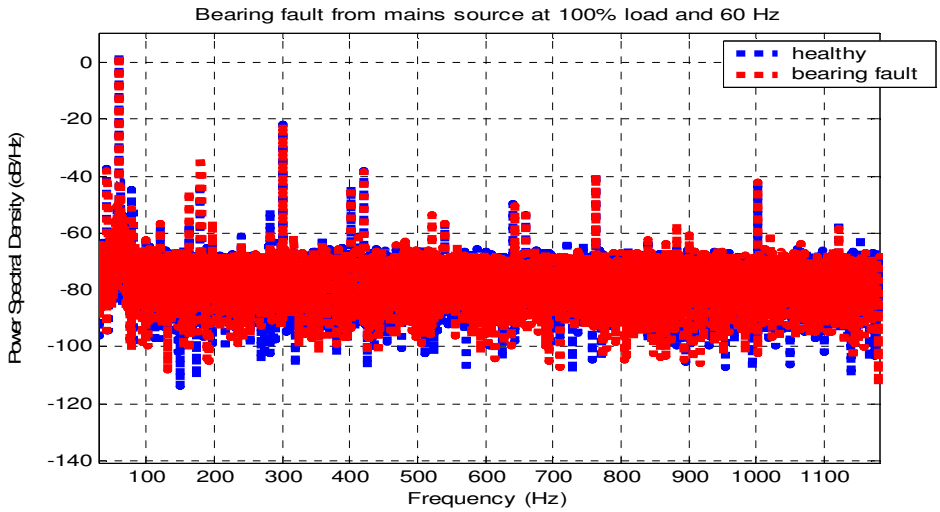

(b) Low frequency range

Figure 6.7: PSD for bearing fault from mains vs. healthy case

The position of the high frequency harmonics in the range of 4240 Hz at a different loading level for the same test is shown in Figure 6.8. There is no clear trend for the position of the bearing fault frequency in respect to the load level. This proves and validates the above bearing faults equations that are not slip dependent.

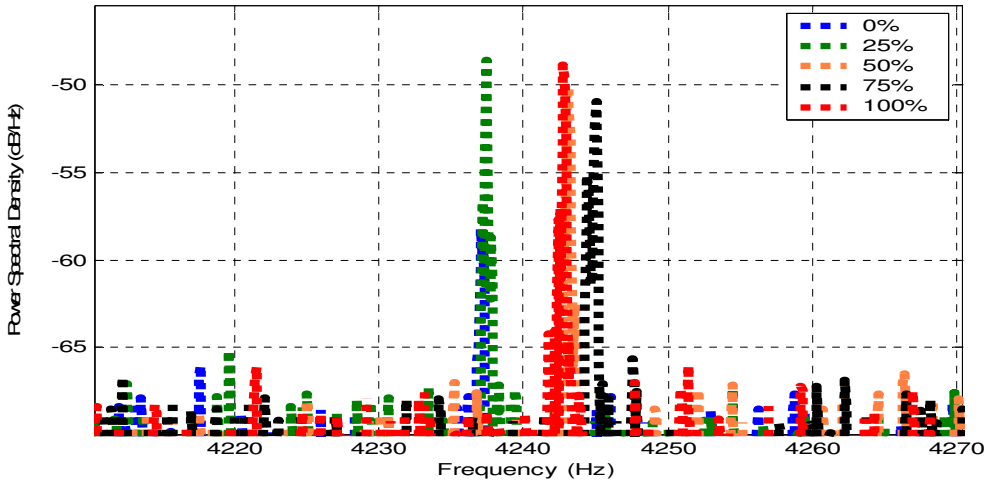

Figure 6.8: High frequency positions at different t loading levels for the 60 Hz test and motor is supplied from the mains

In the case where the programmable source is feeding the motor, only the high frequency at 4200 Hz appears as a difference in healthy motor, as depicted by Figure 6.9, for the rated operating frequency at 60 Hz and the rated full load. The disappearance of a healthy frequency close to 4200 Hz proves that the case shown in Figure 6.7 is mainly due to voltage unbalance.

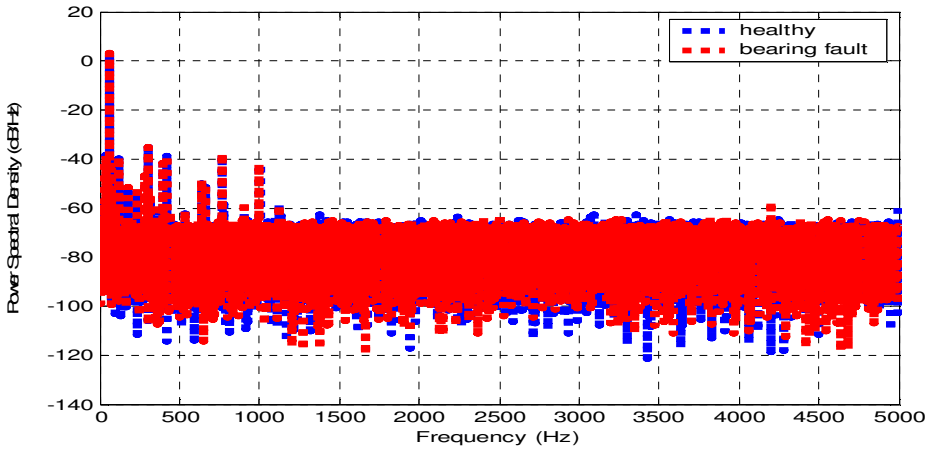

(a) Overall spectrum

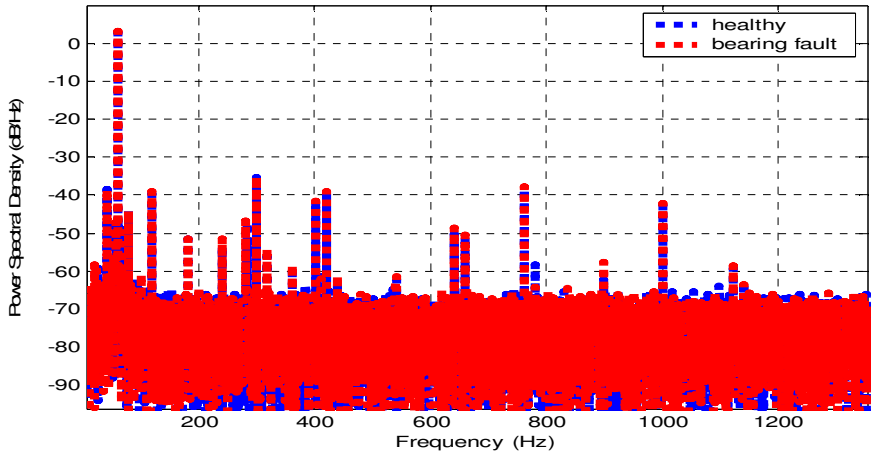

(b) Low frequency range

Figure 6.9: PSD for bearing fault with programmable source at 60 Hz and full load

In terms of load level dependency, the different load level for the same test is shown in Figure 6.10. The position of the new frequency for the bearing fault detection does not show a pattern is revealed when changing the load or speed.

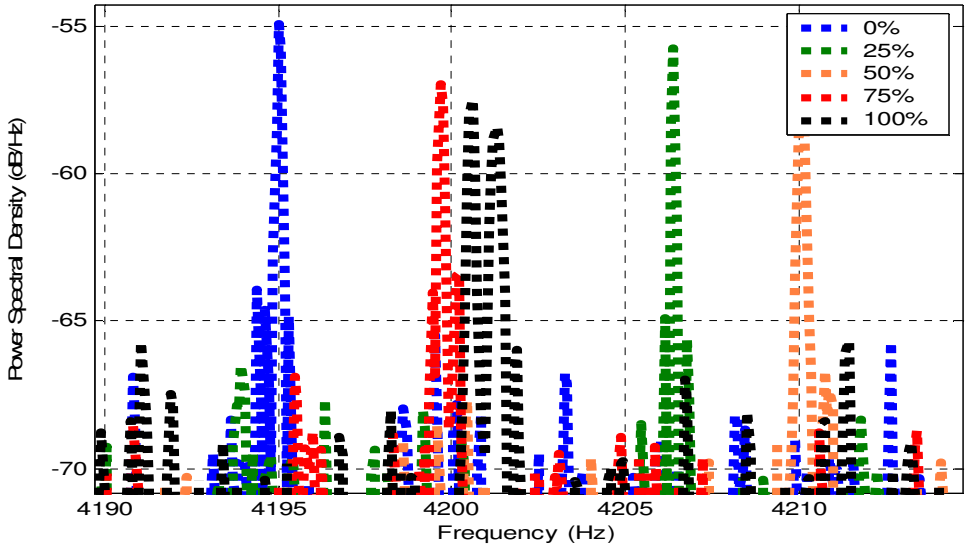

Figure 6.10: Positions of high frequency bearing fault at 60 Hz and at different loading levels with supply from the programmable source

Different frequencies have been tested in order to see the influence of changing the frequency to the bearing fault frequency spectrum. The following figures depict the

different frequencies test for the bearing high frequency position. For the 30 Hz test at full load, as shown in Figure 6.11, an increase in the magnitude of 40 Hz and 20 Hz (eccentricity sidebands) frequencies is observed. The fundamental third harmonic at 90 Hz (*fe+2fo*) shows a notably high magnitude for the healthy case. A new frequency that is to believed to be caused only by the bearing fault is at 4234 Hz.

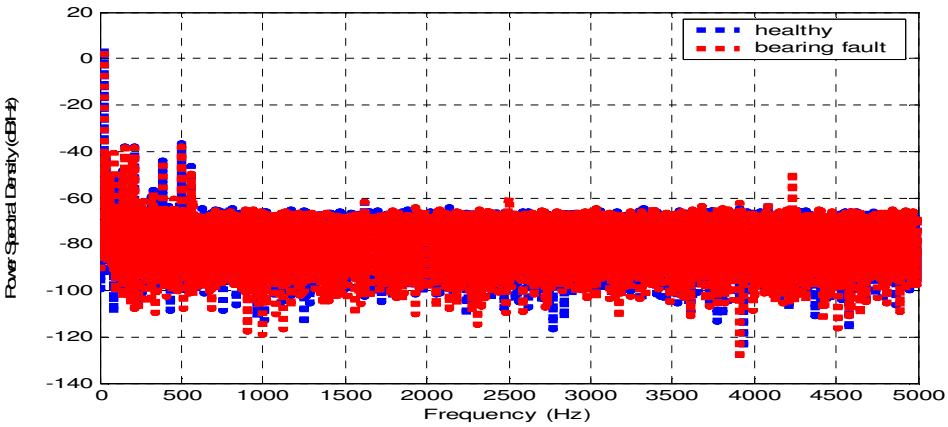

(a) Overall spectrum

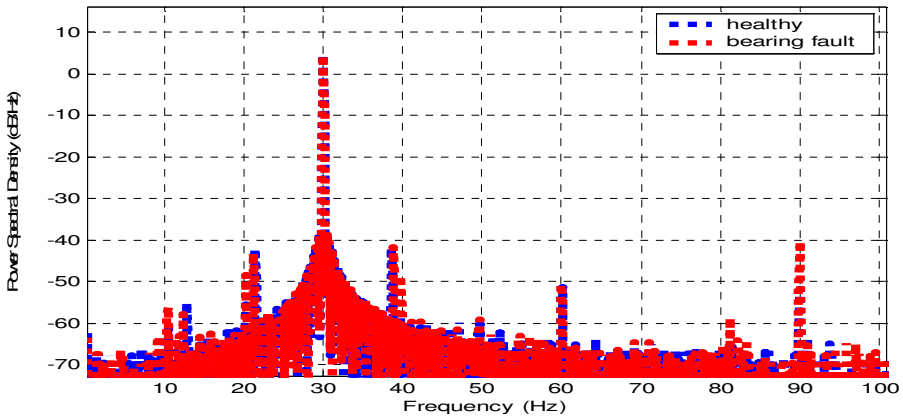

(b) Low frequency range

Figure 6.11: 30 Hz test from programmable source at full load

The different load levels test show that the bearing fault frequency has non-uniform peaks, as depicted in Figure 6.12. The bearing fault frequency is evident at all

loads and at low frequency, as opposed to the broken rotor bar and dynamic eccentricity, which are load dependent faults.

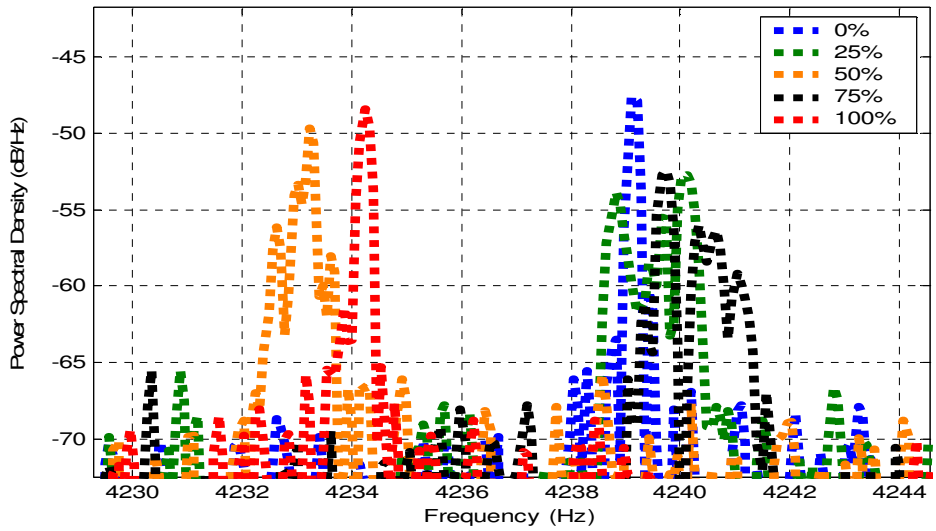

Figure 6.12: Different loads for the bearing fault at 30 Hz and full load

For a high frequency operation like 80 Hz, the bearing fault's new frequency is at 1167 Hz for the motor rated full load case, as shown Figure 6.13. The high frequency speed has no obvious impact on the detection of a faulted bearing, as opposed to the broken rotor bar and dynamic eccentricity faults which show a high magnitude in the fault sidebands at high frequency.

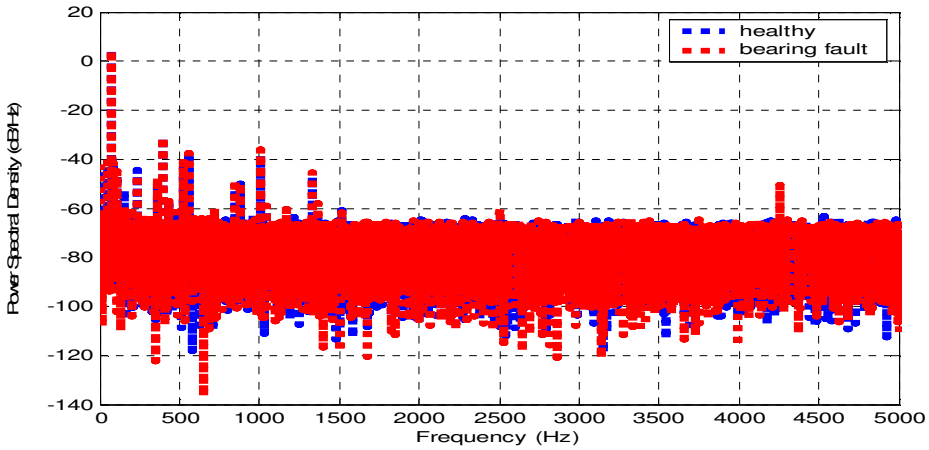

(a) Overall spectrum

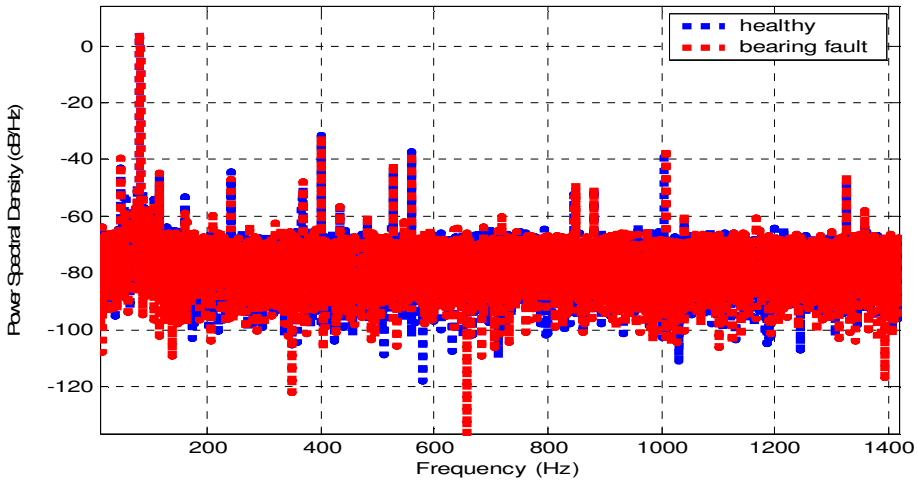

(b) Low frequency range

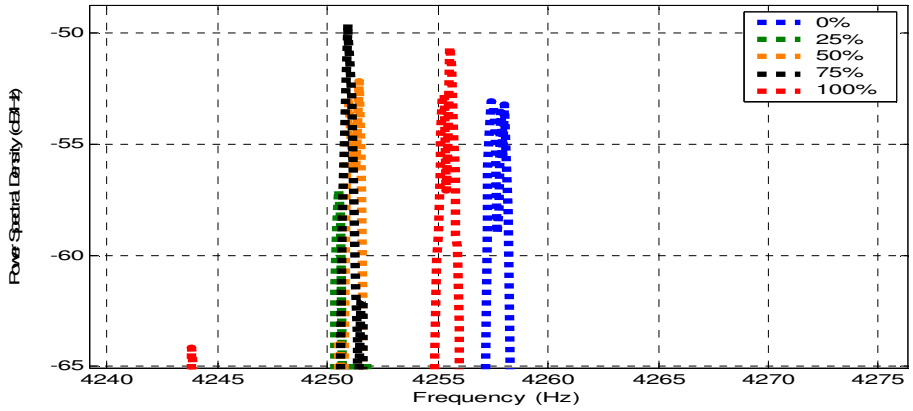

(c) Different load for the bearing fault at 80 Hz and full load

Figure 6.13: 80 Hz test from programmable source at full load

In the case that the drive is controlling the motor, more frequency harmonics start to appear because of the non-sinusoidal voltage supply that the drive is injecting, which reflect back to the frequency spectrum of the current. This is shown in Figure 6.14 for the case that motor is running at the rated full load at 60 Hz. A focus on the lower frequency band for the healthy and bearing faults cases is depicted on part "b" of the same figure. The new frequency that is believed to be a reflection of the bearing fault is at 4269 Hz. A Similar frequency but with less magnitude appears for the healthy case at 4266 Hz, mainly due to the non-sinusoidal supply as described above

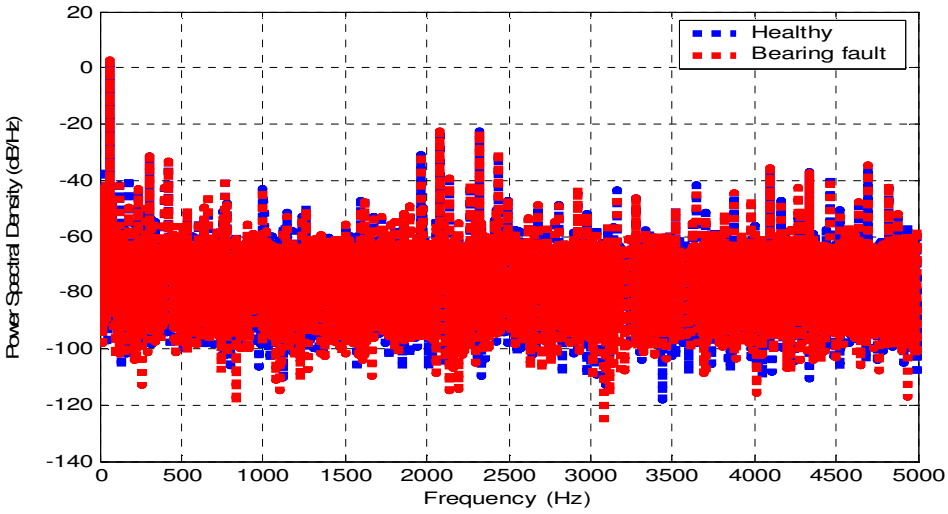

(a) Overall spectrum

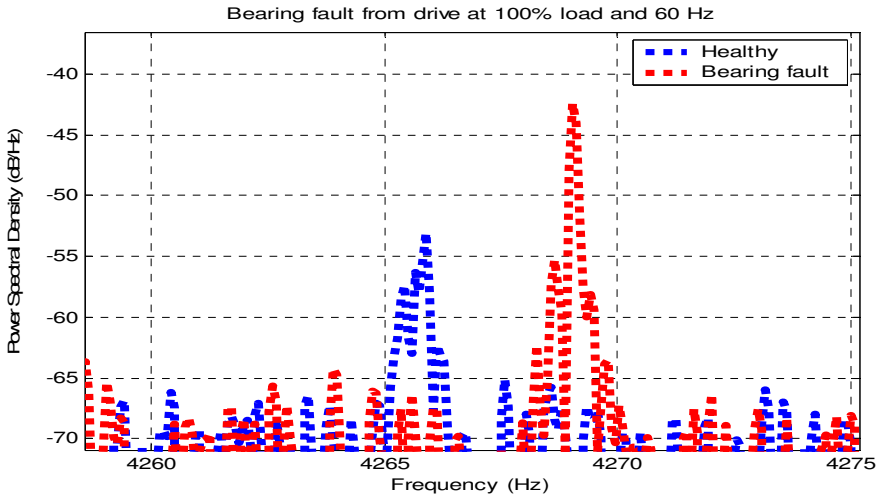

(b) High frequency range

Figure 6.14: Drive as source and motor with full load and 60 Hz

At different load the bearing fault frequency positions have a wider gap between each other. The magnitude of these frequencies increases as the load increases. However, a pattern in how these frequencies appear with respect to the load is hard to uncover, as shown in Figure 6.15.

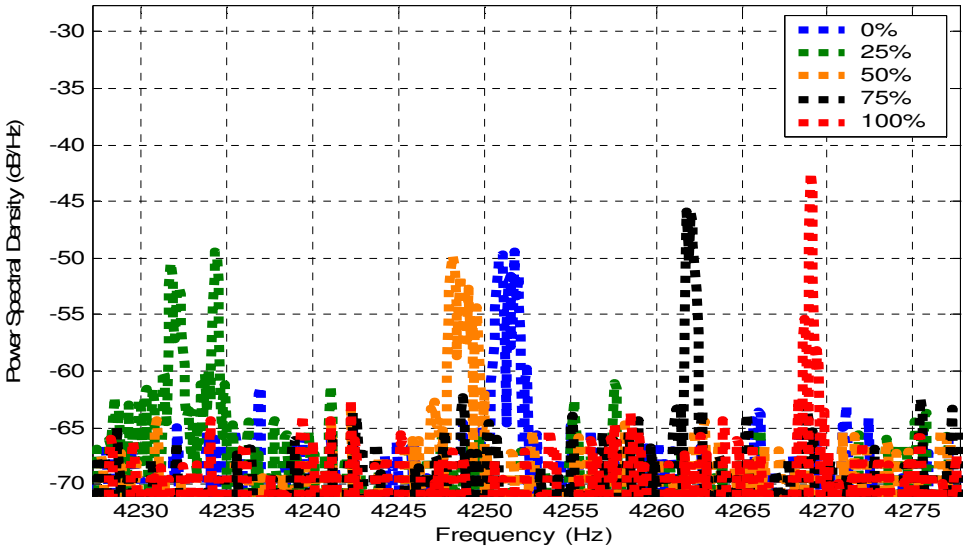

Figure 6.15: Different loading levels for the bearing fault frequency position and motor is running at 60 Hz

Tests at several frequencies and different loads were conducted in order to study the influence of changing the frequency in detection of the bearing fault. Figure 6.16 depicts the 30 Hz position of the high frequency showing a significant increase due to the bearing fault. Part "b" depicts the same figure at different loads.

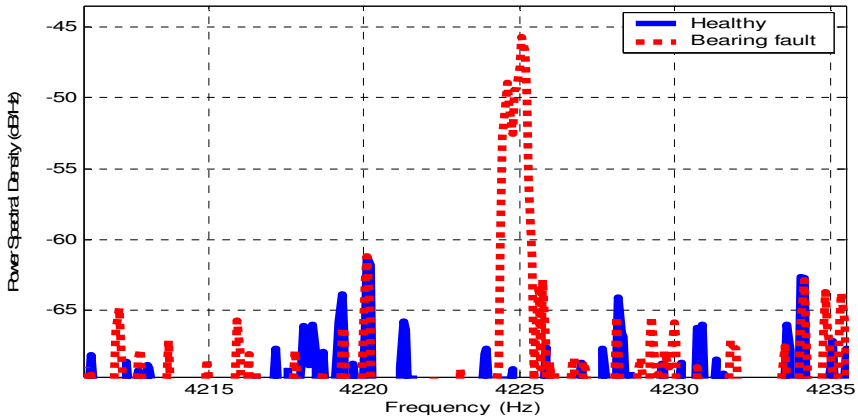

(a) High frequency range

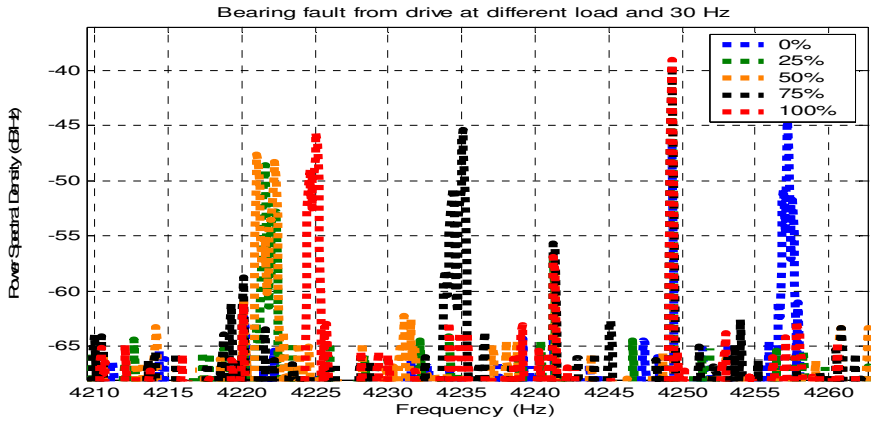

(b) Positions of the bearing fault frequency at different load level at 30 Hz

Figure 6.16: Drive as source at 30 Hz test with motor at rated load

Figure 6.17 depicts the 80 Hz test. The new frequency that indicates a bearing fault is at 4233 Hz. This increase of frequency has further increased the non uniform peaks of the bearing fault frequency, as shown in part "b" of the same figure. However, since at this high level of frequency the drive starts to inject more harmonics, it is hard to tell if this effect is only due to the bearing fault. Moreover, it is believed that the drive starts to operate in the overmodulation range at a frequency higher than 60 Hz, which increases the number of harmonics in the high frequency range.

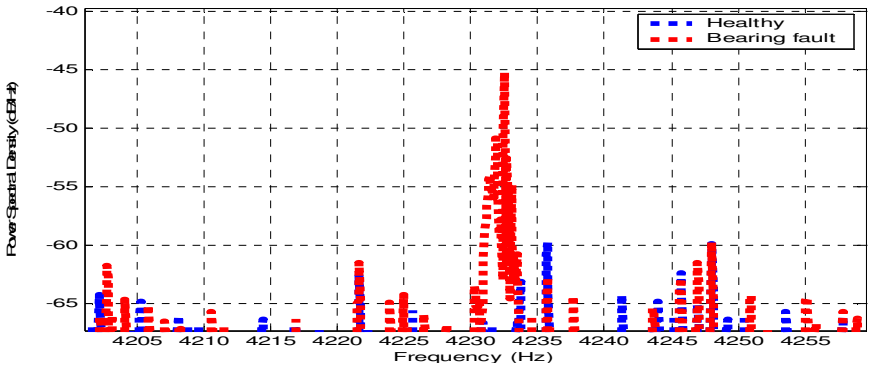

(a) High frequency range

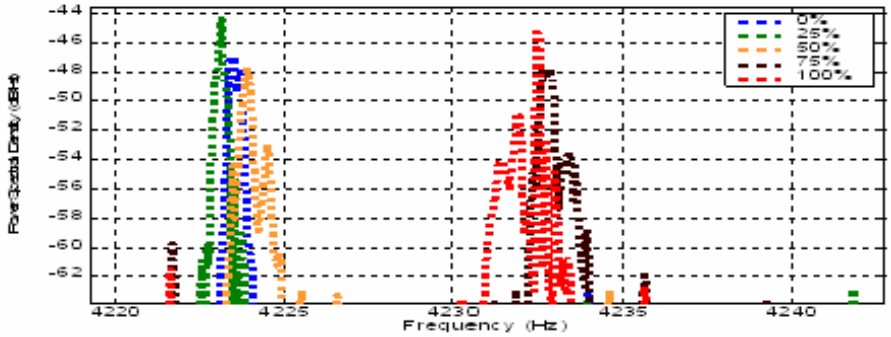

(b) Positions of the bearing fault frequency at different load level.
Figure 6.17: Drive as source at 80 Hz test with motor at full load

In summary, due to the incipient bearing fault made in this research, the frequencies that can reflect this fault in the current spectrum are seen only in the high frequency range for all of the tested supply sources, as shown in Tables 6.4. This makes it hard to relate these frequencies to any one of those expected by the bearing faults equations described earlier. Moreover, because the drive switching frequencies are usually in the high frequency range, it is impossible to find the subject frequencies unless a supply from a different source, like the mains or programmable source, is compared with in order to help predicate the range in which these frequencies might exist.

On the other hand, the vibration signal analysis was showing a better coloration than the current signature between expected bearing faults characteristic frequencies and the ones predicted by the bearing faults equations.

Load	30 (Hz)	40 (Hz)	60 (Hz)	80 (Hz)
0	4239	4238.5	4195	4258
25	4239	4240.5	4206	4251
50	4233	4239.5	4210	4251
75	4240	4234.5	4200	4251
100	4234	4236	4201	4255

(a) Programmable supply

Load	30 (Hz)	40 (Hz)	60 (Hz)	80 (Hz)
0	4257	4259	4251	4223
25	4222	4231.5	4233	4223
50	4222	4232	4249	4224
75	4235	4235	4262	4233
100	4225	4236	4269	4232

(b) Drive supply

Load	60 (Hz)
0	4237
25	4237.5
50	4243
75	4245
100	4242.7

(c) Mains supply

Table 6.4: Experimental bearing fault frequencies for current analysis at different frequencies and different loads

6.2.2.2 Negative and positive sequence analysis

The current negative and positive sequence components clarify that the bearing fault frequencies are detected in the high frequency range, as shown in the previous section. Figure 6.18 depicts the negative and positive components for the healthy and bearing fault conditions for the three different power supplies. For the three supplies - mains, programmable and drive - none of the positive and negative components accompanied the bearing faults' main phase current frequency. On the other hand, with the drive and mains power supplies some of the negative components come with a healthy frequency that is believed to occur from voltage unbalance. This finding, however, does not provide any useful information or provide a good indicator for the detection of bearing faults, but it does provide a clear sign that negative and positive sequence components are more related to non-faults conditions like supply voltage unbalance. This is more evident from the programmable source test where the absence of any healthy frequency is marked by the absence of the negative and positive sequence components.

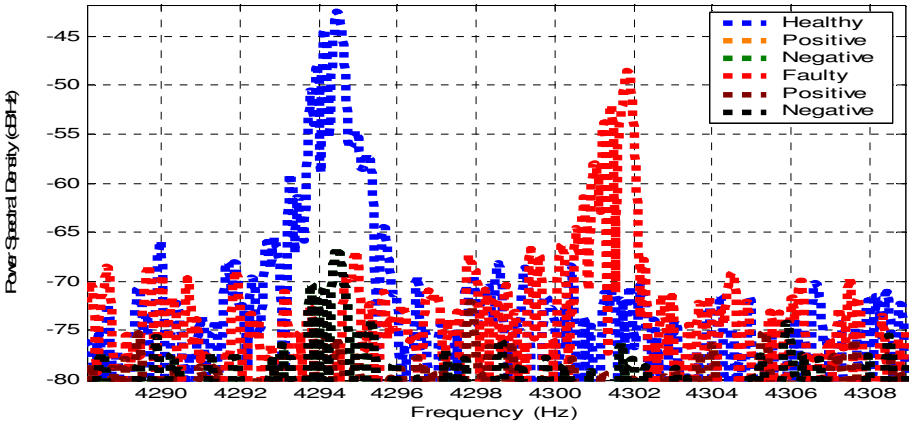

(a) Mains supply and motor running at 60 Hz and full load

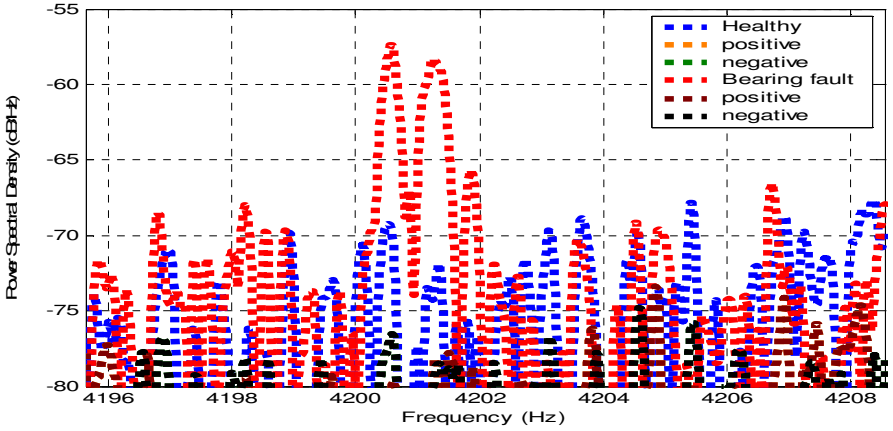

(b) Programmable supply and motor running at 60 Hz and full load

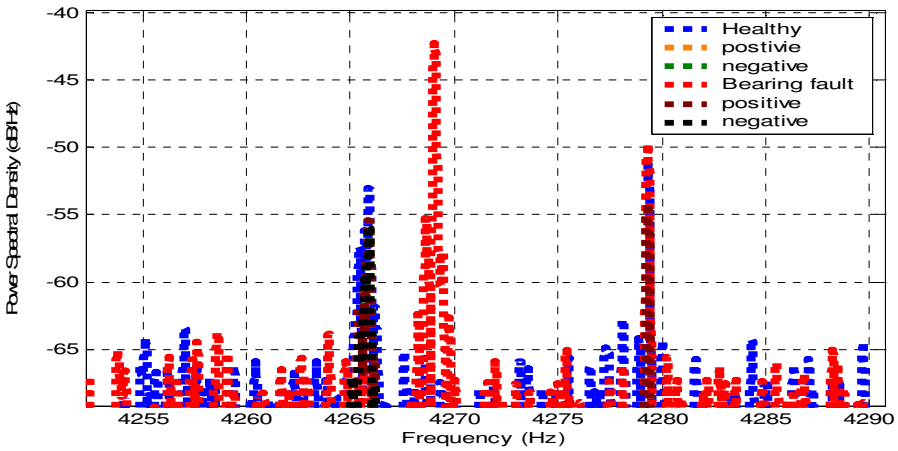

(c) Drive supply and motor running at 60 Hz and full load

Figure 6.18: Negative and positive components for the bearing fault and healthy case at 60 Hz and full load.

6.2.2.3 Park's vector approach analysis

Similar to the broken rotor bar and eccentricity tests, Park's vector method has been applied to the bearing fault detection analysis, as discussed in Chapter 3. It is obvious from Figure 6.19 that none of the different source supplies - drive, programmable or mains - provide a better indication of the level of bearing fault where the healthy and the eccentricity figures are almost identical except for the difference in rotation. The only different outcome of this approach is the influence of the voltage source supply, where the programmable source shows a good circle shape due to the pure sinusoidal voltage supply it provides. Meanwhile, the drive and the mains supplies shows a hexagonal shape because of the degree of unbalance that comes with these supplies, in addition to the harmonics that the drive injects because of the high switching speed with witch the switching IGBT's are working. Moreover, the change of rotation is not an indication of fault because it is mainly due to swapping of phases during the experimental setup.

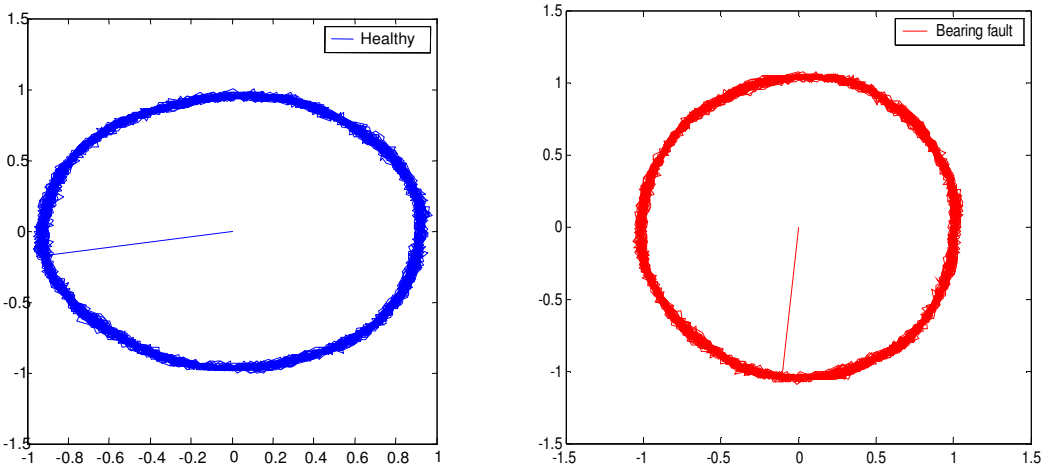

(a) Programmable supply

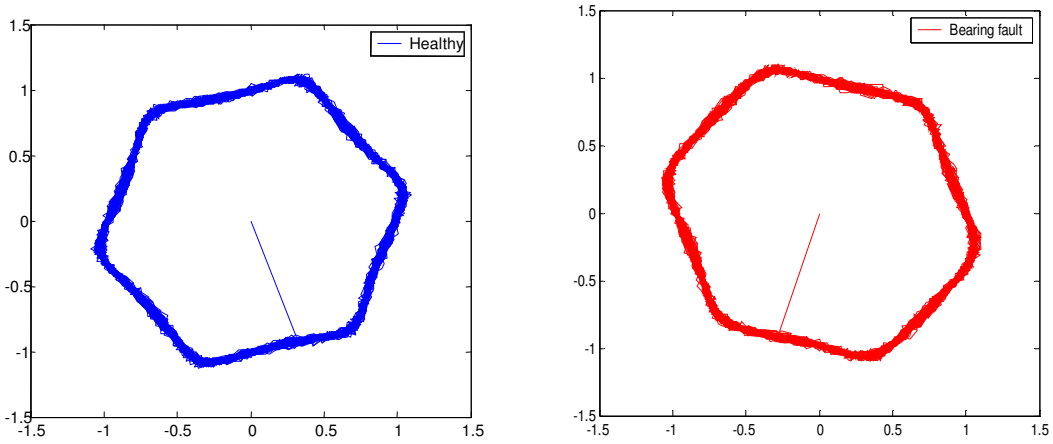

(b) Mains supply

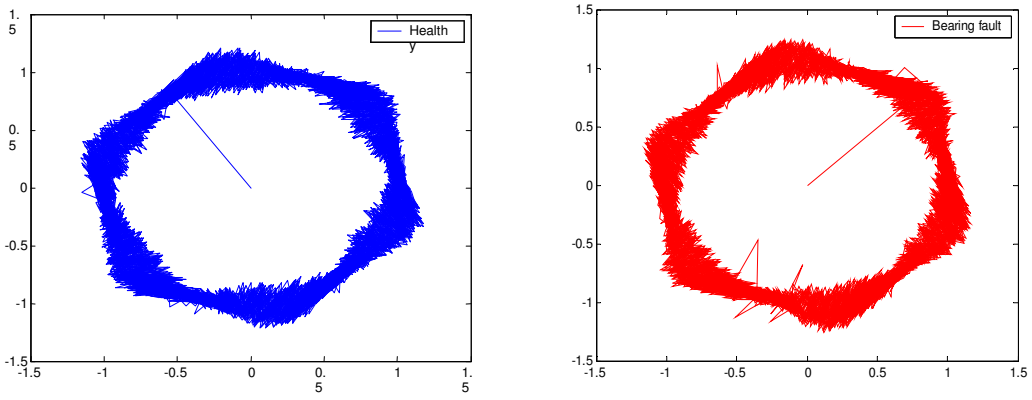

(c) Drive supply

Figure 6.19: Park's vector approach for bearing fault at 60 Hz and full load

7. Conclusions and recommendations for future work

This research has investigated three major induction motor faults. These are the broken rotor bar, air gap dynamic eccentricity, and bearing faults. These faults have been experimentally simulated in the lab, at different levels of severity. Current signature analysis with correlation to the vibration motoring have been used as the prime tools for the detection of these faults. Three main methods of current signature analysis have been analyzed for the three experimentally generated faults. These are the power spectral density estimation using the Welch approach, the positive and negative sequence components, and the three phase Park's vector approach. Using an adjustable speed drive to control a motor, and its influence on these fault detection techniques, has been compared to powering the motor directly from the mains supply and through a pure sinusoidal supply from a programmable source.

This research has proved that using the power spectral analysis is a good tool to detect induction motor faults that use adjustable speed drive control as well as for mains supply. In particular, detection of broken rotor bar faults using the Welch spectral power density estimation has shown a better potential for incipient fault detection than the vibration test. Different broken rotor bar fault severities can be revealed directly from the fundamental first order sidebands, which are not at all present in the healthy case. For the dynamic air gap eccentricity fault, correlation between the vibration test and the current signature using the power spectral density is important for a proper assessment of the motor condition because of the overwhelming harmonics from the other non-faulty symptoms. This is mainly due to the presence of the eccentricity sidebands even in a healthy case. With regards to the bearing fault, the vibration signal has shown better indication of the bearing fault condition than the current signature analysis using the power spectral density. However, it is most likely impossible to pinpoint any of the bearing faults' current signature harmonics in the low frequency range, as a way to provide a bearing fault indication. The positive and negative approach, and the Park's vector approach did not show more effective results for fault detection due to their great influence by non-fault conditions like the supply voltage unbalance and load oscillating conditions.

Future work on this line of research should include using different signal processing spectral estimation methods, such as wavelet analysis which provides a better estimation for non-stationary signals, like the bearing faults for example. Additional research should also test the severity of different bearing faults including different bearing parts like the inner race and ball bearing faults. Analyzing the influences of overall system components on the reliability of the fault detection techniques needs to be further investigated. These include the supply system disturbances like sag, swells and dips, and the effect of coupled load and interruption of this to the drive, such as from the loss of signal from a control valve. Studying the influence of the drive on the stator turns fault detection needs to be included. Considering different brands and different sizes of motors is also important.

References

[1] Benbouzid, M El, "Bibliography on induction motor faults detection and diagnosis," *IEEE Transactions on Energy Conservation*, vol. 14, pp. 1065-1074, 1999.

[2] Nandi, S. and Toliyat, H. A., "Fault diagnosis of electrical machines- a review," *Conference record of the IEEE IEMDC'99, IEEE International Conference on Electric Machines and Drives*, pp. 219-221, 1999.

[3] Kliman, G. B. and Stein, J., "Induction motor fault detection via passive current monitoring," *Record of the International conference in Electrical machines,* pp. 13-17, 1990

[4] Thorsen, O. V. and Dalva, M., "A survey of faults on induction motors in offshore oil industry, petrochemical industry, gas terminals, and oil refineries," *IEEE Transaction on Industrial Electronics*, vol. 31, no. 5, pp. 1186-1196, 1995.

[5] Villada, F., Cadavid, D., Munoz, N., Valencia, D. and Parra, D., "Fault diagnosis in induction motors fed by PWM inverters," *Conference record of the IEEE SDEMPED 4th Meeting, IEEE International Symposium on Diagnostics for Electric Machines, Power Electronics and Drives*, pp. 229 - 234, 2003.

[6] Cash, M. A. and Habetler, T. G., "Insulation failure detection on the stator winding of ASD-driven induction machines using standard deviation of line currents," *Conference Record of the IEEE IAS Annual Meeting,* vol. 1, pp. 299-301, 1998.

[7] Miletic, A. and Cettolo, M. "Frequency converter influence on induction motor rotor faults detection using motor current signature analysis-experimental research," *Conference record of the IEEE SDEMPED 4th Meeting, IEEE International Symposium on Diagnostics for Electric Machines, Power Electronics and Drives,* pp. 124 – 128, 2003.

[8] Bellini, A., Filippetti, F., Franceschini, G., Tassoni, C., "Closed loop control impact on the diagnosis of induction motors faults" *Conference Record of the IEEE Industry Applications Society 35th IAS Annual Meeting*, vol. 3, pp. 1913 - 1921, 1999.

[9] Briz, F., Degner, M.W., Diez, A.B., Guerrero, J.M., "On-line diagnostics in inverter fed induction machines using high frequency signal injection**,"** *Conference Record of the IEEE Industry Applications Society 38th IAS Annual Meeting*, vol.3, pp. 1982 – 1989, 2003.

[10] Obaid, R. R., Habetler, T. G., and Tallam, R. M., "Detecting load unbalance and shaft misalignment using stator current in inverter-driven induction motors," *Conference record of the IEEE IEMDC'03, IEEE International Conference on Electric Machines and Drives*, vol. 3, pp. 1454-1458, 2003.

[11] Von Jouanne, A., Gray, W. and Enjeti, P., "Application issues for PWM adjustable speed AC motor drives," *Record of the IEEE Industry Application Magazine*, pp. 10 - 18, 1996.

[12] Schoen, R. R., "On-line current-based condition monitoring of three-phase induction machines," Ph.D. dissertation, Department of Electrical Engineering., Georgia Institution of Technology., Atlanta, September 1994.

[13] Welch, P.D., "The use of Fast Fourier Transform for the estimation of power spectra: a method based on time averaging over short, modified periodograms,' *IEEE Transaction on Audio and Electroacoustics*, vol. 15, no. 2, pp. 70-73, 1967.

[14] Lynn Kirlin, R., Beach, M. M., and Trzynadlowski, A. M., "Analysis of power spectral density in PWM inverters with randomized switching frequency," *IEEE Transaction on Industrial Electronics*, vol. 49, no. 2, pp. 486-499, 2002.

[15] Marques Cardoso, A.J., Cruz, S.M.A, Carvaho, J.F.S., and Saraiva, E.S., "Rotor cage fault diagnosis in three-phase induction motors, by Park's Vector approach," *Conference Record of the IEEE IAS Annual Meeting*, vol. 1, pp. 642-646, 1995.

[16] Nandi, S., "Fault analysis for condition monitoring for induction motors, " Ph.D. dissertation, Department of Electrical Engineering., Texas A&M University, Atlanta, May 2000.

[17] Benbouzid, M.E.H., Nejjari, H., Beguenane, R., and Vieira, M., "Induction motor asymmetrical faults deytectiom using advanced signal processing techniques," *IEEE Transactions on Energy Conservation,* vol. 14, no. 2, pp. 147-152, June 1999.

[18] Obaid, M. "Detection of rotating mechanical asymmetries in small induction machines," Ph.D. dissertation, Department of Electrical Engineering., Georgia Institution of Technology., Atlanta, May 2003.

[19] Hurst, K., "Transducerless control and monitoring of induction machines by detection of magnetic saliency harmonics," Ph.D. dissertation, Department of Electrical Engineering., Georgia Institution of Technology., Atlanta, October 1996.

[20] Al-Tuaimi, H., "Detection of Incipient Rotor Bars Fault and Air-Gap Asymmetries in Squirrel-Cage Motors Using Stator Current Monitoring," Master of science thesis, Department of Electrical Engineering and Computer Science., Oregon State University, Corvallis, March 2005.

[21] Stack, J. R., "Fault signature detection for rolling element bearings in electrical machines," Ph.D. dissertation, Department of Electrical Engineering., Georgia Institution of Technology., Atlanta, October 2002.

[22] Thorsen, O. V. and Dalva, M., "Failure identification and analysis for high voltage induction motors in petrochemical industry," *IEEE Transaction on Industrial Electronics*, vol. 35, no. 4, pp. 810-818, 1995.

[23] Devaney, M.J. and Eren, L., "Detecting motor bearing fault," *IEEE Transaction on Instrumentation and Measurement*, vol. 7, no. 4, pp. 30-50, 2004.

[24] Benbouzid, M El and Kliman, G. B., "What stator current processing-based technique to use for induction motor rotor faults diagnosis?," *IEEE Transactions on Energy Conservation,* vol. 18, pp. 238–244, Jan. 2003.

Appendix A: MATLAB® code for implementing the Welch power spectral density approach

```
% Specify the sampling frequency speed and the number data in each segment
fs= 10000;
m=100000;

% Healthy condition
% Extract the data from the saved file and tabulat it as a vector x
hp_nl_80hz;
x=hp_nl_80hz (1:100000);
% Apply windowing method
window1=hamming(m);
% Make an over lap to segmented part
noverlap1=m/2;
% Plot Welch method for spectral analysis estimation
pwelch(x,window1,noverlap1,[],fs,'c');

hold on

% Faulty condition

sbr_100I_p_a_80Hz;
q=sbr_100I_p_a_80Hz(1:100000);
window2=hamming(m);
noverlap2=m/2;
pwelch(q,window2,noverlap2,[],fs);


hold off
title('Single broken rotor bar vs healthy from programmable source at different loads and
80 Hz  ')
```

Appendix B: MATLAB® code for implementing the negative and positive approach

```
%initialize vectors:
i1=[0;0;0];
i2=[0;0;0];

% Healthy condition
%Input tabulated current data:
%The data are stored into a file, which is read by MATLAB

%input_current_data_phase-a;
ia=h_100I_m_a_60hz;

%input_current_data_phase-b;
ib=h_100I_m_b_60hz;

%input_current_data_phase-c;
ic=h_100I_m_c_60hz;

% Applying positive-sequence Transformation to input currents:

a=exp(j*2*pi/3);

Kabc_abc1=(1/3)*[1          a          a^2;
                 a^2        1          a;
                 a          a^2        1];

% Applying negative-sequence Transformation to input currents:

Kabc_abc2=(1/3)*[1          a^2        a;
                 a          1          a^2;
                 a^2        a          1];

% Data length:
m=100000;
for t=1:1:m
ihelp_abc= [ia(t);
            ib(t);
            ic(t)];

 help1 = Kabc_abc1*ihelp_abc;
 help2 = Kabc_abc2*ihelp_abc;
 i1=[i1 help1];
 i2=[i2 help2];
```

```
 ih1=i1(1,:);              % positive-sequence
 ih2=i2(1,:);              % positive -sequence
% Power spectrum density plots (see appendix A):

fs= 10000;                 % Sampling frequency

x=ia(1:m);
window1=hamming(m);
noverlap1=m/2;
pwelch(x,window1,noverlap1,2^20,fs);
hold on

x=ih1(1:m);
window1=hamming(m);
noverlap1=m/2;
pwelch(x,window1,noverlap1,2^20,fs);

x=ih2(1:m);
window1=hamming(m);
noverlap1=m/2;
pwelch(x,window1,noverlap1,2^20,fs);


 % Faulty condition

%initialize vectors:
if1=[0;0;0];
if2=[0;0;0];

%Input tabulated current data:
%The data are stored into a file, which is read by MATLAB

%input_current_data_phase-a;
ifa=be2_100I_m_a_60Hz;

%input_current_data_phase-b;
ifb=be2_100I_m_b_60Hz;

%input_current_data_phase-c;
ifc=be2_100I_m_c_60Hz;

% Applying positive-sequence Transformation to input currents:

a=exp(j*2*pi/3);

Kabc_abc1f=(1/3)*[1          a          a^2;
                  a^2        1          a;
                  a          a^2        1];
```

```
% Applying negative-sequence Transformation to input currents:

Kabc_abc2f=(1/3)*[1          a^2          a;
                  a          1          a^2;
                  a^2        a          1];

% Data length:
m=100000;
for t=1:1:m
ihelp_abcf= [ifa(t);
             ifb(t);
             ifc(t)];

  helpf1 = Kabc_abc1f*ihelp_abcf;
  helpf2 = Kabc_abc2f*ihelp_abcf;
  if1=[i1 helpf1];
  if2=[i2 helpf2];

  if1=if1(1,:);          % positive-sequence
  if2=if2(1,:);          % positive -sequence
% Power spectrum density plots (see appendix A):

fs= 10000;               % Sampling frequency

x=ifa(1:m);
window1=hamming(m);
noverlap1=m/2;
pwelch(x,window1,noverlap1,2^20,fs);

x=if1(1:m);
window1=hamming(m);
noverlap1=m/2;
pwelch(x,window1,noverlap1,2^20,fs);

x=if2(1:m);
window1=hamming(m);
noverlap1=m/2;
pwelch(x,window1,noverlap1,2^20,fs);

hold off

title ('Negative and positive components for healthy vs. faulty with mains supply at 60 Hz
and 100%load ')
```

Appendix C: MATLAB® code for implementing the three phases Park's vector approach

```
idq=[0;0;0];
%idq2=[0;0;0];
%idq1=[0;0;0];

%Input tabulated current data:
%The data are stored into a file, which is read by MATLAB

%input_current_data_phase-a;
ia=bbe_100I_dr_a_60Hz;

%input_current_data_phase-b;
ib=bbe_100I_dr_b_60Hz;

%input_current_data_phase-c;
ic=bbe_100I_dr_c_60Hz;

% Applying Park's Transformation to input currents:

Kabc_dq=[sqrt(2)/sqrt(3)          -1/sqrt(6)          -1/sqrt(6);
                 0                1/sqrt(2)          -1/sqrt(2);
                 0          0          0];
% Data length:
m=10000;
for t=1:1:m
ihelp_abc= [ia(t);
            ib(t);
            ic(t)];
  helpdq = Kabc_dq*ihelp_abc;
  idq=[idq helpdq];
  ids=idq(1,:);          % d-axis current
  iqs=idq(2,:);          % q-axis current
end

plot (ids, iqs, 'k');


title ('Parks vector for bearing fault with drive at 60 Hz and 100% load ')
```